Synthesis and Electrochemical Cycling Characteristics of Nanostructured Antimony Alloying Electrodes for Energy Storage Applications

Grant Andrew Williamson

A dissertation

submitted in partial fulfillment of the

requirements for the degree of

Doctor of Philosophy

University of Washington

2019

Reading Committee:

Vincent C. Holmberg, Chair

Daniel T. Schwartz

Cody W. Schlenker

Program Authorized to Offer Degree:

Molecular Engineering

University of Washington

Abstract

Synthesis and Electrochemical Cycling Characteristics of Nanostructured Antimony Alloying Electrodes for Energy Storage Applications

Grant Andrew Williamson

Chair of the Supervisory Committee:

Vincent Holmberg

Chemical Engineering

Nanostructured antimony is a highly promising alloying electrode material for both Li-ion and Na-ion battery systems, possessing a large gravimetric charge storage capacity (660 mAh g^{-1}) combined with extraordinary rate capability (cycling at a 20C rate results in only a ~15% decrease in capacity, relative to 1C). Herein, we elucidate the fundamental drivers for the performance of antimony nanomaterial-based Na-ion battery negative electrodes with a particular focus on the effects of morphology, temperature and oxidation.

In support of these studies, we report the supercritical-fluid-based synthesis of highly anisotropic, hexagonal antimony nanoplatelets with 1000:1 aspect ratios and average thicknesses of 50±10 nm and use the nanoplatelets as a model system to investigate how morphology and strain impact the phases that are encountered during the electrochemical alloying of nanostructured

antimony in Na-ion battery electrodes, the thermodynamics and kinetics of battery cycling and the electrode morphology and conductivity. For these investigations we study the electrodes via capacity and differential capacity analysis, a high-fidelity galvanostatic intermittent titration technique, conductive atomic force microscopy and *in situ* X-ray diffraction. We find that active material anisotropy results in increased ordering and crystallinity during cycling for the antimony nanomaterial-based electrodes and increased composite heterogeneity. We also identify c-NaSb a previously unobserved phase for antimony-based Na-ion battery electrodes that occurs primarily during degraded cycling.

We then utilize electrochemical impedance spectroscopy to investigate the source of temperature-based performance changes in antimony nanocrystal-based Na-ion battery electrode materials. We find that increased charge transfer resistance is predominantly responsible for the observed 100 mAh g^{-1} capacity reduction (~20%) that occurs upon changing the cycling temperature from 50 to 5°C. Furthermore, we determine that the observed decrease in capacity at low temperature is almost entirely caused by increased charge transfer resistance due to less facile Na-ion transport across the solid-electrolyte interphase layer-electrode interface.

Additionally, we systematically study the effects of oxidation on antimony-based electrode performance. Most antimony-based and antimony oxide-based electrodes are typically fabricated into electrodes in a water-based slurry under atmospheric conditions. While this fabrication approach is lower cost and much safer than the methods used for other battery electrode materials that must be processed using toxic organic solvents under inert gas, the level of oxide formation that occurs during water-based slurry processing of nanostructured antimony has largely been undiscussed and left as an uncontrolled variable during electrode fabrication. Here, we systematically investigate the impact of oxide formation on changes in the electrochemical

performance of antimony nanocrystal-based Na-ion battery negative electrodes, providing insight as to why small amounts of oxide result in enhanced gravimetric capacity and capacity retention, while more extensive oxidation results in reduced rate capability. We find that barriers to the sodiation of highly oxidized antimony are reduced by amorphization of the crystalline antimony oxide (c-Sb_2O_3) during extended cycling, while sodium sequestration leads to low reversible sodium storage utilization upon extended cycling.

Dedication

For my family

Acknowledgements

With sincerest gratitude I give my thanks to everyone who has helped me on my journey throughout my life and through my doctorate. My community has been the backbone of my endeavors, motivating, supporting, and inspiring me daily. I would also like to give special thanks to a number of individuals who have been particularly instrumental in helping me reach where I am today.

I would like to thank my graduate advisor, Dr. Vincent Holmberg, for the insight, opportunities, and guidance he has provided me with during my time in graduate school. I have been inspired by his true passion for science and discovery and it has been a privilege and an honor to help start his research lab at the University of Washington. I would like to thank Dr. Cody Schlenker, Dr. Corie Cobb, and Dr. Daniel Schwartz for serving on my committee. I would also like to thank Dr. Daniel Schwartz for all the opportunities he has provided for me during both my graduate and undergraduate at the University of Washington, starting from before I first set foot on campus. Furthermore, I would like to acknowledge the National Science Foundation Graduate Research Fellowship Program for supporting my graduate studies.

I would like to thank Elena Pandres for being a constant sounding board, for collaborating closely as we learned the ropes of nanomaterial synthesis and battery testing and for all of her effort in setting up our research labs that allowed me to hit the ground running. I would also like to thank Martin Affandy, Ayden Andersen, Benedicte Daikubama, Tiara Naidu, Jarrid Nakata, Benny Olivas, Charles Opie, Emilee Paradis, Chester Pham, and Tommy Yoo for their tireless work in the lab in support of my research plans. In addition, I would like to thank Guesang Kevin Lee for his close collaboration on the antimony nanomaterials research. I am also indebted to all

of the current and former members of the Holmberg group, including Brittany Bishop, Soohyung Lee, Sabiha Rustam, Nicole Thompson, Chih-Wei Hsu, Ge Gu, and Yiheng Zhang.

I would also like the thank the Schlenker group for the access to and use of their equipment which was critical to much of my doctoral studies, in particular Jarred Olson, who also taught me how to fabricate and test electrodes and batteries. In addition, I would like to thank Lucas Flagg, Dr Raj Giridharagopal, Dr Sarah Vorpahl, and Jake Precht along with the rest of the Ginger group for their AFM analysis of my battery electrode materials. I would also like to thank Victor Hu for his collaboration on the antimony temperature studies, particularly his expertise in electrochemical impedance spectroscopy. Furthermore, I would like to thank all of the staff at the Molecular Engineering Facility, the Washington Clean Energy Testbeds, the Research Training Testbeds, particularly Kristine Parra, Dr. Phil Cox, Ellen Lavoie, Scott Braswell and Dr. Liam Bradshaw, who provided extensive assistance in materials and device characterization and testing that was critical to my research.

I also would like to thank Dr. Joseph Fairweather and the rest of the Schwartz group for introducing me to scientific research during my undergraduate at the University of Washington. Furthermore, I would like to thank Dr. John Falconer and Dr. Miao Yu for their support during my summer research experience at the University of Colorado-Boulder, as well as Dennis Smith and the rest of his team for their support during my internship at Lam Research. Additionally, I would like to thank Gilberto Perkins, Josh Dewanaga, and the rest of the team for their support and mentorship during my time at GE Water and Process Technologies.

Finally, I would like to thank my friends and family for their support, understanding and encouragement during my graduate studies, in particular, my fiancée Tori Hernandez, my parents Bill and Sandy Williamson, and my brother Parker Williamson.

Portions of this work are reproduced in part from Williamson, G. A.; Hu, V. W.; Yoo, T. B.; Affandy, M.; Opie, C.; Paradis, E. K.; Holmberg, V. C. Temperature-Dependent Electrochemical Characteristics of Antimony Nanocrystal Alloying Electrodes for Na-Ion Batteries. *ACS Appl. Energy Mater.* **2019**, *2* (9), 6741–6750. https://doi.org/10.1021/acsaem.9b01216 Copyright 2019 American Chemical Society. This article can be viewed via the following link: http://pubs.acs.org/articlesonrequest/AOR-MupWZ8cI5SpXFFiyn8Aw. Additional portions of this work are reproduced from journal articles with full citations and attribution in the thesis metadata.

Table of Contents

List of Tables

List of Figures

Chapter 1: Introduction

1.1 The Role of Energy Storage in the Energy System

The current global energy system relies heavily on carbon-intensive fuels and centralized, demand-driven electricity grid systems.[1–6] The next generation energy system will look much different, with a heavily-reduced carbon footprint and a distributed, analytics-driven electricity grid system that responds readily to supply and demand needs to support a cost-benefit analysis by individual consumers.

The transition to the new generation system is already occurring via a complicated interplay of technology and policy. On the technology side, much of this advancement has come from improving solar and wind technologies to the point where they are lower cost without subsidies than conventional generation technologies such as coal, natural gas and nuclear in many cases.[7] In response to these significant advancements in clean energy technology, policy has been developed to further spur technology development and to adapt the incentives in the energy system to these new technologies.[3–6,8] In particular, significant investments have been made in both research and development and technology cost subsidies to drive technology development and implementation. However, solar and wind energy are not drop in replacements for conventional generation due to the intermittent nature of both the sun and the wind.[5] The technology differences between clean energy generation and conventional generation have thus necessitated a shift in utility compensation and design policy.

The traditional model for utility design is a hub and spoke model, whereby large hubs supply energy at a central point that branches out to all the distribution locations and power only flows in one direction, from the hub to the spokes.[3] In this model, demand drives supply and large power plants (peaker plants) are turned on as necessary to compensate for increased load on the

system.[9] The cost of generation for a peaker plant is very high, since they only operate for short times. This paradigm works well when electricity generation is not modular (conventional generation) and the demand for energy and the cost of energy cannot be updated in real-time due to data processing and analysis constraints (20th century computing power).

The new model for utility design is an interconnected system where demand and supply are physically intermingled and power can flow in many directions based on production and need.[4] In this model, both demand and supply interplay and consumer, particularly large consumers can reduce their supply needs in times of high system load or low production. This paradigm works well when electricity generation is modular (solar and wind) and the demand for energy and cost of energy are updated in real-time due to readily available data processing and analysis (21st century computing power.

The traditional model and the new model for utility design require fundamentally different policies to ensure adequate compensation for both the production facilities and the grid owners. The new model involves many more players because the inputs of supply and demand now both factor into the cost-analysis for the grid and the location of production for even the small sources is critical for cost-effective power production. Thus, while the new model in its optimized form reduces system cost, the model is more complicated and dynamic and utility policy must be updated to reflect this.

Energy storage plays a critical role in the new utility paradigm.[9,10] The major new generation sources (solar and wind) are intermittent as described above. However, reliability is key to grid function and is policy mandated.[4,5] While peaker plants can be used to ensure this reliability, they do not represent an ideal solution because of the high operating cost. Instead energy storage is a more ideal technology for the new highly integrated grid. Energy storage follows the

buy low, sell high paradigm in that when supply exceeds demand energy storage facilities harvest the excess demand (low cost) and when demand exceeds supply energy storage facilities distribute the stored energy (high cost). In addition, these facilities are modular. There are many energy storage technologies that have already been commercialized for gird level energy storage.[11] In general for these technologies there is a trade-off between the energy density of the storage and the length of back-up with technologies like Li-ion batteries having a very high energy density (small physical footprint) and low length of back-up (minutes to hours) and technologies like pumped hydro having a very low energy density (large physical footprint) and a high length of back-up (days to months). The new grid system relies on balancing the cost, energy density and length of back-up. Li-ion batteries have a critical role to play in this system as they can help compensate for the intermittency of solar and wind, providing a rapid response to peaks and troughs in supply and demand that occur with the daily schedules of humanity.

In addition, Li-ion batteries are particularly ideally suited to address transportation, the one major area of the energy system that wind, solar and other clean energy primary generation technologies cannot. Currently transportation represents ~30% of the energy system in the USA and is the sector with the least clean energy input.[12] The energy for transportation comes from secondary generation technologies, where energy is stored before use from a primary source and then released. In transportation, high energy density is critical, because in general, the vehicle must not only move itself and its occupants but also the fuel. Low energy density fuels weigh more and so dramatically reduces vehicle efficiency.

While Li-ion batteries do not have as high of an energy density as conventional petroleum fuels, they are sufficiently high in energy density that a car can travel hundreds of miles on one charge based on current technology.[13] There is also significant room for further advances in battery

technology and cost reduction.[14,15] In addition, charging an electric vehicle is currently much slower than filling a gas tank. However, next generation materials can improve the rate to where it is comparable to filling a gas tank.[16,17] Furthermore, with the integrated smart grid system, electric vehicles can provide significant additional energy storage while they are not in use. Overall, next-generation battery technologies will be critical to enabling the next-generation grid and decarbonizing the transportation system.

1.2 Battery Design and Function

In this section, we discuss the major components of batteries, and how batteries work. The three major functional components of a battery are a negative electrode, a positive electrode and an electrolyte.[14] A battery stores and releases energy via electrochemical reactions at the electrodes. When a battery is discharging, the working ions and electrons are released from the negative electrode via electrochemical redox reactions. The electrons travel outside the battery through an electrical circuit, providing energy to the connected devices, while the working ions shuttle through the electrolyte to the positive electrode. At the positive electrode, the electrons and working ions recombine again via electrochemical redox reactions.

The ability of a battery to provide energy during discharge defines key parameters for the battery components.[14,15] First, the negative electrode must store the working ion and electrons at higher energy than the positive electrode. The maximum voltage of a battery is defined by this difference in energy between the electrodes. Second, the electrolyte must not conduct electrons, but must conduct the working ion. In most cases, if the electrolyte were to conduct electrons, the electrons would not move through the connected circuit outside the battery to provide energy, because the path of least resistance between the electrodes would be through the electrolyte. When

electrons travel through the battery rather than through the outside circuit, the battery is operating in a short circuit mode and generates heat rapidly, putting it at risk of fire or explosion.[18] Therefore, the electronic resistivity of the electrolyte is critical not only to function of the battery but also to its safety. Clearly, the function of the battery is strongly defined by the materials in the battery itself.

1.3 Antimony as a Next-Generation Negative Electrode Material

Antimony-based electrodes have demonstrated high capacity (660 mAh g^{-1}) and extraordinary rate-capability in both Li-ion and Na-ion battery systems.[16,17] Antimony (Sb) is one of the highest capacity single-element negative electrode materials for Na-ion batteries, with a theoretical capacity lower than only phosphorus and tin.[17,19] In addition, nanostructured antimony has been shown to exhibit a capacity reduction of only 15% when the cycling rate is increased from 1C (one hour charge) to 20C (three minute charge), clearly demonstrating its excellent rate capability.[16,17] Consequently, nanostructured antimony is an ideal material for next-generation high-power-density, high-capacity battery negative electrodes.

Antimony has a higher theoretical capacity than current Li-ion battery graphite-based negative electrodes (372 mAh g^{-1}), because it stores energy in a fundamentally different way.[14,15] Graphite is an intercalation material.[15] In intercalation materials, the ions reversibly insert into the electrode and are stored in the interstitial spaces of the electrode, without changing the structure of the electrode material. The working ions associate with delocalized electrons in the structure such that there is overall charge neutrality. In the case of graphite, which consists of sheets of carbon atoms, the Li-ions are stored between the sheets, with one Li-ion and one electron per six carbon atoms (LiC_6).[15] As Li-ions are added, the graphite expands approximately 10% but the

sheets of carbon remain otherwise structurally the same. Intercalation materials are currently the most common electrode material type for both positive and negative electrodes in commercial Li-ion batteries, because the small structural change promotes stable cycling.

Alloying materials such as antimony physically react with the Li-ion and electrons to form a chemically bonded alloy. In the case of antimony, the terminal state for working-ion addition is M_3Sb, where M is Li or Na.[16] Alloying materials experience structural rearrangement as the working ion is added or removed (charge and discharge respectively for the negative electrode).[15,20] This structural rearrangement typically supports higher gravimetric and volumetric capacities than are possible with intercalation electrodes. However, this structural rearrangement also causes volumetric expansion (Sb to Na_3Sb has an expansion of ~290%).[17] This expansion leads to significant strain which in turn can lead to structural degradation and reduced capacity.[16,21–23]

The strain-driven structural degradation of alloying electrode materials typically takes the form of electrode cracking leading to increased solid-electrolyte interphase (SEI) layer formation or delamination of the electrode from the current collector.[16,21–23] In the case of electrode cracking, each crack exposes additional electrode material to the electrolyte. The exposed electrode material reacts with the electrolyte to form additional solid-electrolyte interphase (SEI) layer.[24,25] The SEI layer is the passivation layer that forms at the electrode-electrolyte interface during initial cycling, as electrons reach the electrolyte and react with it.[26] In a stable battery, the SEI layer is an electronic insulator that prevents further irreversible reactions between the electrolyte and the electrode from occurring. The SEI layer formation reduces capacity during initial cycling, because it sequesters working ions in non-soluble forms rendering them inactive and increases the overpotential required for the battery to operate. Additional SEI layer formation that occurs after cracking causes

a further reduction in capacity via the same mechanisms. When delamination occurs, the delamination disrupts the electron transport pathways from the active material to the current collector, preventing electrons from ever reaching the current collector, which also reduces capacity.[27] Many common Li-ion negative electrode alloying materials see exacerbated degradation in Na-ion batteries, since the larger Na-ion size increases the structural damage.[16,28] Strain-driven cracking and delamination must be reduced to enable long lifetime, high-capacity alloying negative electrodes, particularly for Na-ion batteries.

Nanostructuring mitigates the capacity loss caused by the volumetric expansion of alloying electrodes, substantially increasing capacity retention.[16,21–23,26,29–33] Nanostructured materials suffer less cracking degradation and delamination than bulk materials because the working ion concentration gradient across the nanomaterial is small, reducing stress and strain.[4] In addition, the nanostructuring introduces void space into the electrode helping it to more easily accommodate expansion than a bulk material. Nanostructured electrodes can also have high charge and discharge rates because the solid-state diffusion path length is small.

Nanostructured antimony shows significant promise as a high capacity, high power density material.[16,17,34–41] Recent research on antimony has focused on understanding the fundamental underpinnings of antimony performance in Na-ion batteries, as well as exploring different types of antimony alloys.[27,42–55] Continuing to develop a broader fundamental understanding of both the drivers of this high performance and the critical factors for capacity retention represents the next step forward for the commercialization of antimony-based negative electrode materials for Li-ion and Na-ion batteries.

1.4 Dissertation Overview

Antimony is an exciting electrode material for use in Na-ion and Li-ion batteries, due to its high-capacity and high-power.[16,17] Herein we focus on antimony primarily as a Na-ion battery material, given that it is one of the highest capacity single element materials in Na-ion batteries.[17,19] Furthermore, we focus on areas of research where we can connect the fundamental drivers of performance in antimony electrode materials with parameters critical to commercialization.

In Chapter 2, we discuss the synthesis of highly anisotropic antimony nanoplatelets using a supercritical fluid growth process. We also discuss the fundamentals of supercritical fluid-based nanomaterial growth and the other products that result from parameter space that we explored. In Chapter 3, we then compare the performance of the highly anisotropic antimony nanoplatelets to the performance of isotropic antimony nanocrystals to elucidate the effects of morphology on performance in antimony nanomaterials. We delve into the underlying phenomena that lead to the morphology-based performance differences using 1D uniaxial stress-strain modeling, differential capacity analysis, a high fidelity galvanostatic intermittent titration technique, and *ex situ* analysis via atomic force microscopy and scanning electron microscope-based energy dispersive X-ray spectroscopy. We find that anisotropy in antimony nanostructured electrodes leads to reduced capacity retention due to both increased strain and crystallinity on the individual particle level and increase electrode heterogeneity. In Chapter 4, we suggest that the formation of differential capacity peak that occurs after extended cycling at ~0.93 V during desodiation results from the desodiation of c-NaSb, using *in situ* XRD and calculations from the literature.[43]

In Chapter 5 we discuss the temperature-dependent capacity of antimony nanocrystals. We study the drivers for the changes in capacity with temperature primarily using electrochemical impedance spectroscopy. We also examine the capacity changes with differential capacity analysis

and *ex situ* scanning electrode microscopy of electrode before cycling and after cycling at different temperatures. We demonstrate that the capacity changes are primarily driven by increased charge transfer resistance across the SEI layer-electrode interface.

In Chapter 6 we examine the electrochemical performance of systematically oxidized antimony nanocrystals. We study the performance via capacity retention and rate-based electrochemical test. We elucidate the performance drivers via differential capacity analysis and a high-fidelity galvanostatic intermittent titration technique. We find that oxidized antimony nanocrystals have significant kinetic and thermodynamic limitations to cycling that prevent full utilization of the electrode capacity.

Chapter 2: Supercritical Fluid Synthesis of Highly Anisotropic Antimony Nanoplatelets

2.1 Introduction

Scalable syntheses utilizing anhydrous organic supercritical fluids have been developed for the production of numerous nanostructured material systems that require high growth temperatures;[56–61] however, to our knowledge, the supercritical-fluid-based synthesis of nanostructured antimony has not yet been explored. Supercritical solvents have significant advantages relative to high-boiling-point solvents, including a wider accessible temperature range and decreased post-processing costs associated with product purification.[56,60,62] Supercritical solvents have a wider accessible temperature range, since solvothermal and hot-injection nanomaterial syntheses done on a Schlenk line are limited by the solvent boiling point, while supercritical solvents fundamentally are unable to boil. The inability of supercritical fluids to boil also leads to easier cleaning, since high-boiling point solvents used on a Schlenk line are typically viscous and therefore difficult to clean. In contrast low-viscosity solvents such as toluene, hexane or benzene can be used in supercritical fluid-based nanomaterial syntheses. The low-viscosity of these solvents results in less aggressive cleaning requirements. Moreover, supercritical solvents exhibit liquid-like solvation, which facilitates the selection of cheaper/safer precursors, and vapor-like transport coefficients, which assist the rate of reaction.[60] The ability to access high temperatures within a supercritical fluid medium enables a wider range of nanomaterial crystallization conditions and the use of a wider range of precursors, as compared to solvothermal and hot-injection syntheses.

While typical liquid-based colloidal syntheses of antimony nanomaterials employ the use of halogenated precursors, here we explore the growth of nanostructured antimony via the thermal

decomposition of triphenylantimony ($SbPh_3$) in anhydrous supercritical toluene.[16,17,34,35,63–65] Above 375°C it was found that the reaction parameters could be tuned selectively to produce Sb nanostructures and microstructures with a variety of different morphologies. High precursor concentrations unsurprisingly led to dendritic growth, while intermediate precursor concentrations and elevated temperature (500°C) gave rise to micrometer-sized truncated octahedra (Figure 2-1).

Most interestingly, under optimized steady-state growth conditions (0.5 mL/min injection of 4.3 mM triphenylantimony into a 10 mL reactor filled with supercritical anhydrous toluene at 425°C and 900 psig), it was possible to direct crystal growth selectively along the high-energy facets perpendicular to the c-axis of the material, resulting in the ultrathin, highly anisotropic nanoplatelets. The antimony nanoplatelets are hexagonal in character, as would be expected from a material with an $R\bar{3}m$ space group, with measured thicknesses ranging from 30 to 80 nm (average thickness of 50±10 nm) and lateral dimensions of several micrometers, resulting in nanoplatelets with aspect ratios as large as 1000:1.[66] Additionally, including small amounts of oleic acid under air-free growth conditions led to the formation of large Sb_2O_3 octahedra, whereas other ligands were found to have minimal impact on product morphology. Under certain conditions, platelets with lateral dimensions in excess of 100 μm were observed.

2.2 Experimental Methods

2.2.1 *Materials.*

Oleic acid (90%), oleylamine (70%), sodium borohydride (99.99%), toluene (anhydrous, 99.8%), trioctylphosphine (TOP) (97%) and triphenylantimony (≥99.0%) were purchased from Sigma Aldrich. Oleic acid and oleylamine were degassed and stored under a nitrogen atmosphere. All other reagents were used as received without further purification.

2.2.2 Supercritical-Fluid-Based Synthesis of Nanostructured Antimony.

In a typical synthesis, a stock solution of triphenylantimony (5 g) dissolved in anhydrous toluene (10 mL) was prepared in an inert-atmosphere nitrogen glove box. A nitrogen-filled, continuous-flow supercritical reactor with a 10-mL internal volume was heated to 425°C and pressurized to 900 psig with anhydrous toluene (See Ref. [67] for further details of the supercritical reactor system).[67] The triphenylantimony stock solution (360 μL, 1.42 M) was diluted with an additional 11.6 mL of anhydrous toluene, drawn into a syringe, and subsequently loaded into a 10-mL injection coil leading to the reactor inlet. The triphenylantimony precursor solution was then injected into the reactor at a rate of 0.5 mL/min for 20 min at 425°C and 900 psig. After completion of the reaction, the reactor was cooled to room temperature, and the product was collected and stored under ambient conditions.

2.2.3 Materials Characterization.

Transmission electron microscopy (TEM) images were acquired with a FEI Tecnai G2 F20 Supertwin TEM, operating with an accelerating voltage of 200 kV. Cross-sectional images were acquired by embedding the Sb nanoplatelets in epoxy using the Embed-812 Resin Kit, and then microtoming the resulting composite using a Leica EM UC6 Ultramicrotome. Dark-field scanning transmission electron microscopy (STEM) images of the epoxied and microtomed samples were used to generate a histogram of nanoplatelet thicknesses (Figure 2-2). Scanning electron microscope (SEM) images and energy-dispersive X-ray spectroscopy (EDXS) data were collected using a FEI XL830 Dual Beam FIB/SEM operating at 5 kV for imaging and 10 kV for EDXS analysis. X-ray diffraction (XRD) patterns were collected with a Bruker D8 Discover diffractometer with an IμS 2-D XRD detector system and analyzed using EVA software. *In situ* XRD patterns were collected with a Bruker D8 Advance diffractometer with a Lynxeye X-ET

detector while the *in situ* cell was cycled with a Princeton Applied Research VersaSTAT 4. The crystal structure of Sb was modeled using VESTA software along with crystallographic data from the American Mineralogist Crystal Structure Database.[66,68,69] The crystal habit models were generated using the Great Stella software package and VESTA, again with crystallographic data from the American Mineralogist Crystal Structure Database. [66,68–70]

2.3 Results and Discussion

2.3.1 Reaction Parameter Space

While minimal precursor decomposition was observed below 375°C, the reaction parameters (Primarily precursor concentration and temperature) could be tuned selectively to produce Sb nanostructures and microstructures with a variety of different morphologies at higher temperatures. (Table 2-1, Figure 2-1). Table 2-1 details the parameter space explored for the supercritical-fluid-based synthesis of nanostructured antimony via the decomposition of triphenylantimony in anhydrous supercritical toluene. All reactions were carried out in a cylindrical, 10-mL-volume titanium reactor charged with anhydrous supercritical toluene under continuous flow. Precursor solutions were prepared by dissolving the prescribed quantity of triphenylantimony in anhydrous toluene in a nitrogen-filled glove box. In all cases, the precursor solution was injected into the reactor at a rate of 0.5 mL/min. The values reported in Table 2-1 and the images in Figure 2-1 correspond to the concentration of triphenylantimony in the precursor solution, prior to injection into the reactor. Minimal precursor decomposition was observed below 375°C, while uncontrolled dendritic growth was observed to occur at high precursor concentrations. Additional discussion and characterization of the morphologies produced under optimized intermediate conditions can be found in the sections below.

Table 2-1. Parameter space explored for the supercritical-fluid-based synthesis of nanostructured antimony in supercritical toluene.

Triphenylantimony Concentration	400°C	425°C	450°C	475°C	500°C
0.43 mM	Minimal product	Dilute nanoplatelets	Dilute nanoplatelets	Thick polyhedra	Thick polyhedra
4.3 mM	Anisotropic nanoplatelets	Anisotropic nanoplatelets	Large nanoplatelets and truncated octahedra	Truncated octahedra and wide nanoplatelet sheets	Truncated octahedra
42 mM	Dendritic growth	Dendritic growth	Dendritic growth	Large dendritic structures	Uncontrolled dendritic growth

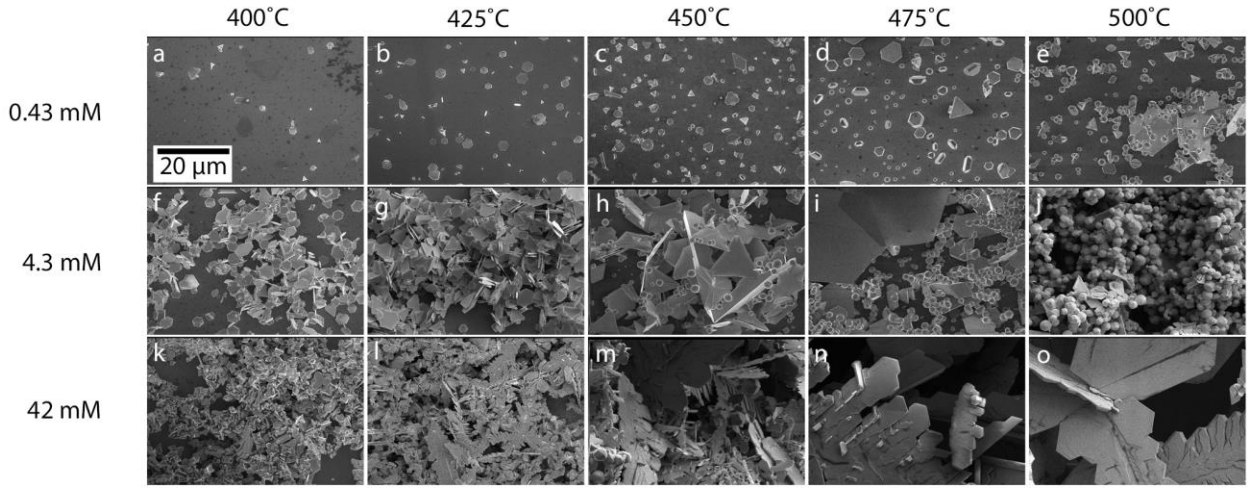

Figure 2-1. SEM images of antimony nanomaterials and micromaterials synthesized by injecting toluene solutions containing different concentrations of triphenylantimony (0.43 mM, 4.3 mM and 42 mM) into a 10-mL continuous flow-through reactor filled with anhydrous supercritical toluene at temperatures of 400, 425, 450, 475, and 500°C, using a 0.5 mL/min injection rate.

2.3.2 Highly Anisotropic Antimony Nanoplatelets

The highly anisotropic antimony nanoplatelet have measured thicknesses ranging from 30 to 80 nm (average thickness of 50±10 nm) and lateral dimensions of several micrometers (Figure 2-2). For the most anisotropic nanoplatelets, the aspect ratios can be as large as 1000:1.

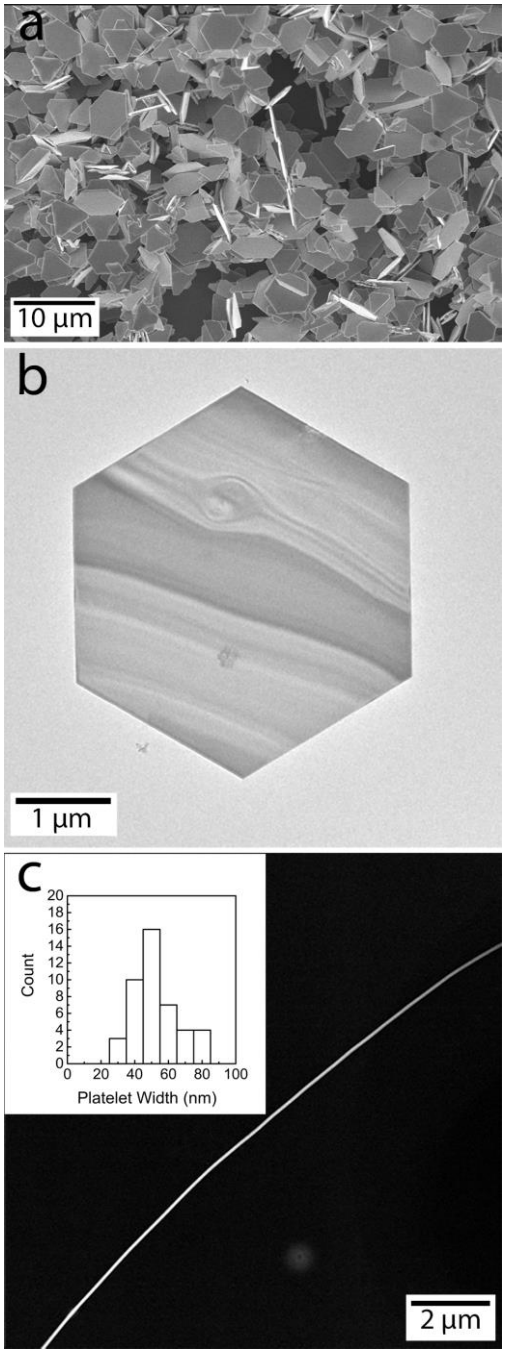

Figure 2-2. Electron microscopy images of highly anisotropic Sb nanoplatelets synthesized by injecting 4.3 mM triphenylantimony at a rate of 0.5 mL/min into 10 mL of supercritical anhydrous toluene at 900 psig and 425°C : characteristic (a) SEM, (b) TEM, and (c) cross-sectional, dark-field STEM images of ultrathin hexagonal antimony nanoplatelets. A histogram of antimony nanoplatelet thicknesses measured via cross-sectional dark-field STEM is included as in inset in

panel (c). As can be seen in Figure 2-3, antimony nanoplatelets produced by the decomposition of triphenylantimony in supercritical toluene are hexagonal in character, with lattice spacings that correspond to crystalline antimony. Energy-dispersive X-ray spectroscopy (EDXS) and X-ray diffraction (XRD) analysis provide further evidence that the nanoplatelets are composed of rhombohedral antimony, with small amounts of surface oxide present due to air exposure following synthesis. As shown in Figure 2-3e, the hexagonal antimony unit cells are stacked such that the c-axis of each unit cell is oriented perpendicular to the face of the nanoplatelet. The model in Figure 2-3 corresponds to the experimentally observed crystallographic orientation, where the indexed spots in the fast Fourier transform (FFT) of the image (Figure 2-3a, inset) correspond to the directions pointing toward the vertices of the platelet. $R\bar{3}m$ antimony forms pseudo-layered sheets with a buckled honeycomb structure, where the puckered hexagonal pseudo-layers form the faces of each nanoplatelet.[71] The interatomic distances within the individual layers (shown in purple) are shorter than the interatomic distances between layers (gold), corresponding to the weakened bonding that exists between layers.

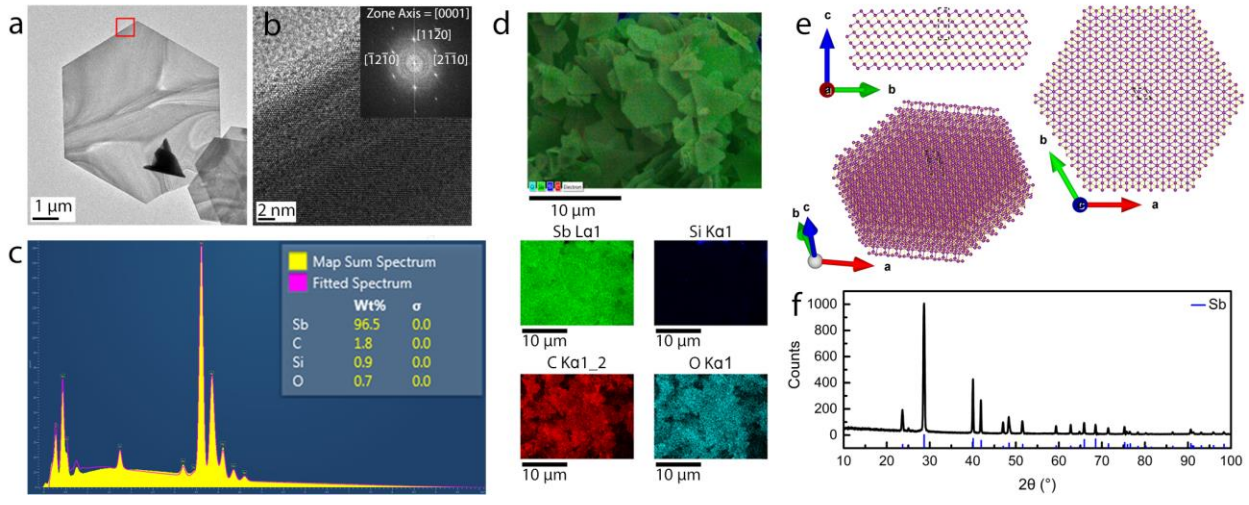

Figure 2-3. (a) Characteristic transmission electron microscopy (TEM) image of Sb nanoplatelets grown at 425°C using a 4.3 mM precursor injection solution, along with (b) a high-resolution TEM

image with FFT inset corresponding to the region highlighted by the red box in panel a. (c) EDXS map sum spectrum corresponding to the (d) scanning electron microscopy (SEM) image and EDXS mapping images of the Sb nanoplatelets synthesized at the conditions described above. (e) Crystallographic modeling of the antimony nanoplatelets showing a side view, an off-axis view, and a top view, with an antimony unit cell outlined in thin dashed lines. (f) XRD pattern collected from the product shown in panels a-d (PDF#: 00-035-0732).[72]

Under optimized, steady-state growth conditions, it was possible to promote anisotropic platelet formation through extension of the crystal in the lateral directions perpendicular to the c-axis via the preferential addition of adatoms to the high-surface-energy facets that terminate the platelet edges.[73] Over time, the slow-growing, low-surface-energy $\{0001\}$ surfaces become the predominant crystal facets, ultimately resulting in the thermodynamically favored Wulff shape for rhombohedral antimony, corresponding to a hexagonal prism where the $\{10\bar{1}1\}$ family of planes form pairs of sloping sidewalls along the lateral edges of the prism (Figure 2-3e).[74] Since hexagonal platelets are the thermodynamically favored morphology, they have a significant presence within the explored parameter space, with nanoplatelet formation particularly favored between 400 and 425°C. For electrochemical testing, antimony nanoplatelets were grown using an intermediate 8.5 mM precursor concentration and 425°C reaction temperature in order to maximize product yield while maintaining the target nanoplatelet morphology.

2.3.3 Truncated Octahedra

For intermediate precursor concentrations, and elevated reaction temperatures near 500°C, truncated antimony octahedra (Figure 2-4) were the predominant product. Since octahedral shapes are somewhat uncommon for materials within the rhombohedral $R\bar{3}m$ space group (Figure 2-3 and

Figure 2-4), it is likely that the formation of these structures is enabled by twinning.[73] In antimony, twinning typically occurs on the $\{01\bar{1}4\}$ planes, frequently forming fourlings, which can then result in a truncated octahedral geometry.[75] Since the probability of twinning increases when the rate of atomic addition during growth is increased,[76] a large preponderance of truncated octahedra would be expected under conditions corresponding to rapid precursor decomposition at elevated temperature. Moreover, in this kinetically dominated regime, the energy difference for atomic addition to different facets becomes less important,[77,78] which in turn leads to more pseudo-spherically shaped structures that minimize overall surface area, thus resulting in truncated octahedra becoming the favored crystal habit at high temperatures.

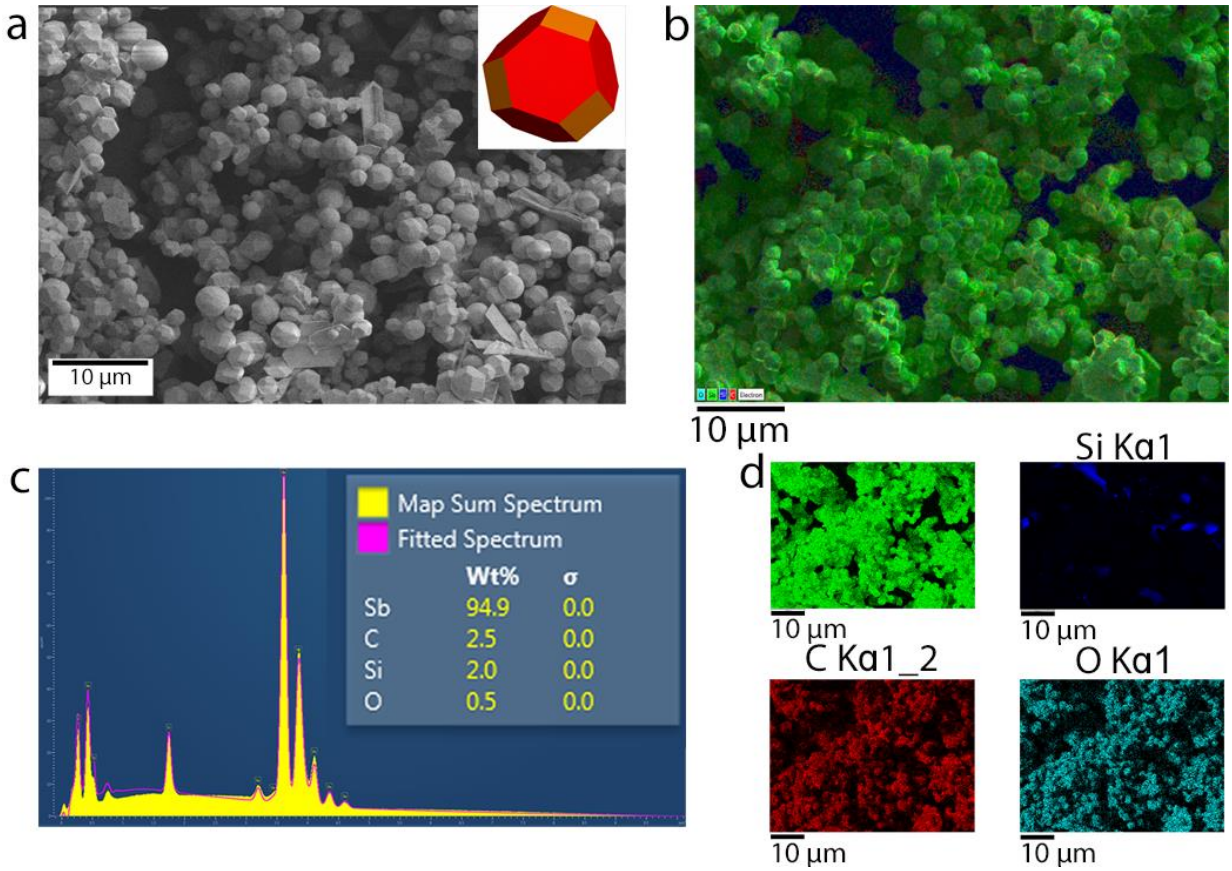

Figure 2-4. (a) Characteristic SEM image of the truncated octahedra produced a 500°C reaction temperature with a 4.3 mM precursor injection solution, include a cartoon truncated octahedron in the inset.[70] (b-d) SEM image, EDXS mapping data, and EDXS map sum spectrum corresponding to the truncated Sb octahedron product.

Interestingly, at 475°C, while truncated octahedra still dominate the reaction product, extremely wide nanoplatelet sheets were also produced (Figure 2-5). The largest nanoplatelets observed were up to 100 µm wide, corner-to-corner, likely resulting from a subset of antimony seed crystals that did not twin during the early stages of growth.

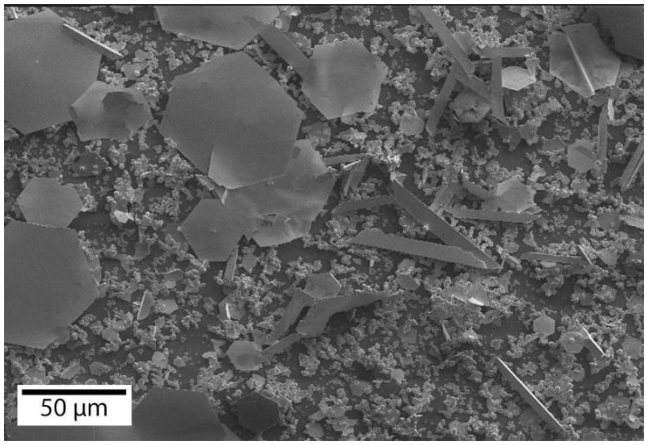

Figure 2-5. SEM image of antimony materials synthesized at 475°C with a 4.3 mM precursor injection solution. Nanoplatelets with tip-to-tip dimensions greater than 100 µm comprise a fraction of the sample.

2.3.4 Effects of Ligand Addition During Synthesis

The co-injection of ligands during nanoplatelet growth was also briefly explored (Figure 2-6). While oleylamine and trioctylphosphine were found to have minimal impact on product morphology, the co-injection of small amounts of oleic acid was found to reduce the number density of nanoplatelets in the final product, and also lead to the formation of large octahedra. Interestingly, in addition to rhombohedral antimony, XRD analysis indicates the presence of Sb_2O_3 in the samples synthesized under co-injection with 1% v/v oleic acid (Figure 2-6e). EDXS mapping indicates that the entirety of the Sb_2O_3 signal originates from large octahedral Sb_2O_3 byproducts, while the hexagonal nanoplatelets remain composed of elemental antimony (Figure 2-6f). Since the supercritical reactor is run under anhydrous, anaerobic conditions, the observation of Sb_2O_3 octahedra indicates that the oleic acid reacts with the decomposing antimony precursor, acting as an oxygen source that results in the formation of the observed Sb_2O_3 byproduct.

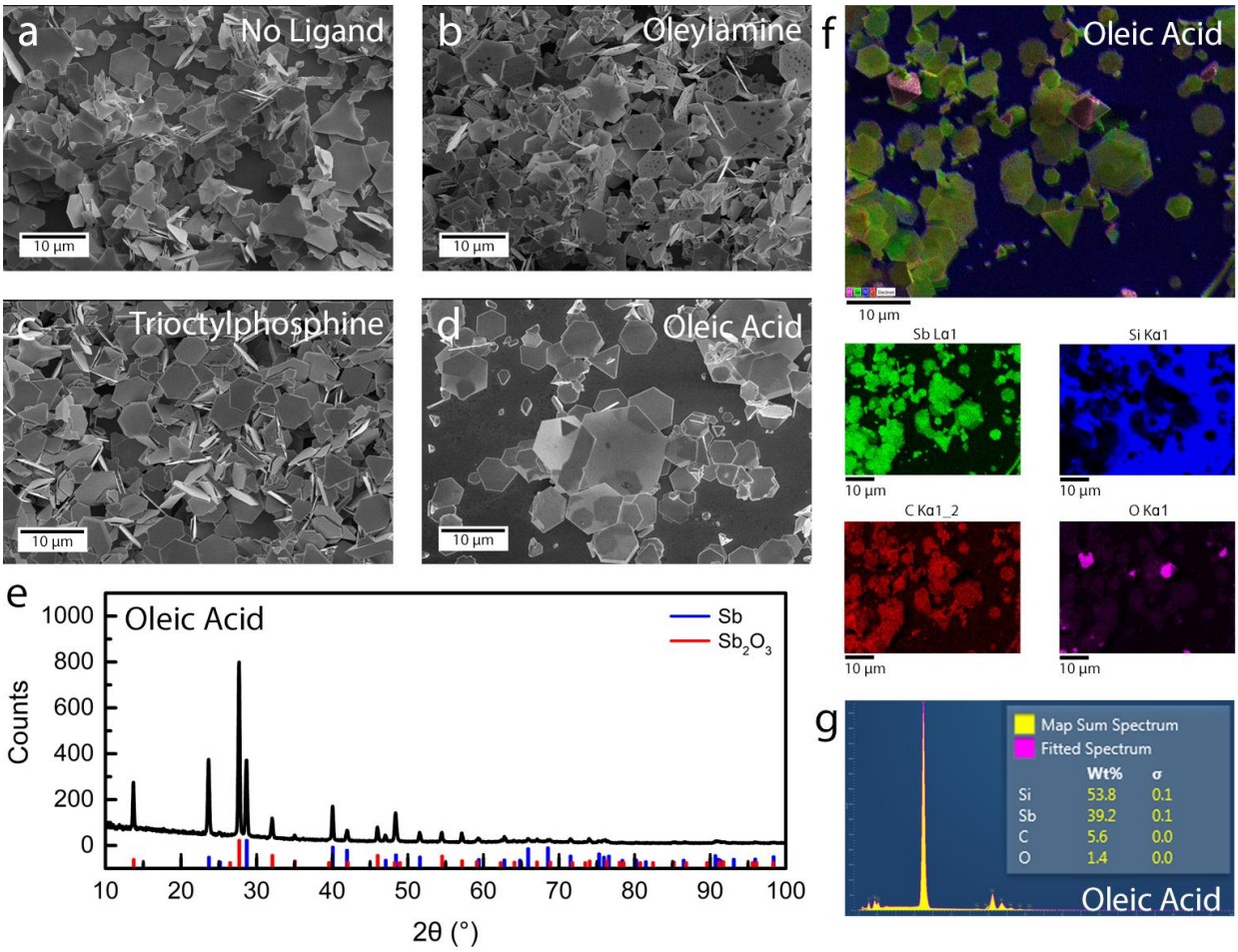

Figure 2-6. (a-d) SEM images of Sb nanoplatelets grown at 425°C using a 4.3 mM precursor injection solution along with co-injection of (a) no ligand, (b) 1% v/v oleylamine, (c) 1% v/v trioctylphosphine, (d) 1% v/v oleic acid. (e-g) Compositional characterization of Sb product grown in the presence of oleic acid, with (e) XRD (Sb PDF#: 00-035-0732, Sb_2O_3 PDF#:00-042-1466)[72,79] and (f-g) EDXS data clearly showing the presence of a minority component, octahedral Sb_2O_3 byproduct.

2.4 Conclusions

In Chapter 2, we explore the supercritical fluid-based synthesis of antimony nanostructures and microstructures using a triphenylantimony precursor in an anhydrous toluene solvent. We find

minimal precursor decomposition below 375°C. At elevated temperatures, we find that the product morphology can be selectively tuned, with high precursor concentrations leading to dendritic growth and intermediate concentrations at high temperature (500°C) resulting in microsized truncated octahedra. Most interestingly, we demonstrate that ultrathin, highly anisotropic antimony nanoplatelets with lateral dimensions of many micrometers and aspect ratios in excess of 1000:1 form in the rest of the explored parameter space with thicknesses between 30 and 80 nm (average thickness of 50±10 nm). The lateral dimension of these platelets can extend to in excess of 100 μm under certain conditions. While the product morphology is relatively insensitive to ligand addition, we also find that the addition of small amounts of oleic acid under air-free growth conditions resulted in the formation of Sb_2O_3 microoctahedra, due to the reaction of oleic acid with the triphenylantimony precursor. The ultrathin antimony nanoplatelets may have possible applications for the development and study of topological and 2D materials.

Chapter 3: Morphology-Dependent Electrochemical Characteristics of Antimony Nanomaterials

3.1 Introduction

In Chapter 3, we study how active material morphology effects performance by comparing the electrochemical alloying characteristics of the highly anisotropic antimony nanoplatelets discussed in Chapter 2 to small, isotropic antimony nanocrystals.[17] Alloying electrodes experience significant volume expansion during cycling (~290% for antimony).[17] This volume expansion leads to significant strain and in turn electrode damage and capacity loss. Nanostructured electrodes have represented an important pathway to reduced strain for alloying-type electrodes.[16,21–23] However, the expansion and associated stress and strain can be strongly affected by morphology of the nanostructures. Thus, determining the effects of morphology on performance and the underlying drivers for morphology-based effects is critical to both a strong scientific understanding of antimony-based negative electrodes and moving antimony towards commercialization.

In this chapter, we study the effects of morphology on antimony nanomaterial electrode performance using capacity and differential capacity analysis, 1D uniaxial stress-strain modeling, a high fidelity galvanostatic intermittent titration technique (GITT) and *ex situ* analysis via atomic force microscopy (AFM) and scanning electron microscope (SEM)-based energy dispersive X-ray spectroscopy (EDXS). We observe via the capacity and differential capacity analysis and 1D uniaxial stress-strain modeling that strain drives increased crystallization and suppression of amorphous solid-solution reactions, leading to additional reliance on two-phase reactions as sources of capacity.

We then develop a stronger fundamental understanding of both the morphology- and degradation-dependent kinetics, thermodynamics and diffusion for antimony nanomaterial-based electrodes via a high-fidelity galvanostatic intermittent titration technique (GITT).[80] We implement this high-fidelity GITT for both Na-ion battery antimony nanocrystal and antimony nanoplatelet conversion type negative electrodes up to cycle 400.

During GITT, the battery is cycled in steps, whereby a known amount of current is passed at a specific rate followed by a relaxation period where no current is passed.[80] This process is repeated until the cell has been cycled across the voltage window. At a given state of charge (SOC), the relaxation steps provide the equilibrium voltages while the current injection steps contain kinetic regimes connected to the cell configurational IR drop (fast), the reaction resistance (intermediate or slow) and the diffusive behavior (slow).[81] The stepwise nature of GITT cycling unconfounds the thermodynamic and kinetic components of the cycling behavior, providing significant insight into the cell electrochemistry.

Based upon the high-fidelity GITT, we find that the increased rate of capacity reduction in the anisotropic antimony nanoplatelets relative to the isotropic antimony nanocrystals results from increased strain-driven kinetic overpotentials during desodiation. This overpotential consists of both a reaction overpotential and a diffusional overpotential. However, the diffusional overpotential is the primary driver for both the rapid capacity loss of the anisotropic antimony nanoplatelets and the capacity loss after extended cycling for the isotropic antimony nanocrystals. Therefore, the diffusion coefficients were determined for both morphologies using the high-fidelity GITT

Although Baggetto et al. investigated the diffusion coefficient of antimony thin films close to the terminal sodiation state during desodiation, to our knowledge, this GITT data represents the

first study of the Na-ion diffusion coefficients in antimony electrode materials for the full cycling window and during extended cycling.[82] In calculating the diffusion coefficient from the GITT data, we implement methods to account for the composite conversion electrode behavior. Although the diffusion coefficients are on the order of 10^{-9} cm^2 s^{-1} at the terminal Na_3Sb sodiation state and 10^{-12} cm^2 s^{-1} at the terminal Sb desodiation state during initial cycling for both the antimony nanocrystals and antimony nanoplatelets, the antimony nanoplatelet diffusion coefficients drop-off rapidly while the antimony nanocrystal diffusion coefficients remain constant through cycle 100.

Finally, we use *ex situ* analysis via atomic force microscopy and scanning electron microscope-based energy dispersive X-ray spectroscopy to connect the nanoscale morphology of the electrode to the performance of the antimony nanomaterial electrodes. Connecting the nanoscale morphology of the antimony nanomaterial electrode is important to understanding battery performance on the bulk scale, because the electrode material is a composite that can be highly heterogenous on the nanoscale.[83–87] The nanoscale heterogeneity of an electrode can lead to different sections of the electrode having substantially different performance. This is particularly likely because the interactions and electrochemical properties of the active material, conductive carbon, binder, electrolyte and SEI layer all affect both capacity retention and rate capability. We find by comparing the chemical mapping and the physically observable structures to conductive atomic force microscopy (c-AFM) that the heterogeneity of the electrodes is substantially larger for the antimony nanoplatelets and that this heterogeneity correlates strongly with the conductivity of the sample. This suggests that the lower capacity retention of the antimony nanoplatelets is driven in part by the heterogeneity of the composite electrodes. Overall, it is clear that anisotropy

has many deleterious effects on performance and must be controlled in antimony nanomaterial-based electrodes.

3.2 Experimental Methods

3.2.1 Materials.

N-Methyl-2-pyrrolidone (NMP) (anhydrous, 99.5%), antimony trichloride (≥99.0%), propylene carbonate (99.7%), sodium metal (>99.99%, dry cubes, ACS Specification), sodium borohydride (99.99%), sodium carboxymethyl cellulose (M_w ~90,000), toluene (anhydrous, 99.8%), and triphenylantimony(III) (≥99.0%) were purchased from Sigma Aldrich. Sodium perchlorate (≥98%) was purchased from Fisher Scientific. Fluoroethylene carbonate (≥98%) was purchased from TCI America. Carbon black (Vulcan XC72R) was purchased from Cabot Corporation and stored in a vacuum oven at 80°C. Copper foil (>99.99%, 9 μm thickness) was purchased from MTI Corporation. An Embed-812 Resin Kit was purchased from Electron Microscopy Sciences.

3.2.2 Supercritical Fluid-Based Synthesis of Highly Anisotropic Antimony Nanoplatelets.

Using the procedure described in Chapter 2, a stock solution was prepared with triphenylantimony (5 g) in anhydrous toluene (10 mL) in an inert-atmosphere nitrogen glove box. A silicon wafer piece was placed in a 10 ml internal volume supercritical flow-through reactor. The reactor was filled with nitrogen and then heated to 425°C and pre-filled with anhydrous toluene until the internal pressure reached 900 psig (See reference [67] for further details of the experimental setup of the supercritical reactor). Triphenylantimony stock solution (720 μL, 1.42 M) was diluted in 11.3 mL of anhydrous toluene, mixed via ~30 seconds of vortexing, and drawn into a syringe. The syringe was then used to fill a 10 mL injection coil that connected to the reactor

inlet. The precursor solution was pumped into the reactor at a rate of 0.5 mL/min for 20 min, while the reactor was maintained at 425°C and 900 psig. After the reactor was cooled to room temperature the wafer with antimony nanoplatelet product was collected and stored in air.

3.2.3 Synthesis of Isotropic Antimony Nanocrystals.

Isotropic antimony nanocrystals were synthesized using the procedure of Walter *et al.*[17] Sodium borohydride (48 mmol) was solvated in NMP (51 mL) in a flask that was heated to 60°C under nitrogen. A solution of antimony trichloride (12 mmol) in NMP (9 mL) was prepared in an inert atmosphere nitrogen glovebox. This solution was injected into the flask. The flask was immediately placed into an icebath for rapid cooling to room temperature. After centrifugation at 7440 RCF for 4 minutes, the supernatant was decanted off. The centrifugate was washed with deionized water (~30 mL) three times in a vacuum flask with a filter funnel. The antimony nanocrystals were then dried overnight under vacuum and stored in an inert atmosphere nitrogen glovebox.

3.2.4 Electrode Fabrication, Coin Cell Assembly, and Electrochemical Testing.

Electrode fabrication used a 64:21:15 mass ratio of Sb:carbon-black:carboxymethylcellulose. The materials were combined and mixed into a slurry using a mortar and pestle with a deionized water carrier based on standard procedures.[16,17,88,89] In a typical fabrication, 150 mg of antimony and 49 mg of carbon black were mixed with 0.52 mL of CMC in deionized water (0.067 g/mL), followed by dilution with an additional 0.4 mL of deionized water. Note that the 0.4 mL of DI water was adjusted to account for environmental conditions as needed. The resulting slurry was doctor-bladed (38 μm thickness) onto a copper foil current collector with a 38 μm thickness and dried on a hot plate at 80°C in air until no moisture was visible (typically ~5 min). Electrodes were further dried and stored in a vacuum oven that was pumped down below

15 mbar at 80°C until ready for punching. The electrodes were punched out into 15-mm-diameter circles. These were stored in a vacuum oven set below 15 mbar at 80°C until battery assembly. Half cells were assembled in an argon glovebox using elemental sodium metal as the positive electrode, a glass fiber separator (Whatman, grade gf/f), 1.0 M $NaClO_4$ in an electrolyte solution of 90% w/v propylene carbonate and 10% w/v fluoroethylene carbonate and a CR2032 case. Electrochemical testing was performed with a MACCOR Series 4000M 64-Channel Automated Battery Test System. Batteries were cycled at a rate of 1C (current density of 660 mA g^{-1}) except for GITT cycles, where they were cycled at a rate of C/10 rate (current density of 66 mA g^{-1}). For GITT the cycling protocol involved cycling the batteries out to cycle 400 with GITT cycles at cycles 2, 5, 10, 20, 40, 100, 200 and 400. During GITT cycles, current was injected for 1 minute and then the cell was rested for 10 minutes. Capacities were normalized versus the weight of the active materials.

For the AFM sample preparation, magnetic stirring was used instead of mortar and pestle-based mixing. The same Sb:carbon-black:carboxymethylcellulose ratios were used, along with the same carboxymethylcellulose concentration in DI water. The sample was magnetically stirred in a vial until the water evaporated. The samples were then epoxied using the Embed-812 Resin Kit, and then microtomed at 1 μm using a Leica EM UC6 Ultramicrotome onto an ITO-coated glass substrate. The microtomed samples were analyzed via conductive AFM performed on an AFP-3D (Asylum Research) using gold coated contact mode silicon AFM probes (ContGB-G, Budget Sensors) and scanning electron microscope (SEM)-based energy-dispersive X-ray spectroscopy (EDXS) using a FEI XL830 Dual Beam FIB/SEM.

3.3 Results and Discussion

3.3.1 Electrochemical Sodiation/Desodiation of Isotropic and Anisotropic Antimony Nanostructures.

Electrochemical cycling was performed at a rate of 1C on negative electrodes comprised of highly anisotropic antimony nanoplatelets (Figure 2-2) and electrodes comprised of isotropic antimony nanocrystals.[17] While the spherical nanocrystals were observed to maintain a specific capacity above 600 mAh g^{-1} throughout 100 cycles at 1C (Figure 3-1a), the capacity of the nanoplatelets rapidly decreased to ~200 mAh g^{-1} after 100 cycles at 1C (Figure 3-1d) due to the significantly increased lateral strain in the system (see section 3.3.1.1 for detailed strain calculations and discussion). Past studies have examined the sodiation and desodiation processes along varied crystallographic directions for antimony materials,[43,82] concluding that sodiation primarily occurs via the hopping of Na ions through the collinear octahedral voids of the material.[43] Desodiation from Na_3Sb is more complicated, with the lowest barrier for desodiation occurring along the a and b axes, in addition to two desodiation pathways along the c-axis that are higher in energy.[43] Notably, the barriers for ion diffusion and propagation of strain are related, leading to anisotropic strain that is dependent upon the preferred crystallographic directions for diffusion.[82]

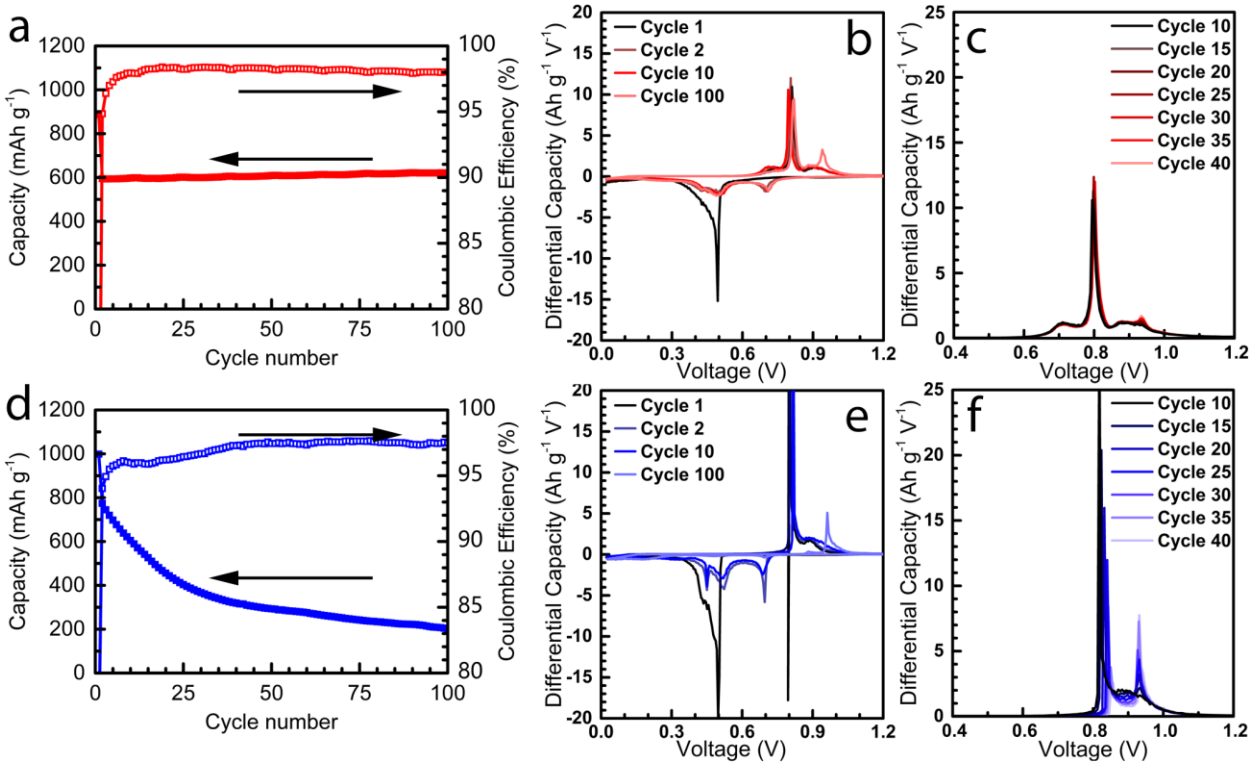

Figure 3-1. (a) 1C cycling performance, (b) differential capacity, and (c) desodiation differential capacity of Sb nanocrystals, and (d) 1C cycling performance, (e) differential capacity, and (f) desodiation differential capacity of Sb nanoplatelets, illustrating the gradual formation of a new electrochemical feature at 0.93 V after extended cycling.

The total differential capacity plots of the highly anisotropic nanoplatelets and the isotropic nanocrystals shown in Figure 3-1 provide insight into the differences in the electrochemical cycling characteristics of the two morphologies.[16,17,28,42] Notably, the nanoplatelets exhibit sharper alloying/dealloying peaks than the nanocrystals, with broad peaks being characteristic of solid-solution transitions with disordered (amorphous) interfaces and sharp peaks being characteristic of electrochemical reactions that include a two-phase transition with ordered (crystalline) interfaces (Figure 3-1b,e).[90] Uniaxial 1D stress and strain calculations included in the supplementary information quantitatively demonstrate that the lateral strain in the nanoplatelets is

much larger than the strain in the nanocrystals. Fracture analysis is also done to supplement the stress and strain calculations, with the fracture analysis indicating cracking occurs for the antimony nanoplatelets, but not the antimony nanocrystals. The results of the stress and strain calculations combined with the morphology-dependent changes in the differential capacity plots this observation suggest that the increased lateral strain in the nanoplatelets promotes the formation of crystalline phases, at the expense of the amorphous phases that help to enable stable cycling in the small, isotropic antimony nanocrystals.

To this point, the isotropic nanocrystals clearly exhibit a broad desodiation peak centered at 0.72 V (just to the left of the c-Na_3Sb desodiation peak at 0.8 V) which is absent in the nanoplatelet electrochemical cycling data. We note that smaller nanocrystals show this peak more prominently in the literature, while for larger micron sized particles this peak is suppressed;[16] however, to our knowledge, this peak has not been previously discussed in the context of a specific electrochemical event. By making a comparison to silicon alloying electrodes (which exhibit a similarly broad feature associated with the delithiation of a-Li_xSi at slightly lower potentials than the c-$Li_{3.75}Si$ delithiation peak)[91] – we attribute the feature centered at 0.72 V to the desodiation of a-$Na_{3-x}Sb$, where x is close to zero. In most cases, the desodiation of an amorphous phase is more facile than the associated crystalline state, and thus occurs at a slightly lower potential.[92,93] Consequently, suppression of the a-$Na_{3-x}Sb$ phase in the nanoplatelets can be attributed to strain-induced crystallization, which has been observed previously in a wide range of materials.[93–97] This observation aligns with the observed behavior in the literature, where larger micron-sized particles experience significantly more strain during cycling than smaller nanocrystals and therefore experience strain-induced crystallization which suppresses the a-Na3-xSb phase in favor of the c-Na3Sb phase, and in turn suppresses desodiation from the 0.72 V peak.[22,33,98] Collectively, these

observations highlight the importance of promoting the amorphous phases that can facilitate stable long-term cycling.

In addition to the a-$Na_{3-x}Sb$ desodiation feature at 0.72 V and the c-Na_3Sb to a-$Na_{1.7}Sb$, a-$Na_{1.7}Sb$ to a-NaSb and a-NaSb to c-Sb desodiation peaks at 0.8 V, ~0.82 V, and ~0.88 V respectively, by the 100th cycle, both the nanocrystals and the nanoplatelets exhibit an additional desodiation feature at 0.93 V (Figure 3-1c,f).[42] While this feature is not observed in the initial cycling profiles, the desodiation event at 0.93 V becomes more prominent between cycles 10 and 40 for both the nanocrystals and the nanoplatelets. By cycle 40, the peak at 0.93 V becomes the primary desodiation event for the nanoplatelets; however, for the spherical nanocrystals, the peak at 0.93 V does not become the primary desodiation feature until cycle 200 (Figure 3-2). In order to determine the nature of this previously undiscussed electrochemical feature that appears after extended cycling of antimony alloying electrodes, we carried out a set of *in situ* XRD experiments, described in detail in Chapter 4, which suggest that the peak at 0.93 V is caused by the desodiation of c-NaSb.

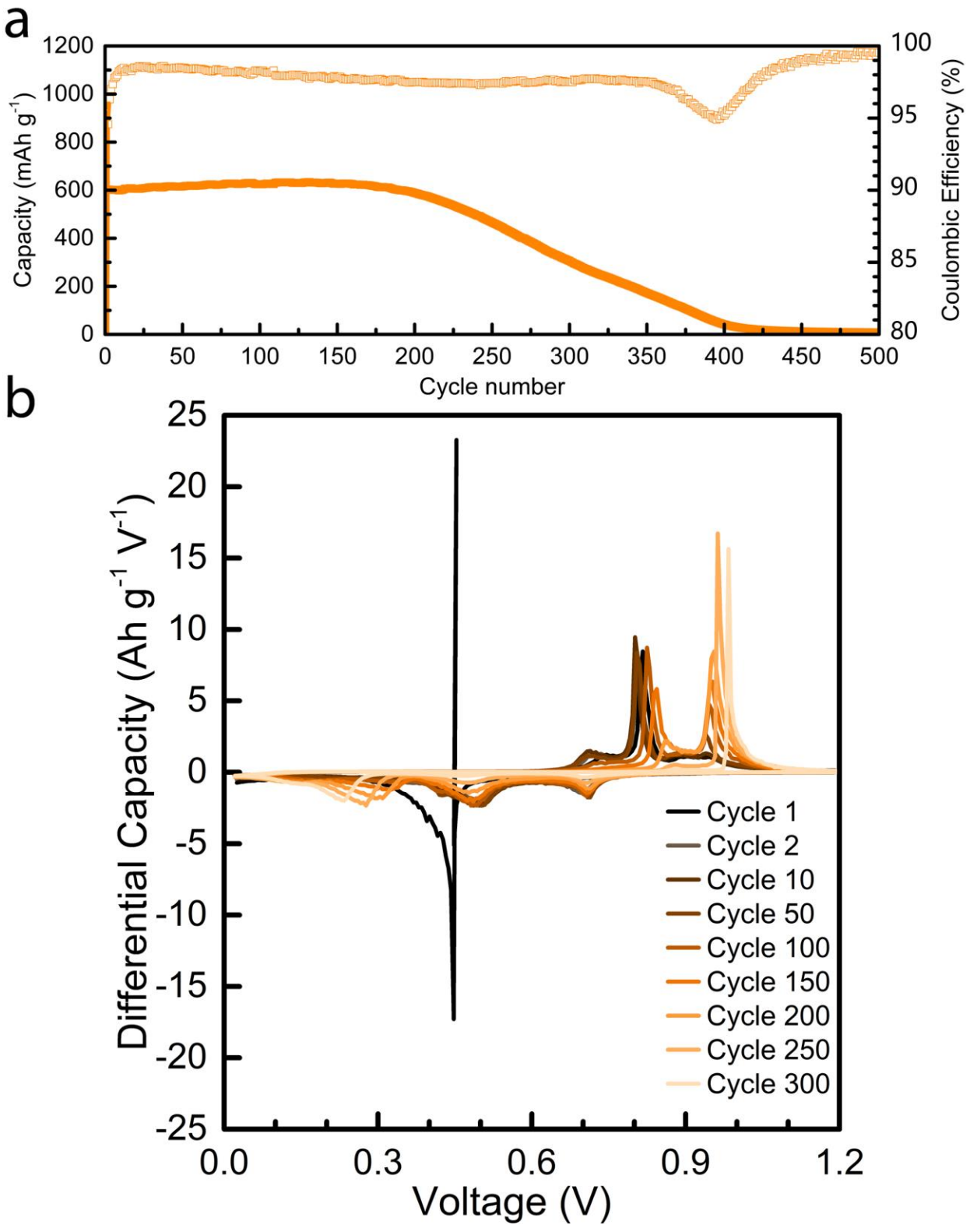

Figure 3-2. (a) Long-term 1C cycling performance of Sb nanocrystal negative electrodes prepared via the method of Walter *et al.*[17] along with (b) the corresponding differential capacity plots,

clearly showing the gradual formation of an additional electrochemical desodiation feature at 0.93 V after extended cycling.

Electrochemical profiles are shown for both the antimony nanocrystals and antimony nanoplatelets (Figure 3-3). The electrochemical profiles illustrate that the antimony nanoplatelets have a much larger irreversible capacity during the initial cycles, in addition to larger hysteresis than the antimony nanocrystals.

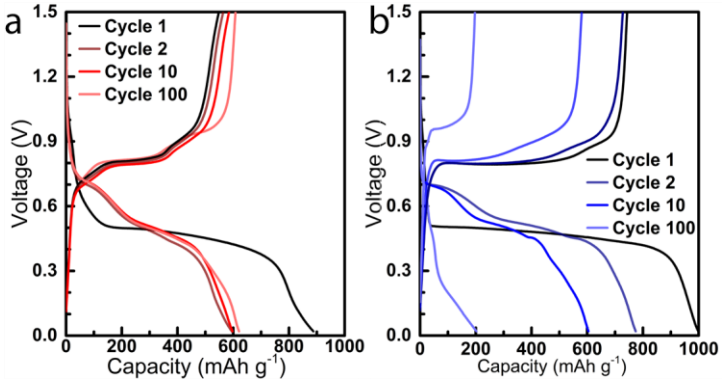

Figure 3-3. Standard electrochemical profiles of (a) Sb nanocrystals and (b) Sb nanoplatelets

3.3.1.1 ***Analysis of Stress and Strain during Electrochemical Cycling***

The stress and strain that occurs during electrochemical cycling can lead to structural degradation and reduced capacity for alloying electrode materials such as antimony.[33] Here, we use a simplified one-dimensional model to analyze stress and strain in the highly anisotropic antimony nanoplatelets and isotropic antimony nanocrystals, and we also examine the cracking characteristics of the two morphologies. Overall this analysis provides insight into the effects of anisotropy-driven strain on the electrochemical performance of antimony nanostructures.

First, the strain associated with the expansion of the crystal structure upon sodiation was calculated along each crystallographic direction by determining the change in separation between the antimony atoms in the unit cells for Sb and Na_3Sb. The interatomic spacings between adjacent

antimony atoms along the a and b directions are 4.0384 Å and 5.366 Å for Sb and Na_3Sb respectively. The average interatomic spacing between antimony atoms along the c direction for the Sb unit cell was determined by measuring the bond lengths and angles corresponding to both the interlayer and intralayer antimony bond distances, and then averaging the two values.[66,68,99] The 2.908 Å intralayer bond length and 3.355 Å interlayer bond length, along with the corresponding 31.205° and 42.147° angles between each bond and a plane perpendicular to the c-axis results in an average antimony c-direction spacing of 1.879 Å. Similarly, the 5.677 Å separation between antimony atoms in Na_3Sb along with the corresponding 56.928° angle between the Sb-Sb vector and a plane perpendicular to the c-axis results in an average antimony interatomic spacing along the c direction of 4.758 Å. We can then find the corresponding strain along each crystallographic direction using the following equation:

$$\gamma = \left(\frac{l_{Na_3Sb} - l_{Sb}}{l_{Sb}}\right) \qquad 3\text{-}1$$

where γ is the strain, and l_{Na_3Sb} and l_{Sb} are the distances in the a and b directions or the c direction between adjacent antimony atoms for Na_3Sb and Sb, respectively.[100]

Based on the above calculations, the nanoplatelets experience a strain of 1.5 (150% expansion) in the c direction (thickness) and a strain of 0.3 (30% expansion) in the lateral a and b directions during the transformation from Sb to Na_3Sb. Notably, although the relative expansion is smaller in the lateral a and b directions than the c direction, the large anisotropy of the nanoplatelets greatly magnifies the expansion that occurs along the lateral directions. For example, a 50-nm-thick, 10-µm-wide nanoplatelet will only expand 75 nm in thickness, while the lateral dimensions will expand by 3 µm.

The stress along each direction can then be related to the strain via the Young's modulus. Values for the Young's modulus in the a, b, and c directions were determined using the ELATE database.[101] For Sb, $E_{a,b}$ = 60 GPa and E_c = 30 GPa. Likewise, for Na_3Sb, $E_{a,b}$ = 33 GPa and E_c = 33 GPa. Since the intermediate phases between c-Sb and c-Na_3Sb are known to be amorphous during stable cycling, approximate uniaxial stresses along each direction were then estimated for each antimony alloying reaction that has been previously demonstrated in the literature[42] by assuming a linear continuum model for both the Young's moduli and the strains, as shown below:

$$E_{Na_{3-x}Sb,Na_{3-y}Sb} = \frac{\left(\left(E_{Na_3Sb} - E_{Sb}\right)\frac{(3-x)}{3} + E_{Sb}\right) + \left(\left(E_{Na_3Sb} - E_{Sb}\right)\frac{(3-y)}{3} + E_{Sb}\right)}{2} \quad 3\text{-}2$$

$$\gamma_{Na_{3-x}Sb,Na_{3-y}Sb} = \left|\left(\frac{\left(l_{Na_3Sb} - l_{Sb}\right)}{l_{Sb}}\frac{(3-x)}{3}\right) - \left(\frac{\left(l_{Na_3Sb} - l_{Sb}\right)}{l_{Sb}}\frac{(3-y)}{3}\right)\right| \quad 3\text{-}3$$

where x and y define the compositions for each reaction. Using the above correlations, the uniaxial stresses for each reaction were estimated (Table 3-1), and the largest source of stress in all directions was found to be the conversion of c-Sb to a-$Na_{3-x}Sb$, as would be expected. All of the other non-zero stresses were found to be within an order of magnitude. Additionally, the stresses in the c direction were found to be approximately three times larger than the stresses in the a or b directions.

Table 3-1. Uniaxial stresses in the a, b, and c directions for each reaction that occurs during antimony sodiation and desodiation.[42] The reactions are ordered based on the reaction voltage, starting at 1.5 V and proceeding from there through a full cycle.

Reaction	a-NaSb to a-$Na_{1.7}$Sb	a-NaSb to a-Na_{3-x}Sb	c-Sb to a-Na_{3-x}Sb	a-Na_{3-x}Sb to c-Na_3Sb	c-Na_3-Sb to a-$Na_{1.7}$Sb	a-$Na_{1.7}$Sb to a-NaSb	a-NaSb to c-Sb
Stress in a or b (GPa)	3.7	5.5	15	0	5.5	3.7	6.1
Stress in c (GPa)	11	21	48	0	20	11	15

A preliminary fracture analysis was also carried out for each of the antimony nanostructures by determining the energy release rate for crack propagation via the following equation:[102]

$$G = \frac{Z\sigma^2 h}{E} \qquad 3\text{-}4$$

where G is the energy release rate, Z is a dimensionless number based on fracture type that is on the order of 1, and h is the characteristic feature size. A Z-value of 2, which is typical for channel cracking in alloying materials such as silicon, is used here.[103] Fracture occurs if G is larger than the fracture energy, Γ, which can be calculated via the following equation:

$$\Gamma = \frac{2Ea}{27} \qquad 3\text{-}5$$

where a is distance between atoms in the direction of the strain, accounting for both anisotropy crystal lattice structure.[104] Note that this is a highly simplified model that provides only rough estimates for the fracture energy; however, the equation has been shown to approximate correct values within an order of magnitude for nanoscale systems in most cases.[104] For antimony, $a_{a,b}$ =

4.3084 Å and a_c = 6.0093 Å.[66] From this data, and the directionally-dependent Young's moduli for antimony ($E_{a,b}$ = 60 GPa and E_c = 30 GPa),[101] we can estimate that $\Gamma_{a,b}$ = 1.9 J/m^2 and Γ_c = 1.3 J/m^2. However, it is important to note that the largest fracture energy occurs along the $\langle 1\bar{1}02 \rangle$ directions where $E_{\langle 1\bar{1}02 \rangle}$ = 104 GPa and the average $a_{\langle 1\bar{1}02 \rangle}$ is 3.12 Å, resulting in a fracture energy of 2.4 J/m^2. Importantly, this vector family aligns with the octahedral voids in the antimony crystal structure (the voids through which Na diffusion occurs during sodiation), further supporting past observations that diffusion and strain are integrally related for antimony sodiation/desodiation.[43,82]

Based on Equation 3-4, for the reaction with the smallest non-zero stress (the conversion of a-NaSb to a-$Na_{1.7}Sb$), the, $G_{a,b}$ is 22 J/m^2 and G_c is 210 J/m^2 for 100-nm-diameter nanocrystals. For a 100-nm-thick, 1-µm-wide nanoplatelet, $G_{a,b}$ increases to 220 J/m^2 while the value of G_c remains the same as for the nanocrystals. The estimated energy release rates suggest that cracking would occur for both antimony morphologies, and an analogous analysis for silicon lithiation yields similar preliminary conclusions.[102] However, it is known that silicon thin films cycle reversibly at thicknesses greater than 50 nm, with a measured yield strength of 1.75 GPa.[102,105,106] Notably, silicon exhibits an increased fracture tolerance for reversible cycling (relative to the feature size predicted via comparison between the energy release rate and fracture energy) because nanoscale silicon yields inelastically, as opposed to cracking, up to a certain critical feature size.[102] Likewise, antimony nanocrystals are known to cycle with little performance degradation for particles with diameters less than 100 nm.[16,17] This suggests that antimony nanocrystals also yield inelastically up to a critical feature size. Based on this supposition, the yield strength of nanoscale antimony can be estimated using the following equation:

$$\sigma_{crit,z} = \sqrt{\frac{E\Gamma}{2h_{crit,z}}} \qquad 3\text{-}6$$

where $\sigma_{crit,z}$ is the yield strength along a particular direction, and $h_{crit,z}$ is the critical characteristic feature size in a given direction.[102] The critical yield strength was determined using Equation S6 for each of the key directions discussed above, resulting in values of $\sigma_{crit,a,b} = 1.1$ GPa, $\sigma_{crit,c} =$ 0.63 GPa, and $\sigma_{crit,\langle 1\bar{1}02\rangle}$ as 1.6 GPa.

Using the fact that the largest yield strength is in the $\langle 1\bar{1}02\rangle$ direction, and assuming that the critical characteristic feature size corresponds to the maximal 50-nm radius for reversible cycling of antimony nanocrystals,[16,17] the following equation can be used to determine whether the nanoplatelets exceed $h_{crit,\langle 1\bar{1}02\rangle}$:

$$h_c = \frac{50\ nm \times 2 \times 1.879\ \text{Å}}{\sqrt{\left(1 \times 4.0384\ \text{Å}\right)^2 + \left(\bar{1} \times 4.0384\ \text{Å}\right)^2 + 0^2 + \left(2 \times 1.879\ \text{Å}\right)^2}} \qquad 3\text{-}7$$

where h_c is the critical dimension for the platelets in the c direction, corresponding to half the platelet thickness. From the above equation, we find that h_c is 27 nm, resulting in a maximal platelet thickness of 55 nm for reversible cycling. Likewise, if the a and b directions are taken as the critical directions, the yield strength is still ~70% of $\sigma_{crit,\langle 1\bar{1}02\rangle}$. Consequently, considering that the smallest platelets are ~1 μm in lateral width, the nanoplatelets are clearly too large to cycle reversibly without strain-related damage.

3.3.2 Thermodynamics and Kinetics of Sodiation and Desodiation via High-Fidelity GITT

High-fidelity Galvanostatic Intermittent Titration Technique GITT data provides further insight into the morphology-dependent performance of antimony nanomaterials. The 1C capacity and differential capacity data for the non-GITT cycles matches closely with the cycling data from section 3.3.1 for both the antimony nanocrystals and antimony nanoplatelets (Figure 3-4). Thus, the high-fidelity GITT cycles are not affecting the performance on a global basis, validating the use of GITT to non-invasively study the thermodynamic and kinetic drivers for decay during extended cycling of antimony nanomaterials.

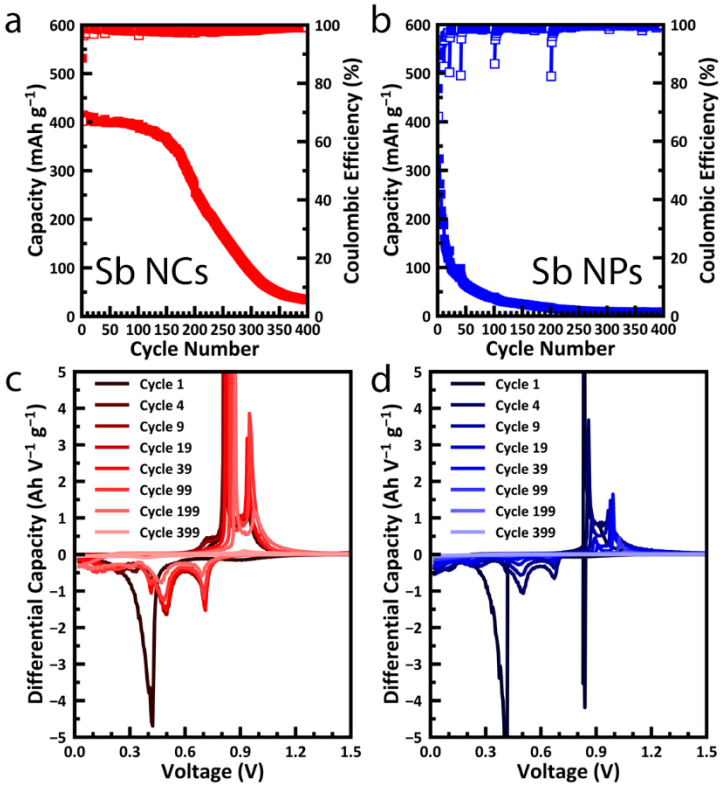

Figure 3-4. 1C non-GITT antimony nanocrystal-based negative electrode (a) capacity, and (c) differential capacity and antimony nanoplatelet-based negative electrode (b) capacity and (d) differential capacity indicating that 1C cycling is largely unaffected by the high-fidelity GITT.

3.3.2.1 *Isotropic Antimony Nanocrystal Thermodynamics and Kinetics during Extended Cycling*

The antimony nanocrystals cycled stably through cycle 100 with 95% capacity retention from cycle 3 to cycle 99 (Figure 3-4). The small initial capacity loss is primarily driven by increased non-kinetic difficulty for the electrochemical reactions. Between cycle 100 and cycle 200, kinetic limitations that reduce the ability to fully desodiate to pure antimony also start to play a role in the capacity losses, thereby increasing the rate of capacity loss.

The coulometric titration curves indicate whether capacity reductions are driven by increased thermodynamic or kinetic barriers (Figure 3-5). The kinetic difficulty of the electrochemical reactions is correlated with the width of the coulometric titration curve.[81,107] Thus, the coulometric titration curve is wider in regions where the electrochemical reactions are more difficult. Through cycle 100, where only a small amount of capacity decay occurs, the width of the coulometric titration curve does not change, suggesting that the capacity decline is primarily driven by non-kinetic barriers. At cycle 200, the width of coulometric titration curve in the region the desodiation electrochemical reactions in the region of 0.8 – 1.5 V has increased substantially, indicating that kinetic limitations have become more dominant (Figure 3-5a).[42] These kinetic limitations drive an increased rate of capacity loss by cycle 150. However, even at cycle 400 all of the initial reaction plateaus are still visible, indicating that much of active material in the electrode that is still cycling cycles fully between Sb and Na_3Sb even though the capacity loss rate has slowed (Figure 3-4). This observation suggests that the capacity losses for the whole electrode could be limited if the fraction of the sample that still cycles between Sb and Na_3Sb after extended cycling could be identified and the parameters associated with this fraction could be replicated across the electrode.

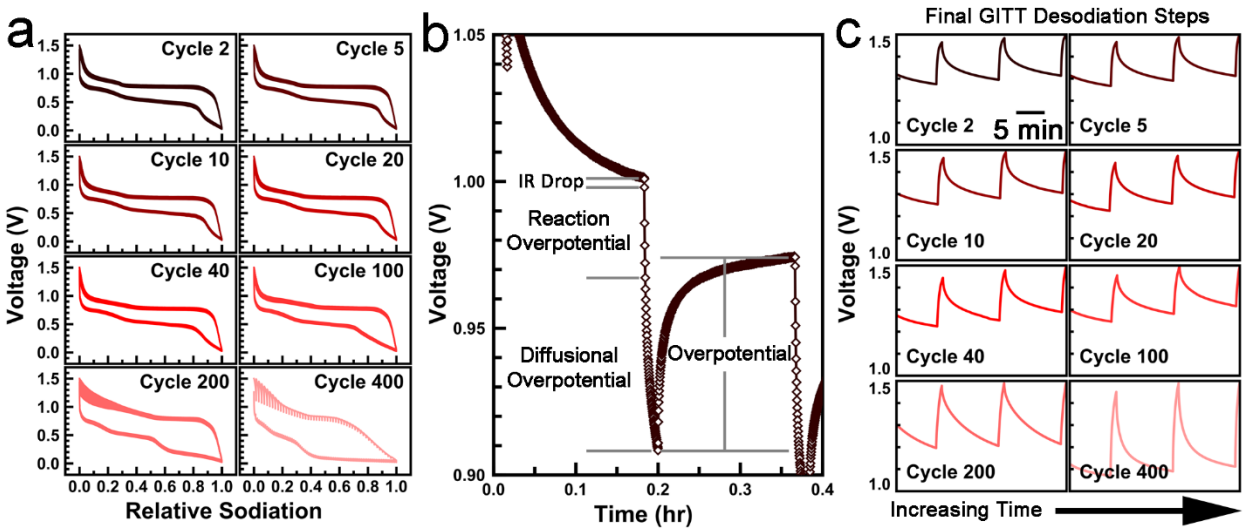

Figure 3-5. Sb nanocrystal-based electrode a) coulometric titration curves demonstrating minimal kinetic limitations through cycle 100, b) a characteristic GITT step showing the overpotential components that contribute to the kinetic limitations, and c) coulometric titration curves showing the final GITT desodiation steps, the most kinetically-limiteed steps after extended cycling. Relative sodiation state of 1.0 is defined as the maximum sodiation state reached a relative sodiation state of 0.0 is defined as the minimum sodiation state reached in a given sodiation or desodiation.

The time-based coulometric titration curves exhibit both the same width for the individual electrochemical reactions and approximately the same cycle time for each reaction step (plateau in the coulometric titration curve) and for the total reaction time, further validating the stability of the antimony nanocrystal-based electrode through cycle 100 (Figure 3-6a).

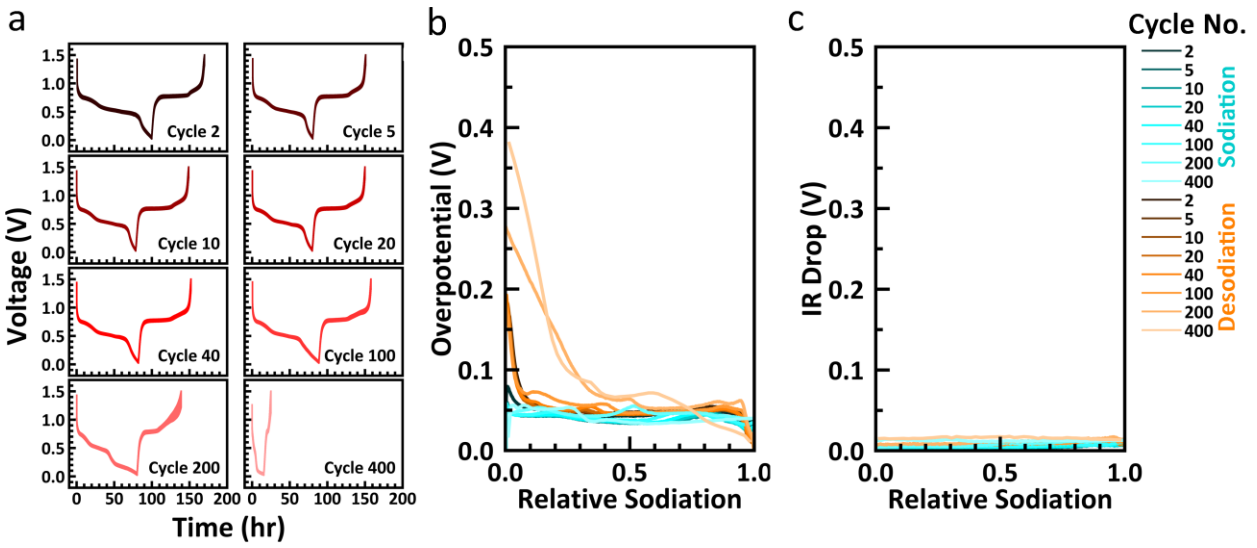

Figure 3-6. Sb nanocrystal-based electrode a) time-based coulometric titration curves further demonstrating that the electrochemical reaction plateaus remain the same through cycle 100 and b) overpotential and c) IR Drop together indicating that the cell resistance is not a major component of the kinetic limitations in the battery.

The source of the kinetic barrier to full desodiation after extended cycling can be identified via further examination of the coulometric titration curve for the antimony nanocrystal-based electrode. The kinetic limitations in the coulometric titration curves consist of three major components, an IR drop, a reaction overpotential and a diffusional overpotential (Figure 3-5b).[81] These components together lead to the overpotential of each GITT step (Figure 3-6).[107] The IR drop in a well-designed cell is the small voltage step change that occurs at the introduction of current to overcome the configurational resistance of the cell.[81] The IR drop is the vertical line in the current injection curve that occurs at the start of each current injection step in the time-based coulometric titration curve. At cycles 200 and 400, the IR drop is small relative to the overpotential at close to full desodiation, indicating that it is not the driver for the increased kinetic limitations (Figure 3-6). Furthermore, the IR drop close to full desodiation during cycle 200 is similar in value

to the IR drops close to full desodiation for cycles 2 through 100, further indicating that it is not leading to increased kinetic resistance. Therefore, either the reaction overpotential or the diffusional overpotential is leading to the increased kinetic barriers for full desodiation after extended cycling.

The reaction overpotential cannot be easily quantitatively determined via GITT.[81] However, the relative influences of the reaction overpotential and the diffusional overpotential can be qualitatively determined. The portion of the current injection step correlated with the reaction overpotential occurs directly after the IR drop and has a very steep slope, while the portion of the current injection step correlated with the diffusional overpotential occurs after the reaction overpotential and has a more gradual slope. In the coulometric titration curves close to full desodiation, the portion of the current injection steps with a gradual slope increases more than the portion of the current injection steps with a steep slope for cycles 200 and 400 relative to cycles 2 through 100, indicating that the diffusional overpotential is the dominant source for the increased kinetic limitations observed in cycles 200 and 400 (Figure 3-5c). Thus, the kinetic difficulty of reaching the fully desodiated state after extended cycling and the associated increase in capacity loss occurs because diffusion becomes more difficult.

The diffusion coefficients at each voltage further validate that diffusion is kinetically limiting performance after extended cycling (Figure 3-7). The details of these calculations are included in in section 3.3.2.4. Previously the diffusion coefficients for desodiation of an antimony thin film at close to the terminal sodiation state of Na_3Sb have been explored (0.1 to 0.7 V).[82] The diffusion coefficients in this region for the antimony nanocrystals are within one order of magnitude (~10^{-8} to 10^{-9} cm^2/s vs. ~10^{-8} to 10^{-10} cm^2/s in this study) of the previously observed diffusion coefficients for the antimony thin films and show the same shape across the voltage window validating our

diffusion coefficient calculations on both a qualitative and quantitative level (Figure 3-7b). The shapes of the diffusion coefficient curves also correlate with the shape of the differential capacity plots further validating the diffusion coefficient calculations. The diffusion coefficients are reduced by 2-3 orders of magnitude at low sodiation states during desodiation for cycles 200 and 400 relative to cycles 2 through 100, validating that the kinetic limitations are driven by a reduction in the diffusion coefficients (Figure 3-7b). Thus, after extended cycling, the diffusion of sodium ions out of the electrode is kinetically limited at low sodiation states, resulting in a sequestration of sodium in the electrode and in turn a loss of capacity at a C/10 cycling rate.

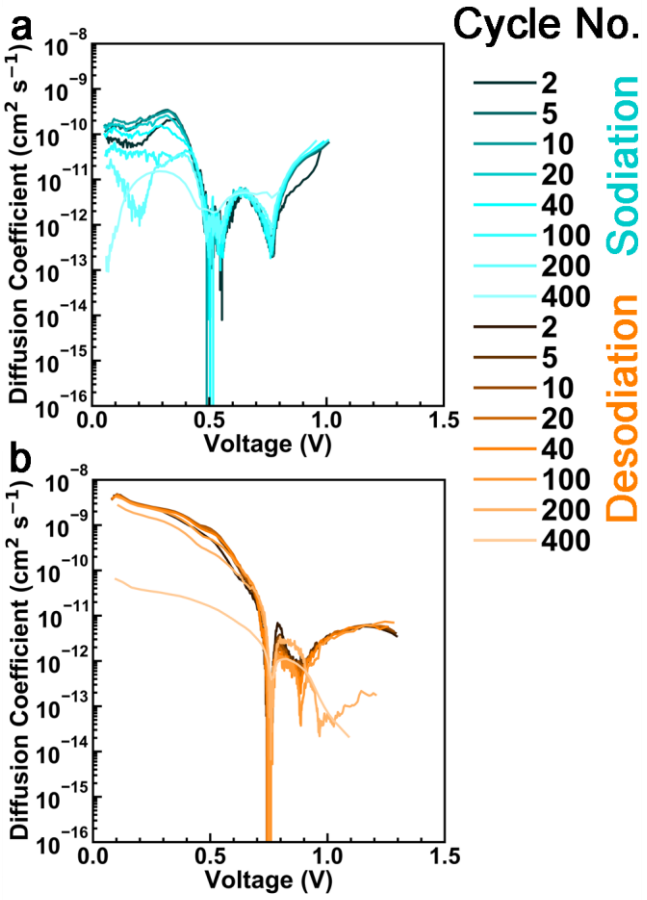

Figure 3-7. GITT-based a) sodiation and b) desodiation diffusion coefficients for an Sb nanocrystal-based electrode showing drop-offs close to the Na_3Sb terminal sodiation state during sodiation and throughout desodiation after extended cycling.

3.3.2.2 *Highly Anisotropic Antimony Nanoplatelets Thermodynamics and Kinetics during Extended Cycling*

The capacity of the antimony nanoplatelets decays rapidly, with this decay strongly correlated with increased kinetic limitations for full desodiation (Figure 3-4 and Figure 3-8). These kinetic limitations can be clearly seen as early as cycle 5 in the coulometric titration curves and worsen rapidly with extended cycling, affecting a wider sodiation range as cycle number increases. In

addition, increased kinetic limitations occur during sodiation, becoming visually apparent by cycle 100 although these limitations are small relative to the kinetic difficulty during desodiation.

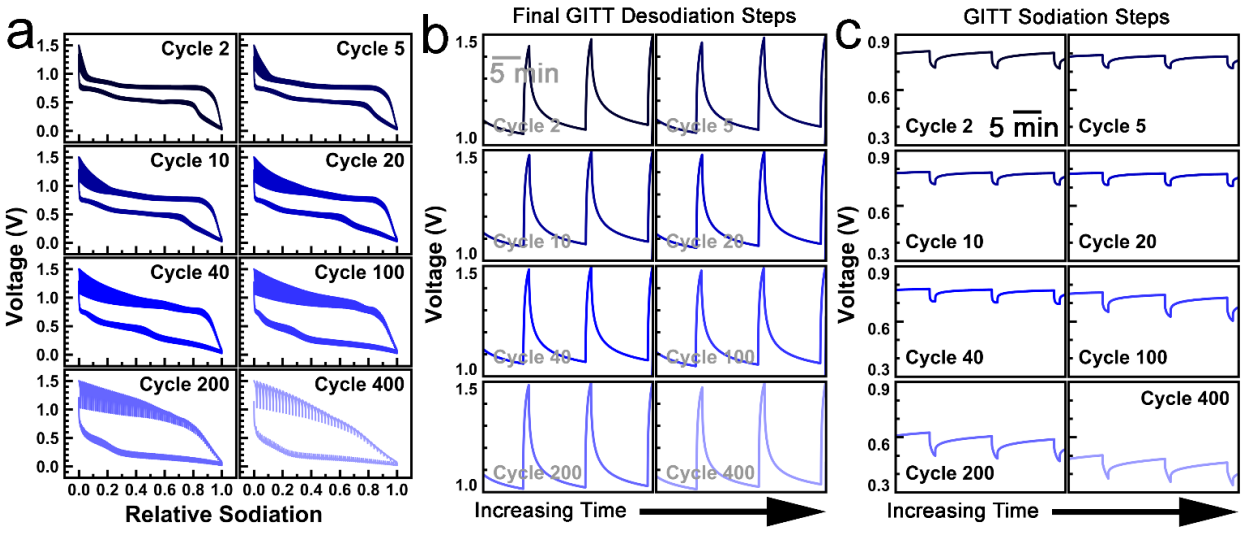

Figure 3-8. Sb nanoplatelet-based electrode a) coulometric titration curves demonstrating signficant kinetic limitations beginning before cycle 5, b) coulometric titration curves for final GITT desodiation steps indicating these limitations occur due to both reaction and diffusional overpotentials, and c) coulometric titration curves for the GITT sodiation steps between 0.5 and 1 hr showing increased diffusional overpotentials upon extended cycling.

The time-based coulometric titration curves demonstrate that the rapid drop-off in capacity for the highly anisotropic antimony nanoplatelets results in less current flow through all of the electrochemical reactions (plateaus) (Figure 3-4 and Figure 3-9). The reactions at low sodiation states during sodiation and at high sodiation states during desodiation are most strongly affected, suggesting that the cycling window narrows for the highly anisotropic antimony nanoplatelets with much of the sample not cycling fully between Sb and Na_3Sb. The IR drop is a small percentage of

the overpotential at all sodiation levels for the antimony nanoplatelets, indicating that the IR drop is not the driver for kinetic limitations during cycling (Figure 3-9).

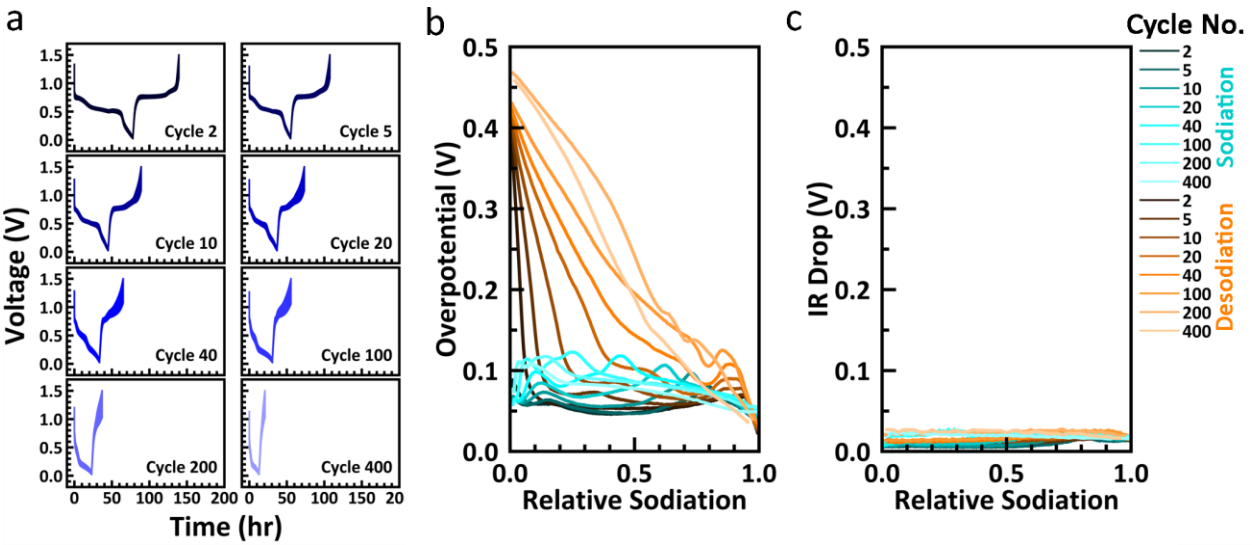

Figure 3-9. Sb Nanoplatelet-based electrode a) time-based coulometric titration curves demonstrating that less current is flowing through all the electrochemical reactions as capacity decays and b) overpotential and c) IR Drop together indicating that the cell resistance is not a major component of the kinetic limitations in the battery.

The kinetic limitations during both sodiation and desodiation are driven by large increases in both the reaction overpotential and diffusional overpotential (Figure 3-8a,b). As discussed in section 3.3.1.1 the nanoplatelets are highly strained during cycling. Strain strongly affects activation energies (kinetic barriers) of reactions and in turn the reaction rates.[108] Strain speeds up the reaction kinetics when it helps to align the system into an ideal configuration for reaction (typically closer to the reaction intermediate state) and slows down the reaction kinetics when it moves the system configuration further away from the ideal. In the case of the antimony nanoplatelets, the increased kinetic barriers for desodiation at low desodiation states and for

sodiation after cycle 20 combined, suggest that the sharp reaction interfaces in the strained antimony nanoplatelets move the system away from the ideal reaction configuration (Figure 3-8b).

The diffusion coefficients can also be positively or negatively affected by strain.[109–112] Strain reduces the diffusion barrier when the lattice becomes more favorably aligned with the diffusion pathways and increases the diffusion barrier when the opposite occurs. In the case of the antimony nanoplatelets the strain is leading to increased diffusional barriers again for desodiation at low desodiation states and for sodiation after cycle 20, based on the observed diffusional overpotentials and diffusion coefficients (Figure 3-8b and Figure 3-10). Therefore, both the lowered diffusion coefficients and increased reaction barriers indicated by the overpotentials are caused by the strain in the antimony nanoplatelets. The details of these calculations are included in in section 3.3.2.4.

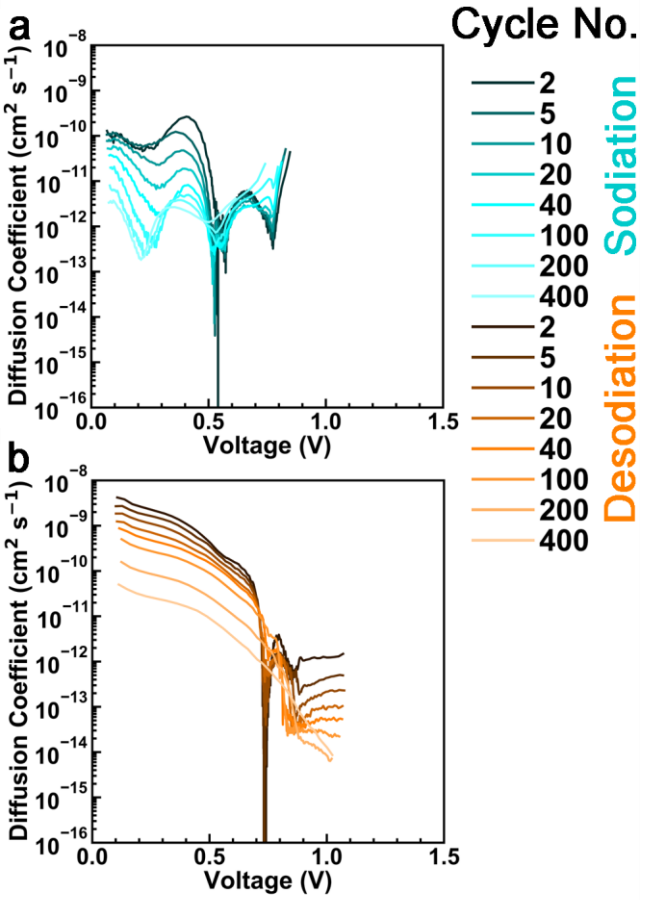

Figure 3-10. GITT-based a) sodiation and b) desodiation diffusion coefficients for an Sb nanoplatelet-based electrode showing diffusion coefficient drop-offs close to the Na_3Sb terminal sodiation state during sodiation and during desodiation throughout cycling.

The strain-induced reduction in diffusion coefficients and increase in reaction barriers are largest during desodiation close to the terminal sodiation state, resulting in sequestration of sodium in antimony. The kinetic hinderance becomes particularly strong at ~0.9 V, which corresponds to the start of the voltage window recrystallization of antimony from a-NaSb.[42] Allan et al. have previously observed that this recrystallization does not fully occur for up to 70% of the active material remains as a-NaSb, which would correspond to a fully utilized active material capacity of

~500 mAh g^{-1}.[42] Therefore significant regions of the antimony active material are amorphous even at the upper cutoff voltage. This stress of the a-NaSb to c-Sb transition is the largest stress that occurs during desodiation (section 3.3.1.1), and therefore, the a-NaSb to c-Sb reaction is the first desodiation that is adversely affected by the increased strain in the nanoplatelets. The strain-induced reduction in diffusion coefficients and increase in reaction barriers seen in the nanoplatelets exacerbates the lack of full utilization of the active material, leading to increased sequestration in a-NaSb and a loss of capacity.

However, even if the active material stops reaching the c-Sb phase entirely, the capacity of the fully utilized active material would still be 440 mAh g^{-1}. Therefore, additional sources of capacity loss must occur. One major source of this additional capacity loss is the strain-induced reduction in diffusion coefficients.[109–112] Strain and the diffusion barrier (diffusional overpotential) are correlated for antimony with larger strains leading to an increased diffusion barrier, when examined by comparing Li_3Sb to Na_3Sb.[82] In cases where the strain and diffusion barrier are positively correlated increased capacity loss occurs because the diffusing ions are less uniformly distributed within the active material, leading to increased stress and stress-induced damage.[110] The stress-induced damage and capacity loss comes in the form of active material disconnection from the current collector and increased SEI layer formation.[22,24,27] In the antimony nanoplatelets, the initial diffusion barrier to full desodiation is strain-induced. The diffusion barrier leads to stress-induced damage and capacity reduction. The stress-induced damage in turn causes increased kinetic and thermodynamic barriers (Figure 3-8). The increased thermodynamic and kinetic barriers then lead to further stress-induced damage, with this feedback loop resulting in an almost full loss of capacity by cycle 200.

This feedback loop can be clearly observed via the drop-off in diffusion coefficients for the antimony nanoplatelets (Figure 3-10). For cycle 2, the diffusion coefficients match well with the literature both numerically (~10^{-9} cm^2 s^{-1} at c-Na_3Sb) and qualitatively (drops off between 0.1 and 0.7 V).[82] After cycle 2, the diffusion coefficients drop off continuously as shown for the Na_3Sb and Sb states during sodiation and desodiation.

3.3.2.3 ***Morphology-driven kinetics and decay pathways***

The model system of isotropic antimony nanocrystal and highly anisotropic antimony nanoplatelet-based electrodes offers significant insight into the fundamental drivers of stable cycling for antimony. The isotropic antimony nanocrystals exhibit significantly higher capacity retention than the highly anisotropic antimony nanoplatelets, which we attribute in section 3.3.1.1 to the increased strain observed in the antimony nanoplatelets. The GITT analysis further validates that assertion, demonstrating that the increased strain in the antimony nanoplatelets causes both an increased diffusional barrier and an increased reaction overpotential for the desodiation of sodium antimonide, which is not present for the isotropic antimony nanocrystals early in cycling. This in turn leads to an increased rate of capacity reduction for the antimony nanoplatelets. As described above, the initial diffusional barrier strongly drives this increased rate of capacity reduction, by leading to further increases in the desodiation barrier as cycling continues. Unlike the highly anisotropic antimony nanoplatelets, the antimony nanocrystal capacity loss is initially driven by increased non-kinetic barriers. Eventually, the diffusional barrier increases to the point where the same feedback loop observed for the antimony nanoplatelets occurs and like with the nanoplatelets the sodium becomes sequestered in sodium antimonide. However, even during capacity degradation, the reaction overpotential for the antimony nanocrystals does not contribute as strongly as it does for the antimony nanoplatelets. After 400 cycles, both the antimony

nanoplatelets and antimony nanocrystal capacity is substantially reduced, but the coulometric titration curves exhibit different behavior, with the antimony nanocrystal curve more strongly exhibiting all the major reaction plateaus (indicators of each electrochemical reaction) that are present during initial cycling (Figure 3-4, Figure 3-6, and Figure 3-9). This suggests that the antimony nanocrystals are less likely to experience partial sodiation or desodiation than the antimony nanoplatelets, even during degraded cycling. Overall, the morphology-driven differences in cycling performance are attributable to the strain-impeded kinetics of the electrochemical cycling.

3.3.2.4 ***Diffusion Coefficient Calculations from GITT***

The diffusion coefficients can be calculated based upon the GITT data to provide a quantitative measure of the solid-state diffusion. Assuming Fickian diffusion, the diffusion coefficient can be determined using the following equation

$$D = \frac{4}{\pi}\left(\frac{iV_m}{z_A FS}\right)^2 \left[\frac{\left(\frac{dE}{d\delta}\right)}{\left(\frac{dE}{d\sqrt{t}}\right)}\right]^2 \qquad t \ll \frac{L^2}{D} \qquad 3\text{-}8$$

where D is the solid-state diffusion coefficient, i is the current, V_m is the molar volume of the electrode, z_A is the charge number, F is Faraday's constant, S is the electrochemically active electrode surface area, $\frac{dE}{dx}$ is the slope of the equilibrium potentials, the last voltages in rest steps of the coulometric titration curve before current resumes, and $\frac{dE}{d\sqrt{t}}$ is the slope of the linearized charging steps in the coulometric titration curve, t is the time and L is the size of the electrode material in the diffusion direction.[113]

The surface area, the volume expansion and two-phase transitions in composite electrodes with an alloying active material introduce additional complications into calculating the diffusion coefficients from GITT. However, these additional complications can be compensated for by

modifying the basic diffusion coefficient calculations. In a composite electrode comprised of nanomaterials, the electrochemically active surface area is often substantially larger than the superficial surface area of the current collector.[114] However, the nonactive components of the electrode confound establishing an electrochemically active surface area via non-electrochemical methods such as Brunauer-Emmett-Teller (BET) gas adsorption, because these types of measurements include the surface area of the nonactive components as part of the total surface area.[115] There is currently significant research focused on developing models and analysis techniques that better access the electrochemically active surface area to support more accurate diffusion coefficient calculations for a broader array of active materials and composite electrode morphologies.[114–116] These approaches involve techniques such as 3D tomography to develop detailed models of the composite or SEM examination of electrodes stained with chemicals that only bind to electrochemically active areas.[114–116] To our knowledge, these types of approaches have not yet been employed for antimony nanomaterial-based electrodes and these techniques are outside the scope of this paper. However, we can provide an upper and lower bound for the surface area that in turn establishes an upper and lower bound for the diffusion coefficient. The superficial surface area of the copper current collector is typically smaller than the electrochemically active surface area of the composite electrode on the copper current collector, because the composite electrode is a 3D porous material while the superficial surface area of the current collector is 2D. Therefore, the diffusion coefficients calculated with the copper current collector superficial surface area (1.77 cm^2) represent an upper bound for the possible diffusion coefficient range (Figure 3-7 and Figure 3-10).

We established a lower bound on the diffusion coefficients by calculating a maximum surface area for both the antimony nanoplatelets and antimony nanocrystals, based upon the

assumption that all of the surface area of the nanomaterial is active (Figure 3-11). We calculated the surface area at a given sodiation state via the following equation

$$S = (1 - x)S_{Sb} + xS_{Na_3Sb} \quad 3\text{-}9$$

where x is the relative sodiation level such that the maximum sodiation state reached during a given sodiation or desodiation step is one and the minimum sodiation state reached during a given sodiation or desodiation step is zero, S_{Sb} is the surface area of the unsodiated antimony active material and S_{Na_3Sb} is the surface area of the antimony active material sodiated to Na_3Sb. For the antimony nanoplatelet geometry we used a regular hexagon. Based upon the density of antimony and the electrode active material weight we calculated the total volume of antimony nanomaterial in the electrode using the following equation

$$V_{Sb} = \rho_{sb} m_{sb} \quad 3\text{-}10$$

where m_{Sb} is the antimony weight in the electrode, ρ_{sb} is the density of antimony and V_{Sb} is the total volume of antimony in the electrode. For the antimony nanoplatelets we calculated the volume of an individual antimony nanoplatelet using a regular hexagon with a 100 nm thickness and 1 µm tip to tip width with the equation

$$V_{SbNP} = \frac{3\sqrt{3}}{2} a^2 h \quad 3\text{-}11$$

where h is the thickness of the antimony nanoplatelet, a is half of the tip to tip platelet width and V_{SbNP} is the volume of a single nanoplatelet. The Wulff shape of the nanoplatelets does have sloped sides, however both the volume and surface area provided by the sloped sides are small compared to the volume and surface area provided by the platelet faces given the order of magnitude difference between the platelet width and thickness, validating the assumption that the antimony nanoplatelets are a regular hexagon.[74,117]

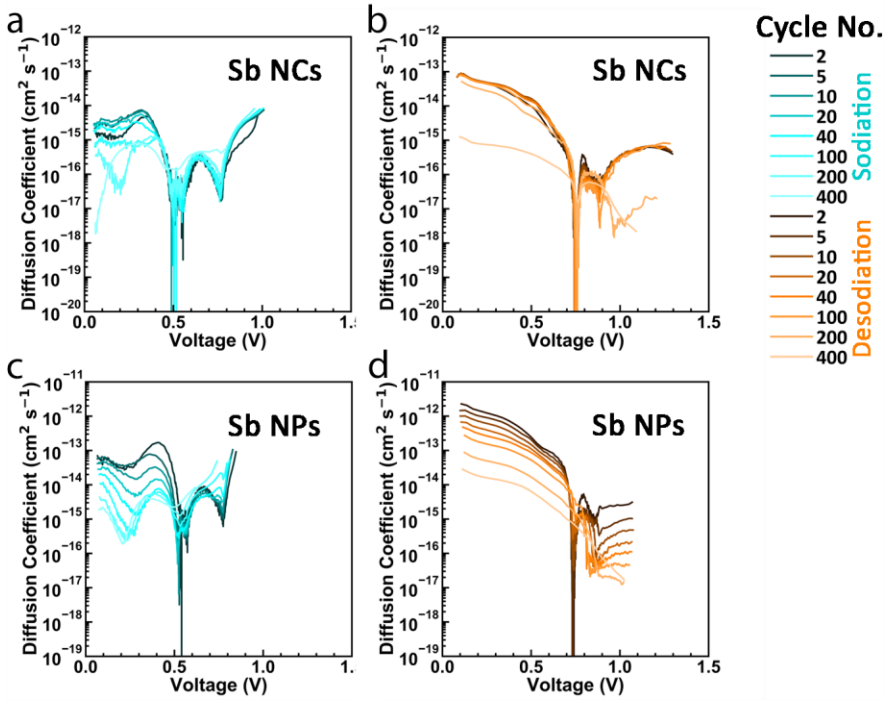

Figure 3-11. Surface area adjusted Sb nanocrystal-based electrode a) sodiation and b) desodiation diffusion coefficients and Sb nanoplatelet-based electrode c) sodiation and d) desodiation diffusion coefficients showing quanitatively lower, but qualitatively similar values to the surface area unadjusted diffusion coefficients.

We assumed the antimony nanocrystals were spherical with a 40 nm diameter when calculating the volume of an individual nanocrystal. We calculated the volume of an individual nanocrystal based on the following equation

$$V_{SbNC} = \frac{4}{3}\pi r^3 \qquad 3\text{-}12$$

where r is the nanocrystal radius. Dividing the total antimony volume by the single antimony nanostructure volume gives the total number of antimony nanoplatelets in the sample

$$N_{SbNS} = \frac{V_{Sb}}{V_{SbNS}} \qquad 3\text{-}13$$

where N_{SbNS} is the number of nanostructures in the sample and V_{SbNS} is the volume of an individual nanostructure. Based on the number of nanoplatelets we can calculate the total nanoplatelet surface area with the following equation:

$$S_{Sb} = N_{SbNS}\left(6ah + 3\sqrt{3}a^2\right) \quad 3\text{-}14$$

and the total nanocrystal surface area with the following equation

$$S_{Sb} = N_{SbNS}(4\pi r^2) \quad 3\text{-}15$$

where S_{Sb} is the surface area of the unaggregated electrode active material before sodiation. The surface area of the sodiated Na_3Sb can then be calculated based upon the known expansion in the a, b and c directions for the antimony nanoplatelets, such that the height increases 2.5 times and the width increases by 1.3 times giving

$$S_{Na_3Sb} = N_{SbNS}\left(6 \cdot 1.3a \cdot 2.5h + 3\sqrt{3}(1.3a)^2\right) \quad 3\text{-}16$$

and for the antimony nanocrystals using a volume expansion of 3.9 giving

$$S_{Na_3Sb} = N_{SbNS}\left(4\pi\left(\sqrt[3]{3.9}r\right)^2\right) \quad 3\text{-}17$$

where S_{Na_3Sb} is the surface area of the unaggregated electrode active material after sodiation.[66,99] Inserting these surface areas into equation 3-8 provides the unaggregated surface area for a given sodiation state. The lower bound for the diffusion coefficients is based on these unaggregated surface areas (Figure 3-11c-f).

Additionally, the molar volume term V_m in the diffusion coefficient calculation must be adjusted based upon the sodiation state. For all of the differential capacity cycles observed, some fraction of the electrode cycles between unsodiated and terminally sodiated to Na_3Sb (Figure 3-4). Therefore, the molar volume for the diffusion coefficient calculation is the antimony molar volume at the start of sodiation and end of desodiation and the Na_3Sb molar volume at the end of sodiation

and the start of desodiation. In between, we assume that expansion occurs linearly across the sodiation range and modified the molar volume term accordingly such that

$$V_m = (1 - x)V_{m,Sb} + xV_{m,Na_3Sb} \quad 3\text{-}18$$

where x is the relative sodiation level such that the maximum sodiation state reached during a given sodiation or desodiation step is one and the minimum sodiation state reached during a given sodiation or desodiation step is zero, $V_{m,Sb}$ is the molar volume of antimony (18.18 cm^3/mol) and V_{m,Na_3Sb} is the molar volume of Na_3Sb (71.44 cm^3/mol).[66,99] While the exact molar volume for the intermediate states may not be accurately modeled with a linear interpolation, the molar volumes of antimony and Na_3Sb bound the molar volumes of the intermediate states and thus the diffusion coefficients of antimony and Na_3Sb also bound the intermediate diffusion coefficients.

The large drop-offs in diffusion coefficients at ~0.5 V during sodiation and ~0.75 V during desodiation occur during two-phase reaction regions as shown in the differential capacity plots (Figure 3-4, Figure 3-7, and Figure 3-10). Two-phase reactions violate the assumption of Fickian diffusion that the diffusion coefficient calculations rely upon, resulting in the large observed drop-off in diffusion coefficient.[118] These drop-offs are driven by the phase transformation that occur at the two-phase interface not drop-offs in the diffusion coefficients. Thus, these regions do not provide accurate diffusion coefficients via standard GITT analysis. However, these regions are not kinetically limiting during capacity loss as evidenced by the coulometric titration curves and therefore are not of primary interest for this study (Figure 3-5 and Figure 3-8). Overall, the modifications made to the standard diffusion coefficient calculation provide accurately bounded diffusion coefficients at the low sodiation states that are the primary kinetic source of capacity losses for both the nanocrystals and nanoplatelets.

3.4 Electrode Conductivity and Compositional Mapping

Active material morphology affects the composite structure of the electrode, particularly the heterogeneity and in turn this heterogeneity affects the conductivity (Figure 3-12). The antimony nanoplatelets have a more heterogenous distribution of chemical components when compared to the antimony nanocrystals (Figure 3-12a,b). Electrode heterogeneity is driven by chemical and physical differences in the electrode materials during electrode fabrication.[86] For the antimony nanomaterial composites, the same binder and conductive carbon were used in the same mass fractions. Therefore, the major differences are caused by the active materials.

The nanoplatelets and nanocrystals have substantially different size dispersions and morphology and are synthesized in different solvent media with different precursors, likely resulting in substantially different surface chemistry. Each of these material properties can affect the electrode composite heterogeneity.[83–87,119] The antimony nanoplatelets have a larger size dispersion and are more anisotropic than the antimony nanocrystals. Both an increase active material size dispersion and anisotropy in the active material have been shown to increase electrode heterogeneity.[83–85,119] In addition, the surface chemistry can introduce heterogeneity in cases where it leads to aggregation of the active material during electrode fabrication.[86] While the surface chemistry has not been interrogated for the nanoplatelets and nanocrystals, visual observation of the electrode fabrication process suggests that less active material aggregation occurs for the antimony nanocrystals. Therefore, the observed heterogeneity of the nanoplatelet electrode is driven by the particle size dispersion, anisotropy and surface chemistry.

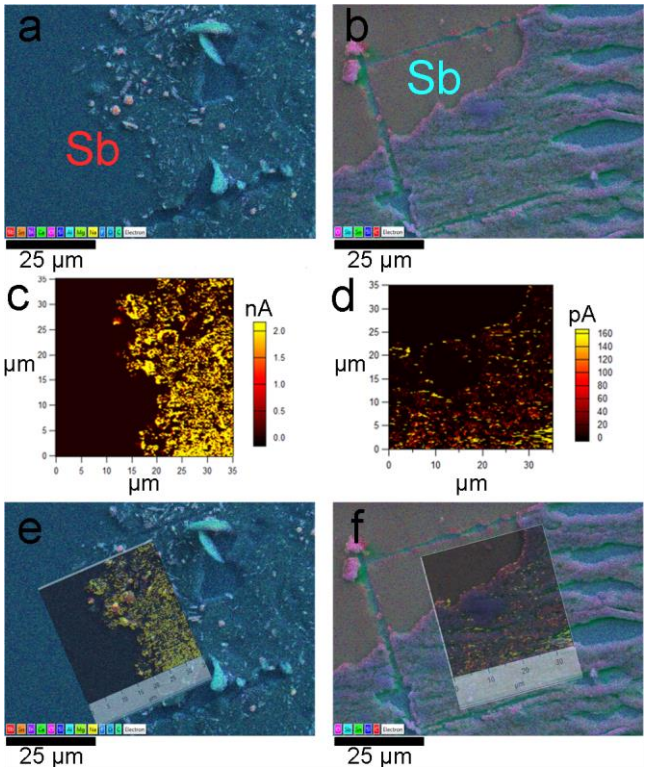

Figure 3-12. SEM with EDXS mapping of a) an antimony nanoplatelet-based electrode and b) an antimony nanocrystal-based electrode, C-AFM mapping of c) the antimony nanoplatelet-based electrode and d) the antimony nanocrystal-based electrode, and an overlay of the C-AFM on the SEM with EDXS for e) the antimony nanoplatelet-based electrode and f) the antimony nanocrystal-based electrode after epoxying and microtoming demonstrating strong correlations between chemical and conducivity heterogenity.

The conductivity of the electrode samples closely aligns with the chemical signatures with the antimony nanoplatelet-based electrode showing significantly more heterogeneity in its conductivity map (Figure 3-12c,d). Heterogenous conductivity at the nano and micro scales has previously been tied to reduced bulk scale performance, since for much of the sample active material the electron transport pathways to the current collector and ion-diffusion path lengths are longer than in a homogenously mixed sample.[86] Thus, the increased physical and electrical

heterogeneity of the antimony nanoplatelets relative to the antimony nanocrystals indicates that the electrode composite morphology leads to reduced performance in the antimony nanoplatelet-based electrodes.

3.5 Conclusions

In Chapter 3, we use the highly anisotropic antimony nanoplatelets as a model system to study the impacts of morphology on the electrochemical sodiation nanostructured antimony. Relative to small, isotropic antimony nanocrystals, the antimony nanoplatelets experience significantly more strain during cycling, leading to increased crystallization and suppression of amorphous phases – most notably, suppression of the previously unassigned a-$Na_{3-x}Sb$ desodiation peak that occurs at 0.72 V. In addition, using a high-fidelity galvanostatic intermittent titration technique we demonstrate that this leads to increased strain-driven kinetic overpotentials above ~0.9 V in the highly anisotropic antimony nanoplatelets that occur immediately upon cycling. Through this analysis we elucidate that these kinetic hindrances are the source of the previously observed difficulty in desodiation beyond a-NaSb.[42] We also find that for both the antimony nanocrystals and antimony nanoplatelets, the diffusional overpotential during desodiation at voltages greater than ~0.9 V correlates strongly with the capacity reductions. These results suggest that minimizing the diffusional overpotential at voltages greater than ~0.9 V is critical to increasing both capacity and capacity retention in antimony electrode materials. Furthermore, we find that the anisotropy and size dispersion of the antimony nanoplatelets leads to unfavorable electrode heterogeneity that also negatively impacts performance. Therefore, controlling the morphology of antimony-based active materials is critical to obtaining high performance both on an individual

particle level and on an electrode composite level, with decreased anisotropy driving increased performance at both levels.

Chapter 4: In Situ XRD of Antimony Na-Ion Battery Electrodes After Extended Cycling

4.1 Introduction

In Chapter 4, we use *in situ* XRD to identify a previously unidentified peak that occurs at ~0.93 V in the differential capacity data for both anisotropic nanoplatelets and isotropic nanocrystals after extended cycling (Figure 3-1 and Figure 3-2). Previous antimony related phase identification efforts have focused primarily on the first few cycles, which occur before this peak forms and so have not interrogated samples where the electrochemical event that leads to the peak is present.[38,42,44] *In situ* XRD measurements combined with recent calculations in the literature, suggest that the ~0.93 V peak can be attributed to the desodiation of crystalline NaSb, which becomes increasingly prominent upon extended cycling.[43] Crystalline NaSb is a thermodynamically favorable, but largely undiscussed source of capacity in antimony electrodes.

4.2 Experimental Methods

4.2.1 Materials.

Propylene carbonate (99.7%), sodium metal (>99.99%, dry cubes, ACS Specification), sodium carboxymethyl cellulose (CMC) (M_w ~90,000), toluene (anhydrous, 99.8%), and triphenylantimony (≥99.0%) were purchased from Sigma Aldrich. Sodium perchlorate (≥98%) was purchased from Fisher Scientific. Fluoroethylene carbonate (≥98%) was purchased from TCI America. Carbon black (Vulcan XC72R) was purchased from Cabot Corporation and stored in a vacuum oven at 80°C. Aluminum foil (99%, 4-µm-thickness) was purchased from Lebow Company. All reagents were used as received without further purification.

4.2.2 Supercritical-Fluid-Based Synthesis of Nanostructured Antimony.

In a typical synthesis, a stock solution of triphenylantimony (5 g) dissolved in anhydrous toluene (10 mL) was prepared in an inert-atmosphere nitrogen glove box. A nitrogen-filled, continuous-flow-through supercritical reactor with a 10 mL internal volume was heated to 425°C and pressurized to 900 psig with anhydrous toluene (See Ref. 67 for further details of the supercritical reactor system).[67] The triphenylantimony stock solution (720 μL, 1.42 M) was diluted in 11.3 mL of anhydrous toluene, drawn into a syringe, and subsequently loaded into a 10-mL injection coil leading to the reactor inlet. The triphenylantimony precursor solution was then injected into the reactor at a rate of 0.5 mL/min for 20 min at 425°C and 900 psig. After completion of the reaction, the reactor was cooled to room temperature, and the product was collected and stored under ambient conditions.

4.2.3 Electrode Fabrication, Coin Cell Assembly, and Electrochemical Testing.

Electrodes were fabricated with a 64:21:15 mass ratio of antimony:carbon-black:carboxymethylcellulose. Using standard electrode fabrication procedures, the antimony active material, conductive carbon, and polymeric binder were combined in the above mass ratio and mixed into a slurry with deionized water using a mortar and pestle.[16,17,88,89] In a typical fabrication, 150 mg of antimony, 49 mg of carbon black, 0.52 mL of CMC in deionized water (0.067 g/mL), and 0.4 mL of additional deionized water were mixed. The volume of deionized water added was adjusted as needed to achieve the desired slurry concentration. The slurry was then doctor-bladed (38 μm thickness) onto a copper foil current collector (aluminum foil for *in situ* XRD experiments) and dried on a hot plate at 80°C in air until no observable moisture was present. Electrodes were further dried in a vacuum oven (80°C, less than 15 mbar) and stored until ready

for use. 15-mm-diameter electrodes were punched out and stored in the vacuum oven (80°C, less than 15 mbar) as needed. CR2032-type coin cells were assembled into half cells in an argon-filled glovebox using elemental sodium metal as the positive electrode, a glass fiber separator (Whatman, grade gf/f), and 1.0 M $NaClO_4$ in an electrolyte solution of 90% w/v propylene carbonate and 10% w/v fluoroethylene carbonate. Electrochemical testing was performed with a MACCOR Series 4000M 64-Channel Automated Battery Test System using a 1C cycling rate that corresponds to a current density of 660 mA g^{-1}. *In situ* XRD patterns were collected with a Bruker D8 Advance diffractometer with a Lynxeye X-ET detector using Cu Ka radiation while the *in situ* cell was cycled with a Princeton Applied Research VersaSTAT 4 at a 1C rate. Gravimetric capacities were calculated based on the weight of the active material.

4.2.4 Materials Characterization.

The crystal structures of Sb, NaSb, and Na_3Sb were modeled using VESTA software along with crystallographic data from the American Mineralogist Crystal Structure Database.[66,68,69,99,120] The crystal habit models were generated using the Great Stella software package and VESTA, again with crystallographic data from the American Mineralogist Crystal Structure Database. [66,68–70,99,120]

4.3 Results and Discussion

4.3.1 In Situ XRD of Antimony Na-Ion Battery Electrodes after Extended Cycling.

In situ XRD measurements for observations of phase transformations in antimony electrode materials have typically focused on the first few cycles, thus precluding any analysis of the observed electrochemical feature that occurs at 0.93 V after extended cycling. Here we carry out *in situ* XRD measurements after repeated cycling of the antimony electrodes in order to maximize

the intensity of the suspected crystalline two-phase transition at 0.93 V. For *in situ* measurements, both nanoplatelet- and nanocrystal-based composite electrodes were cast onto a 4-μm-thick aluminum foil current collector (in order to maximize X-ray transparency), assembled into an *in situ* half cell (LRCS *in situ* cell, beryllium window, provided by Bruker), and cycled repeatedly at a rate of 1C, until the electrochemical feature previously observed at 0.93 V was predominant. With the thin aluminum current collector and the *in situ* cell configuration, the electrodes degraded substantially faster than in the CR2032 coin cells where the 0.93 V peak was very prominent by cycle 40 for the antimony nanoplatelets and cycle 200 for the antimony nanocrystals (Figure 3-1 and Figure 3-2). In contrast, for the *in situ* cell configuration, 0.93 V feature in the differential capacity plot dominated after only 10 cycles (Figure 4-2c,d). In addition, all of the desodiation reactions are shifted to slightly higher potentials due to the increased cell resistance of the *in situ* half-cell configuration, with the reaction of interest at ~0.97 V (Figure 4-2d).

After aging the cells for 10 cycles, the *in situ* XRD analysis was carried out by holding the voltage at 0.02 V until the current declined by approximately an order of magnitude (~10 minutes), followed by collecting *in situ* XRD data for ~2 hours, and then repeating for additional voltage holds at 0.93 V and 1.5 V (Figure 4-1). Holds at 0.02 V and 1.5 V were selected in order to maximize signal from the c-Na_3Sb and c-Sb phases present in the cell, respectively, while the hold at 0.93 V was selected in order to maximize desodiation of the c-Na_3Sb phase (thus decreasing its XRD signal), while preserving the phase associated with the unidentified desodiation peak (which is shifted to a slightly higher potential for the *in situ* cell configuration, as discussed above). Although it proved exceedingly difficult to make definitive XRD peak assignments for electrodes fabricated from the spherical antimony nanocrystals due to the small grain size of the active material, the micrometer-scale lateral dimensions of the platelets proved significantly

advantageous with respect to acquiring interpretable *in situ* XRD signal. Consequently, the analysis that follows centers entirely on *in situ* XRD experiments carried out on Na-ion battery alloying electrodes fabricated from the highly anisotropic antimony nanoplatelets (Figure 4-1).

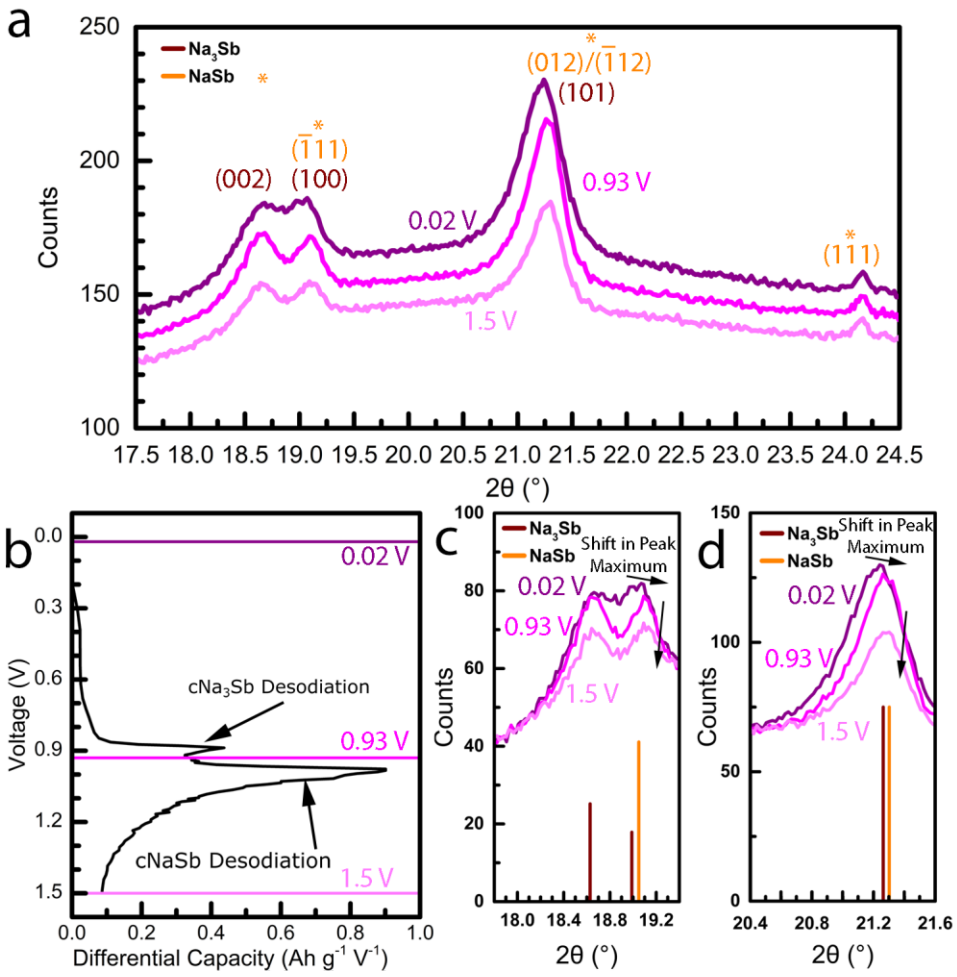

Figure 4-1. (a) *In situ* XRD measurements of antimony nanoplatelets, collected after 10 aging cycles at 1C, at desodiation potentials of 0.02 V, 0.93 V, and 1.5 V, tracking changes in the peaks associated with Na_3Sb and NaSb as a function of desodiation. (b) Differential desodiation capacity during cycle 10, illustrating the state of the electrochemical cell during each voltage hold, and (c,d) detailed views of the *in situ* XRD peaks that correspond to changes in the Na_3Sb and NaSb content

of the electrode (Na_3Sb PDF#: 03-065-3523, NaSb PDF#: 01-074-0801, Sb PDF#: 00-035-0732).[72,99,120]

Although numerous components present within the *in situ* experimental setup confound large portions of the *in situ* XRD pattern at high angles (Figure 4-2), features in the 17.5° to 24.5° 2θ region remain largely unperturbed. In particular, diffraction peaks at 18.6°, 19.1°, 21.3°, and 24.2° are clearly visible (Figure 4-1), with minimal interference from the components of the *in situ* setup (Figure 4-2). While the diffraction peak at 18.6° can be unambiguously attributed to reflections from the (002) planes of $P6_3/mmc$ c-Na_3Sb (PDF#: 03-065-3523), the diffraction peak at 24.2° can only be assigned to the (111) reflections from $P2_1/c$ c-NaSb (PDF#: 01-074-0801), clearly indicating that c-NaSb is also present, as no other cell components have reflections at this position.[99,120] Interestingly, this peak does not change in strength substantially during cycling. This indicates that a significant fraction of the c-NaSb does not desodiate during cycling. c-NaSb has not been previously observed to form during early stable cycling of antimony active materials, because the crystallization from a-NaSb to c-NaSb is kinetically slow.[38,43] The lack of desodiation from a significant fraction of the c-NaSb for the antimony nanoplatelet active material indicates that active material is electrochemically isolated. This suggests that a significant fraction of the c-NaSb is forming when a-NaSb becomes electrochemically isolated during degradation in the cell and therefore has time to crystallize to c-NaSb. The remaining peaks at 19.1° and 21.3° correspond to overlapping signals from c-Na_3Sb (100) reflections convoluted with c-NaSb ($\bar{1}11$) reflections and c-Na_3Sb (101) reflections convoluted with c-NaSb (012) and ($\bar{1}12$) reflections, respectively, with the c-NaSb diffraction peaks occurring at slightly higher angles.

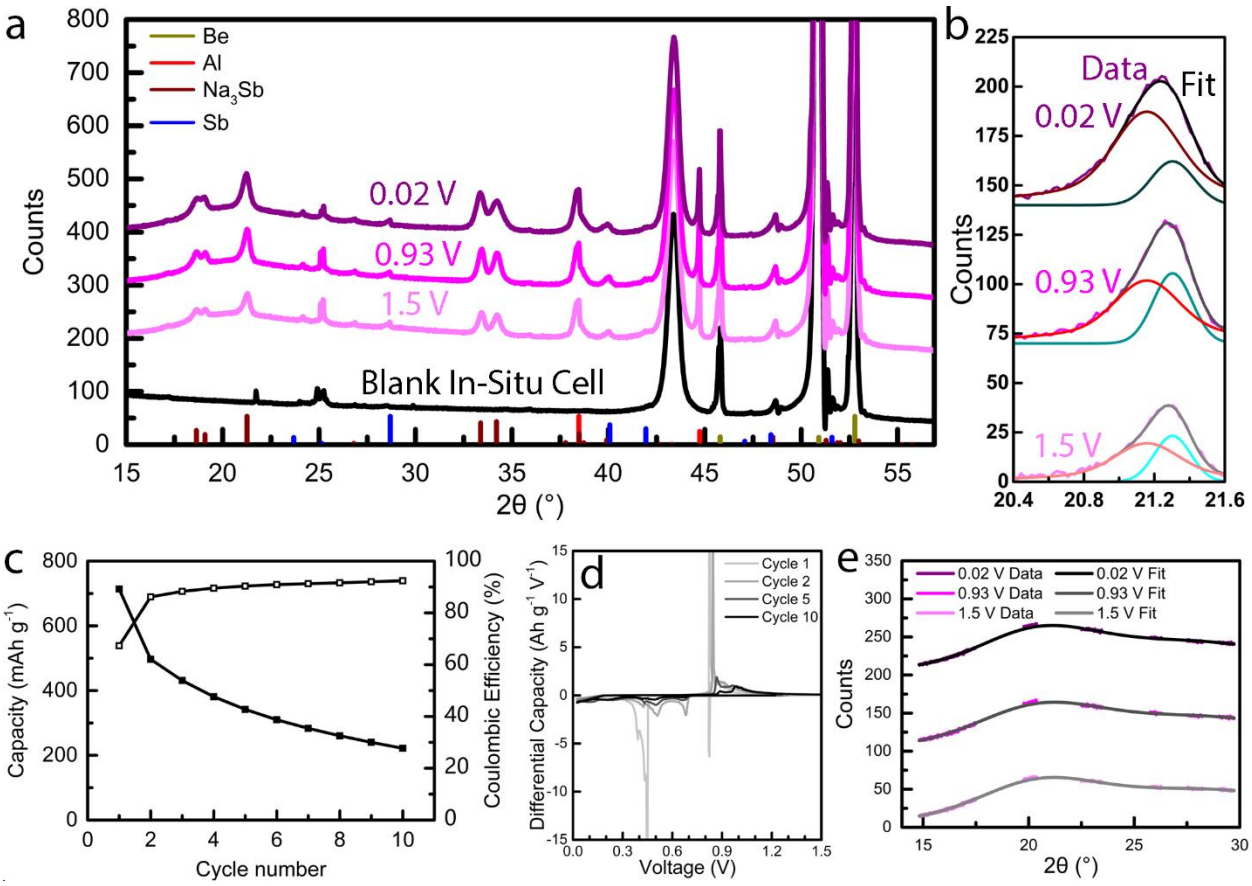

Figure 4-2. (a) Full *in situ* XRD patterns of antimony nanoplatelet electrodes (along with signal from the Al current collector and Be windows), collected after 10 aging cycles at 1C (shown in panels c and d), at desodiation potentials of 0.02 V, 0.93 V, and 1.5 V, along with (b) qualitative fits of the XRD peak at 21.3°, (c) the cycling profile of the electrode prior to *in situ* XRD measurement along with (d) the corresponding differential capacity curves ensuring predominance of the 0.97 V electrochemical cycling feature, and (e) baseline fits used for the model (Be PDF#: 01-071-0257, Al PDF#: 00-004-0787, Na_3Sb PDF#: 03-065-3523, Sb PDF#: 00-035-0732).[72,99,121,122]

A simple inspection of the observed changes in peak intensity and peak position in Figure 4-1 reveal a consistent set of trends as the electrode is desodiated. At the 0.02 V hold (following

the numerous 1C aging cycles), the electrode is in its maximally sodiated state, corresponding to a maximum in c-Na_3Sb diffraction signal (Figure 4-1, violet curve), with the peaks at 19.0° and 21.3° clearly positioned at lower 2θ angles. As the c-Na_3Sb domains are gradually desodiated during the hold at 0.93 V, the c-Na_3Sb contribution to the diffraction peaks at 19.0° and 21.3° decreases (Figure 4-1, pink curve), causing the diffraction peaks to shift toward the c-NaSb reflection positions at slightly higher angles. Finally, the hold at 1.50 V results in the desodiation of both phases (Figure 4-1, light pink curve), resulting in commensurate intensity decreases from each of the phases. Overall, these shifts suggest that a fraction of the c-NaSb desodiates during cycling. This contrasts with the observed stability of the unconvoluted (111) c-NaSb peak at 24.2°. The peak intensities of the 19.0°, 21.3° and 24.2° c-NaSb peaks are 0.8, 1 and 0.5 respectively based upon the P21/c c-NaSb (PDF#: 01-074-0801) pattern. The in-situ XRD cell set-up significantly attenuates peaks for all of the observed chemical species and so higher intensity peaks provide significantly more information. Therefore, the 19.0° and 21.3° peaks capture more information about the c-NaSb phase than the 24.2°. Thus, even though the 24.2° peak stays constant during cycling, the subtle shifts in the 19.0° and 21.3° peak maxima still suggest that a small fraction of the c-NaSb is desodiating during extended cycling.

In addition to the qualitative analysis of the observed peak shifts, we also performed a deconvolution of the peak near 21.3° 2θ, which consists of both Na_3Sb and NaSb components. After stripping kα2 radiation from the XRD data, the signal from the blank *in situ* cell was subtracted from the signal collected at the 0.02 V, 0.93 V, and 1.5 V potentials. For each of the XRD curves, a baseline was constructed using normalized Gaussian functions

$$G(2\theta) = \frac{1}{\sigma\sqrt{2\pi}} e^{-(2\theta-\mu)^2/(2\sigma^2)} \qquad 4\text{-}1$$

where σ is the root-mean-square width of the Gaussian, and μ represents the center of the Gaussian (Figure 4-2). After smooth baselines were established, Pseudo-Voigt functions were used to model the Na_3Sb (21.2634°, PDF#: 03-065-3523) and the NaSb (21.3029°, PDF#: 01-074-0801) peaks in the fitted region (Figure 4-2). The pseudo-Voigt function, $V(2\theta)$, is a weighted sum of Lorentzian and Gaussian functions, where the Lorentzian function is given by

$$L(2\theta) = \frac{1}{\pi}\frac{\frac{1}{2}\Gamma_L}{(2\theta - 2\theta_0)^2 + \left(\frac{1}{2}\Gamma_L\right)^2} \quad 4\text{-}2$$

where Γ_L is the full width at half maximum (FWHM) of the Lorentzian, $2\theta_0$ is the center of the peak, and

$$V(2\theta) = \mathrm{A}\big((1-\eta)\,G(2\theta) + \eta L(2\theta)\big) \quad 4\text{-}3$$

where A is the peak amplitude and η is a weighting factor ranging from 0 to 1 that defines the relative contributions of the Gaussian and Lorentzian functions. We note that, it is helpful to constrain η via the following equation when fitting XRD data, as it is more representative of the physical nature of the system, since Γ_L and Γ_G are rooted in physical parameters such as particle size, while η and Γ are non-physical in nature. Thus η is given by[123,124]

$$\eta = 1.36603\left(\Gamma_L/\Gamma\right) - 0.47719\left(\Gamma_L/\Gamma\right)^2 + 0.11116\left(\Gamma_L/\Gamma\right)^3 \quad 4\text{-}4$$

where Γ is the full width at half maximum for the pseudo-Voigt, which can be approximated by

$$\Gamma = 0.5346\Gamma_L + \sqrt{0.2166\Gamma_L^2 + \Gamma_G^2} \quad 4\text{-}5$$

and Γ_G is the full width at half maximum for the Gaussian, which is related to the root-mean-square width of the Gaussian as follows

$$\Gamma_G = 2\sigma\sqrt{2ln(2)} \quad 4\text{-}6$$

The fit of the peak in the region of 21.3° further validates the qualitative observations indicating the presence of crystalline NaSb and the cycling scheme proposed in Figure 4-1 and Figure 4-2.

Overall, the *in situ* XRD data strongly suggests that the desodiation peak observed in the total differential capacity plots at 0.93 V in our antimony half-cells (Figure 3-1 and Figure 3-2) can be attributed to increased desodiation from crystalline NaSb after extended cycling. In contrast to previous observations focused on early cycling, both the sharpness and the location of the peak at 0.93 V are suggestive of a well-defined two-phase transition from c-NaSb.[90] Notably, the desodiation of a-NaSb has been reported in the literature to occur at a potential of 0.88 V, directly before the observed 0.93 V desodiation peak.[16,42,91] The relative position of the observed sharp two-phase transition at a potential slightly higher than the desodiation of the amorphous phase is further suggestive that the 0.93 V peak corresponds to the desodiation of c-NaSb.[42]

To our knowledge, the impact of the suggested c-NaSb desodiation after extended cycling has not been previously discussed, likely due to the focus of previous *in situ* experiments on early cycles. However, despite the structural rearrangements necessary for the crystallization of NaSb,[38] its role would not necessarily be unexpected from a thermodynamic point of view. In addition to being the only thermodynamically stable crystalline phase between Sb and Na_3Sb,[125] on a *per sodium basis*, c-NaSb represents a global thermodynamic minimum among the stable sodium antimonide binary alloys (Table 4-1).[43] Therefore, during initial cycling, sodiation proceeds through amorphous intermediates to the fully sodiated, terminal c-Na_3Sb phase. However, as the cell degrades toward capacities commensurate with 1:1 Na:Sb (~220 mAh g^{-1}), we posit that sodiation to c-NaSb becomes favored due to the stabilization afforded by the c-NaSb phase. We also note that increased strain in the nanoplatelets may lead to a more rapid transition to c-NaSb as a dominant terminal sodiation state relative to the isotropic antimony nanocrystals. Nonetheless,

the observed two-phase desodiation reaction at 0.93 V and the associated *in situ* XRD measurements presented in Figure 4-2, combined with previous calculations in the literature, strongly suggest that crystalline NaSb plays an important, and currently underappreciated, role in the electrochemical characteristics of antimony-based alloying electrodes after extended cycling.[43]

Table 4-1. Heats of reaction (reproduced from Caputo *et al.*) for the thermodynamically stable alloys of sodium and antimony present in the binary phase diagram at room temperature[43,125]

	Sb ($R\bar{3}m$)	**NaSb ($P2_1/c$)**	**Na_3Sb ($P6_3/mmc$)**
Enthalpy of reaction (kJ/mol of Na) from elemental Na and Sb	0	-75.17	-59.69

4.4 Conclusions

The emergence of a previously unidentified desodiation reaction that appears at 0.93 V after extended cycling occurs during antimony nanomaterial cycling. *In situ* XRD measurements carried out on antimony alloying electrodes after extended cycling associate the emergence of this electrochemical feature with the presence of crystalline NaSb. We note that the micrometer-scale lateral dimensions of the nanoplatelets enable the collection of interpretable *in situ* XRD signal relative to the nanometer-scale dimensions of the nanocrystals. Overall, these observations, in conjunction with previous thermodynamic calculations in the literature, lead us to attribute this electrochemical reaction to the desodiation of crystalline NaSb – a thermodynamically favorable, but largely undiscussed source of capacity in antimony electrodes – demonstrating that crystalline NaSb plays an increasingly important role in antimony-based Na-ion battery alloying electrodes after extended cycling.

Chapter 5: Temperture-Dependent Electrochemical Characteristics of Antimony Nanocrystals

5.1 Introduction

In this chapter, we investigate the temperature-dependence of the sodiation/desodiation of antimony nanocrystal composite electrodes. Long-term cycling data illustrating the variations in capacity for an antimony nanocrystal composite electrode being cycled in a laboratory environment without temperature control, along with the corresponding ambient temperatures recorded at Seattle-Tacoma International airport, which is approximately 15 miles from the University of Washington lab where the battery was tested are pictured in Figure 5-1. Battery testing was carried out during a period where large day-night temperature swings (~20°C) occurred, which resulted in large temperature-correlated oscillations in the recorded electrode capacity. These observations demonstrate that developing a detailed understanding of the temperature-dependence of antimony nanocrystal composite electrodes is critical for their potential implementation in real-world energy-intensive, high-power applications.

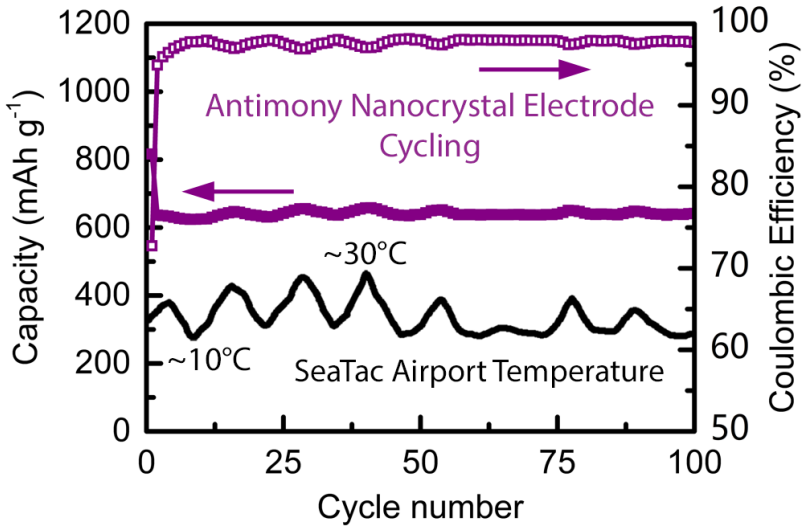

Figure 5-1. Variations in capacity and Coulombic efficiency for antimony nanocrystal conversion electrodes cycled in a lab without temperature control, correlated with the recorded temperature variations measured at Seattle Tacoma International Airport over the cycling period from May 25, 2017 through June 2, 2017.[126]

5.1.1 Mechansims leading to Temperature-Dependent Battery Performance

Temperature can strongly affect battery performance (Figure 5-1) via a variety of mechanisms, including irreversible phenomena such as metallic deposition, and reversible phenomena such as increased charge transfer resistance, increased solid-electrolyte interphase (SEI) layer resistance, or decreased liquid- or solid-state sodium diffusion rates at lower temperatures.[127–131] At low temperatures, the working ion can irreversibly deposit onto the electrode due to increased concentration polarization.[127] These metallic deposits of the working ion also increase the SEI layer thickness with each subsequent cycle, leading to increased cell resistance and lower performance. Since metallic deposition of the working ion at low temperature and the subsequent SEI layer growth that results directly from the metallic deposition are primarily

irreversible processes, these particular sources of capacity loss cannot be recovered when the electrode is returned to higher temperatures.[127]

In alloying electrodes, increased interfacial resistance leading to a reversible capacity reduction at low temperatures typically occurs in two forms: increased charge transfer resistance across the electrolyte-SEI layer interface or increased charge transfer resistance across the SEI layer-electrode interface.[130–132] In general, reversible capacity loss occurs due to increased overpotentials that stem from reversible chemical or physical traits of the battery materials. Once the operating conditions move away from the environment that caused the additional overpotential, the capacity returns. The increase in interfacial resistance at low temperature can be lessened by changing the electrolyte composition, via modifications to the solvent, ionic species, or electrolyte additives. Alterations to the electrolyte composition also change the chemical and physical properties of the SEI layer, because the SEI layer forms from electrolyte decomposition products. Therefore, these chemical and physical property changes in the electrolyte and SEI layer impact the charge transfer resistance at both the electrolyte-SEI layer interface and the SEI layer-electrode interface.

Impaired diffusion of the working ion through the liquid electrolyte can also be a potential source of capacity loss. However, electrolyte formulations have been explored extensively, and most major electrolytes have established Li-ion/Na-ion temperature operation ranges where they do not contribute to a significant loss of capacity.[129] In this study, propylene carbonate was used as the primary electrolyte solvent, as it has been demonstrated to have negligible deleterious impact on capacity at temperatures as low as 0°C.[133] Moreover, addition of fluoroethylene carbonate, an electrolyte additive used in this study, has been shown to improve cycling performance at

temperatures below 0°C.[134,135] As such, impaired diffusion of the working ion through the electrolyte is not expected to be limiting in this system.

In addition, reductions in the solid-state diffusion coefficient can also reversibly limit capacity at low temperature, making it more difficult to reach full sodiation for a given particle size.[128,131] This effect can be significant relative to changes in the other components that affect cell performance. Smaller particle sizes can be employed in order to reduce the solid-state-diffusion path length in cases where solid-state diffusion is limiting.[128] Understanding the fundamental mechanisms of capacity reduction for a given chemistry is important due to the varied strategies that can be used to mitigate the different underlying sources of capacity loss.

5.1.2 Drivers for the Temperature-Dependent Performance of Antimony Nanocrystal-based Electrodes

As discussed in detail below, differential capacity measurements and electrochemical impedance spectroscopy indicate that SEI layer-electrode charge transfer resistance is the primary driver for the ~100 mAh g^{-1} (~20%) capacity reduction as the operating temperature is reduced from 50 to 5°C for this particular antimony nanocrystal electrode architecture. The increase in SEI layer-electrode charge transfer resistance at low temperatures is shown to be primarily driven by an increased energetic barrier toward transport of the Na ions across the SEI layer-electrode interface. These results suggest that strategies targeted toward modification of the SEI layer composition could potentially lead to increased low-temperature electrode capacity for this particular class of antimony nanocrystal composite electrode.

5.2 Experimental Details

5.2.1 Materials.

N-Methyl-2-pyrrolidone (NMP) (anhydrous, 99.5%), antimony trichloride (≥99.0%), fluoroethylene carbonate (99%), propylene carbonate (99.7%), sodium metal (>99.99%, dry cubes, ACS Specification), sodium borohydride (99.99%), and sodium carboxymethyl cellulose (CMC) (M_w ~90,000), were purchased from Sigma Aldrich. Sodium perchlorate (≥98%) was purchased from Fisher Scientific. Carbon black (Vulcan XC72R) was purchased from Cabot Corporation and stored in a vacuum oven at 80°C. Copper foil (>99.99%, 9-μm thickness) was purchased from MTI Corporation. All reagents were used as received without further purification.

5.2.2 Antimony Nanocrystal Synthesis.

Antimony nanocrystals (Sb NCs) were synthesized using a modified version of the procedure by Walter *et al.* with an added methanol cleaning step, used to remove residual NaCl byproduct from the material.[17] Sodium borohydride (48 mmol) in NMP (51 mL) was heated to 60°C under nitrogen in a 250-mL three-neck flask. Antimony trichloride (12 mmol) dissolved in NMP (9 mL) was rapidly injected into the flask. The flask was immediately cooled to room temperature using an ice bath. The contents of the flask were collected and centrifuged at 7440 RCF for 4 minutes. After centrifugation, the precipitated nanocrystals were isolated by decanting the supernatant. The Sb NCs were then washed with deionized water (~30 mL) three times in a vacuum flask. The product was dried overnight under vacuum and stored in a nitrogen glovebox. If visible sodium chloride was present, the nanocrystals were further purified by suspension into 20 mL of clean methanol, followed by decantation of the supernatant after nanocrystal sedimentation. This cleaning process was repeated, as necessary, until the material was free of visible NaCl byproduct.

5.2.3 Electrode Fabrication, Coin Cell Assembly, and Electrochemical Testing.

Composite electrodes were fabricated using a 64:21:15 mass ratio of antimony:carbon-black/carboxymethylcellulose. Using standard Sb electrode fabrication procedures, the above electrode materials were formed into a slurry and mechanically mixed using a mortar and pestle.[16,17,88,89] A typical fabrication involved mixing 150 mg of antimony and 49 mg of carbon black with 0.52 mL of CMC in deionized water (0.067 g/mL), followed by dilution with an additional 0.4 mL of deionized water. Note that the amount of deionized water added was adjusted in order to achieve the visually desired slurry concentration based on ambient conditions. The slurry was then doctor-bladed onto a copper foil current collector at a thickness of 38 μm. Electrodes were cut out of the copper sheet and dried in air on a hot plate at 80°C until no visible moisture was present (typically ~5 min). The electrodes were then transferred to a vacuum oven and stored at 80°C and a pressure of less than 15 mbar until ready for punching. 15-mm-diameter electrodes were then punched out and stored in an argon glovebox for further use. CR2032-type coin cells were assembled in the argon glovebox using 1 M $NaClO_4$ in an electrolyte solution of 90% w/v propylene carbonate and 10% w/v fluoroethylene carbonate, an elemental sodium metal positive electrode, and a glass-fiber separator (Whatman, grade gf/f). Electrochemical testing was performed on the assembled coin cells, as described below. Capacities were normalized versus the weight of the active material.

5.2.4 Materials Characterization.

Transmission electron microscopy (TEM) images were captured at an accelerating voltage of 200 kV with a FEI Tecnai G2 F20 Supertwin TEM. X-ray diffraction (XRD) patterns were collected with a IμS 2-D XRD detector system on a Bruker D8 Discover diffractometer and subsequently analyzed with the EVA and Jade softwares. Scanning electron microscopy (SEM)

images were captured at 5 kV using an FEI XL830 Dual Beam FIB/SEM. Electrochemical cycling data was collected using a 64-channel MACCOR Series 4000M Automated Battery Test System along with a MACCOR temperature chamber. Electrochemical Impedance Spectroscopy (EIS) was carried out over a frequency range spanning from 0.1 Hz to 100,000 Hz using an Autolab PGSTAT128N potentiostat/galvanostat with a frequency response analyzer module (Autolab FRA32) and a MACCOR Temperature Chamber (MTC-020 Chamber). The differential capacity and EIS data were collected on the same battery. Capacity and differential capacity were collected with the cell cycled at a 1C rate throughout the temperature range. When the temperature was changed, it was adjusted at a rate of 1°C per minute between cycles. During these temperature changes the cell was rested. After differential capacity testing, EIS was then performed. Cells were charged or discharged at a C/10 rate until the desired voltage for the EIS measurement was reached, and then the cell was subjected to a constant-potential hold at that desired voltage for two hours. The cells were then subjected to an additional two-hour rest so that equilibrium at open-circuit could be achieved for the EIS measurement.

5.3 Results and Discussion

5.3.1 Antimony Nanocrystal Characterization

Antimony nanocrystals were synthesized via a modified version of the procedure developed by Walter *et al*. (Figure 5-2).[17] The macroscale product consists of aggregated nanocrystals of rhombohedral ($R\bar{3}m$) antimony (PDF #00-035-0732) with an average diameter of ~40 nm based on a Rietveld refinement of the XRD data (Figure 5-2c). Notably, while highly monodisperse antimony nanocrystal syntheses have also been developed,[16] the procedure of Walter *et al*. enables low-cost, large-scale nanocrystal production with much higher product yields.

While the resulting nanocrystal product tends to be less monodisperse and more aggregated than small-scale precision syntheses, the electrochemical cycling characteristics remain equivalent, cycling reversibly with no significant change in Na-ion battery performance for nanocrystals with diameters between 20 and 100 nm.[16,17]

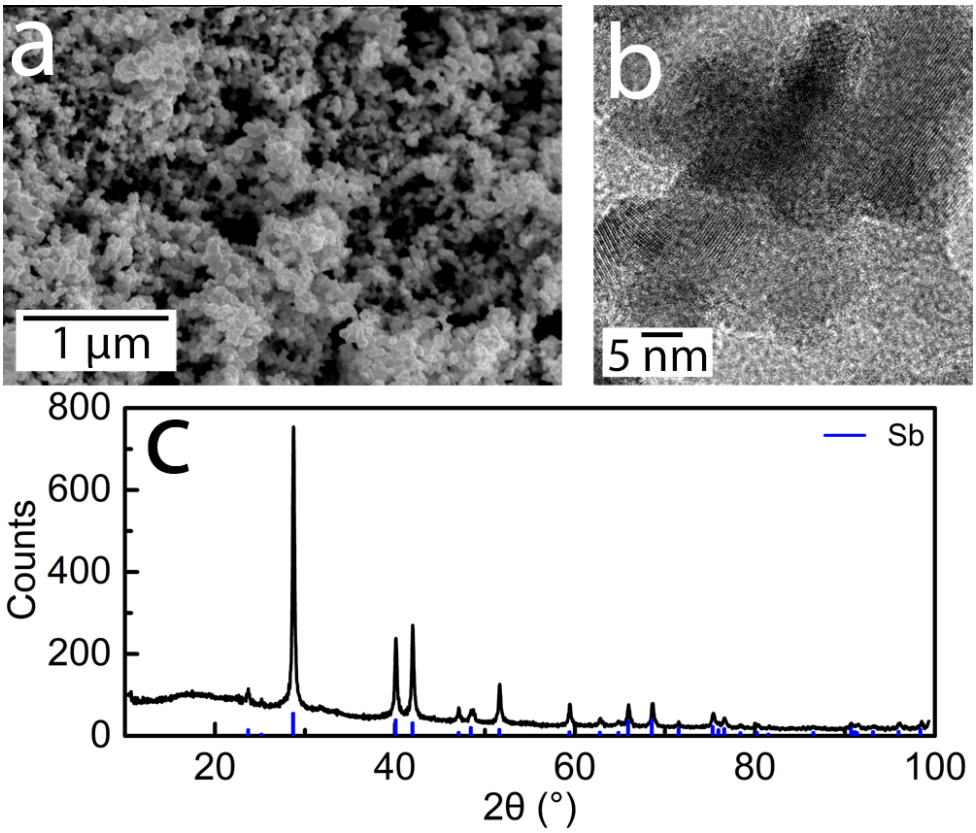

Figure 5-2. a) Scanning electron microscopy (SEM), b) transmission electron microscopy (TEM), and c) X-ray diffraction (XRD) of the as-synthesized antimony nanocrystal active material.

5.3.2 Capacity and Differential Capacity

Figure 5-3 shows temperature-dependent capacity and differential capacity data as an antimony nanocrystal composite electrode is cycled repeatedly within a voltage window of 1.5 to 0.02 V. A temperature of 50°C was chosen as the upper limit as there is known risk of battery damage and fire at temperatures above 60°C.[18] As can be seen in Figure 5-3a, the capacity of the

antimony nanocrystal electrode decreases by ~100 mAh g^{-1} (~20%) as the temperature is decreased from 50 to 5°C. Importantly, the electrode capacity consistently returns to its initial ~500 mAh g^{-1} capacity at 20°C irrespective of its temperature-dependent cycling history or whether it is returning from high or low temperature, indicating that the temperature-dependent capacity changes are primarily reversible within this set of cycling parameters. As such, primarily irreversible sources of capacity loss – such as the metallic deposition of the working ion at low temperature and the associated additional solid-electrolyte interphase (SEI) layer formation that would result directly from the metallic deposition – are not the primary cause for the changes in the capacity of the antimony nanocrystal-based composite electrodes with temperature.[127]

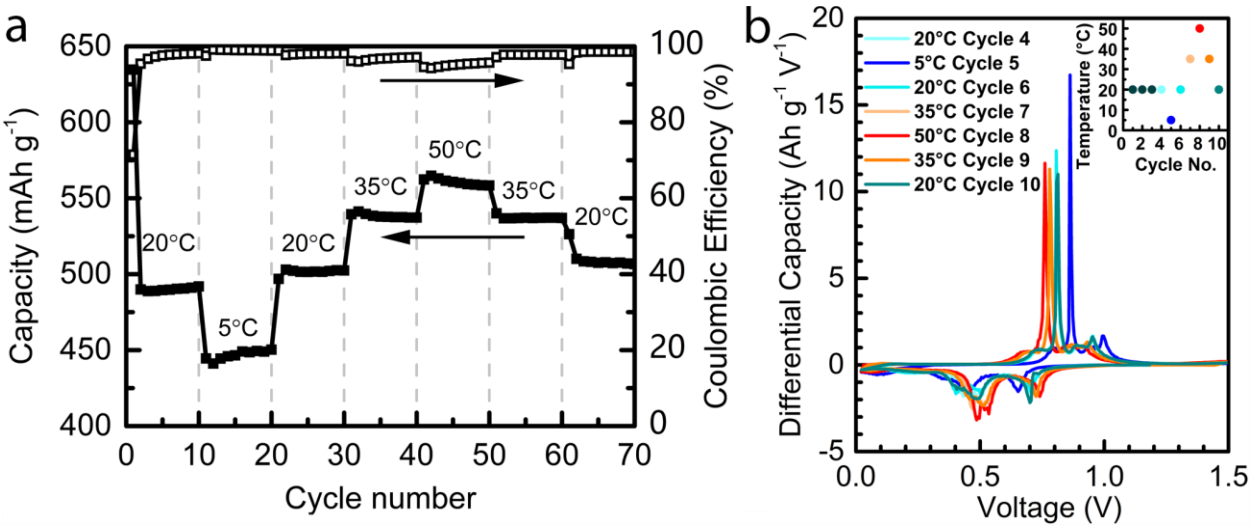

Figure 5-3. (a) Temperature-dependent gravimetric capacity and Coulombic efficiency, along with (b) temperature-dependent differential capacity plots (cycling history shown in the inset) of antimony nanocrystal-based Na-ion battery negative electrodes, cycled at a rate of 1C in 1 M $NaClO_4$ 90% propylene carbonate / 10% fluoroethylene carbonate electrolyte.

Moreover, as can be seen in the differential capacity plots shown in Figure 5-3b, a significant shift in sodiation and desodiation voltages is observed, with higher operating temperatures resulting in smaller overpotentials during both sodiation and desodiation, as would be expected. For the terminal desodiation peak, a shift of ~100 mV is observed from 0.86 V at 5°C to 0.76 V at 50°C. According to the Nernst equation

$$\Delta G^\circ = -nFE \qquad 5\text{-}1$$

where ΔG° is the Gibbs energy of an electrochemical reaction, n is the number of electrons in the reaction, F is the Faraday constant, and E is the electrochemical potential for the reaction in question, the terminal desodiation reaction, c-Na_3Sb → a-$Na_{1.7}Sb$, decreases in energy by 12.5 kJ/mol as the operating temperature is changed from 5 to 50°C, representing a 12% decrease in the energy for that reaction.[42,136] Furthermore, the voltage shifts in the peaks are reversible, again indicating that metallic deposition leading to increased SEI layer formation is not a source of capacity loss over this temperature range. In addition, the rightmost peak during desodiation, associated with the desodiation of c-NaSb, as established in Chapter 4 (~1.0 V at 5°C) also decreases in area as temperature increases.

5.3.3 Temperature-dependent SEI Layer Formation during Cycling

The antimony nanocrystal-based electrodes exhibit an increased degree of SEI layer formation as the cycling temperature is increased (Figure 5-4). The increased SEI layer formation is substantially more pronounced at 50°C than at 5 and 20°C, particularly when compared to the uncycled electrode. At high temperatures, increased SEI layer formation is favored because more thermal energy is available to drive the side reactions that result in SEI layer formation.[137] The observed build-up of the SEI layer at 50°C also indicates that SEI layer formation is more favored than the reverse SEI layer dissolution reaction, thus resulting in a lowered coulombic efficiency at

50°C, because a significant fraction of the increased SEI layer formation consists of irreversible reactions that only provide capacity during sodiation (Figure 5-4a). Nonetheless, within the parameter space investigated, this increased SEI layer formation does not outweigh the benefits to capacity of increasing temperature.

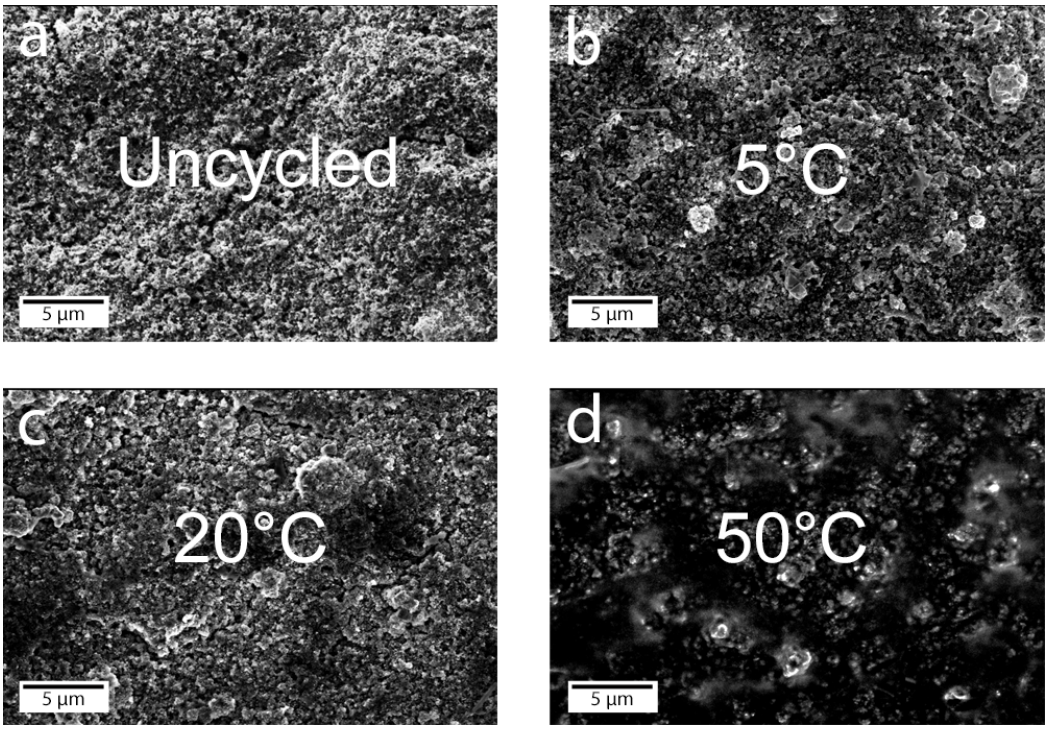

Figure 5-4. Postmortem SEM images of antimony nanocrystal-based electrodes a) before cycling, and (b-d) after cycling at b) 5°C, c) 20°C, and d) 50°C for 10 cycles at a rate of 1C.

5.3.4 Studying Temperture-Dependent Performance via Electrochemical Impedance Spectroscopy

Electrochemical impedance spectroscopy (EIS) is a powerful tool that can provide further insight into the fundamental drivers of the temperature-dependent capacity (Figure 5-3). In EIS an oscillatory current signal is applied to an electrochemical cell, and the output response is analyzed using an equivalent circuit model that can help to illuminate which specific processes in the

electrode are leading to changes in performance with temperature.[138,139] A two-electrode configuration was used for the EIS measurements in this study due to the safety risks associated with including a third reference electrode.[140] The voltages selected for EIS testing were chosen based upon the major reaction voltages for antimony sodiation and desodiation.[28,38,42,44,82]

The EIS responses were observed to vary monotonically across the voltage window at each of the tested temperatures (Figure 5-5 and Figure 5-6). Consequently, the EIS parameters for modeling the intermediate potentials fall between the parameters determined for the terminal voltages. In addition, the impedances were found to decrease at all voltages as the temperature was increased, indicating that the electrochemical processes have reduced opposition to current flow at high temperature.

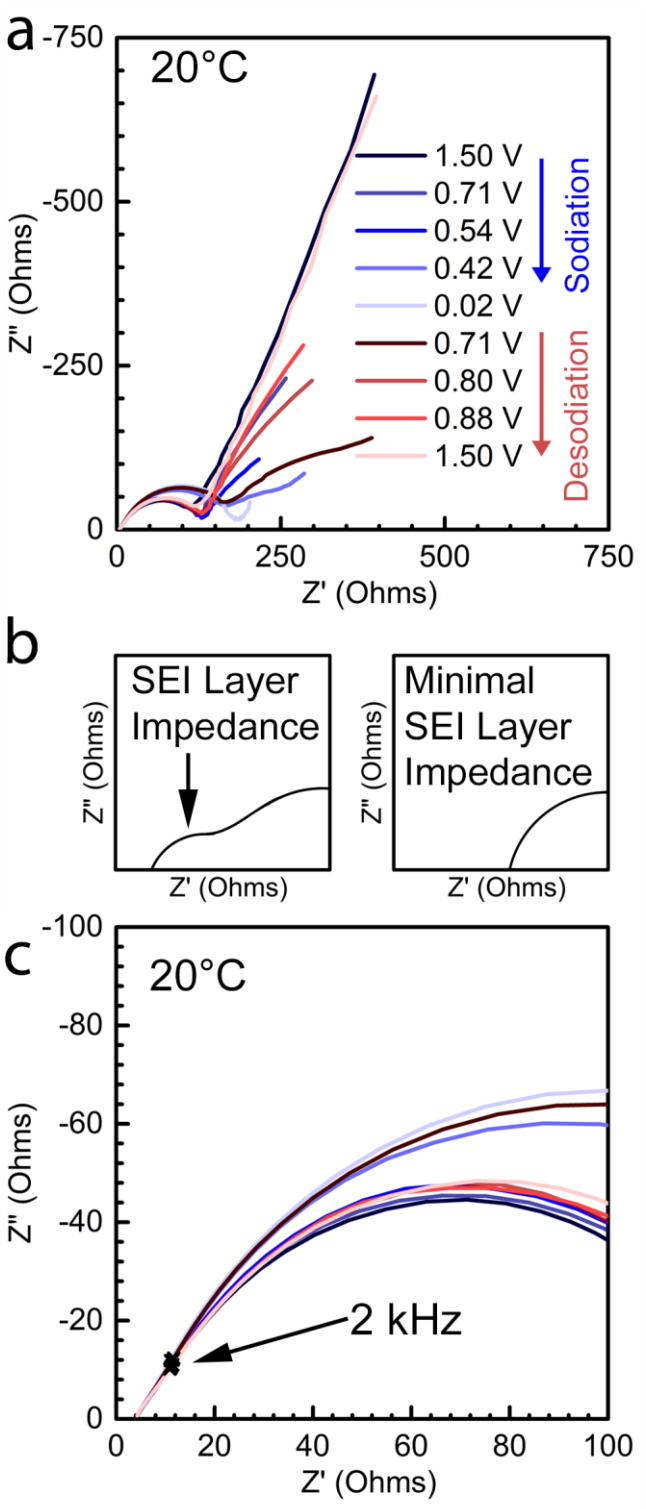

Figure 5-5. (a) Nyquist plots collected at 20°C, over a frequency range spanning from 0.1 Hz to 100,000 Hz, (b) a cartoon illustrating the characteristic impact of SEI contributions to the

impedance spectra, and (c) a magnified version of the high-frequency region for the terminal sodiation states at 0.02 V and 1.5 V, and several intermediate potentials (0.42, 0.54, and 0.71 V for sodiation and 0.71, 0.80, and 0.88 V for desodiation)

The temperature-dependent EIS data for electrodes cycled at 5, 35, and 50°C are shown in Figure 5-6 below, varying monotonically across the voltage range investigated, as seen for the room-temperature 20°C measurements (Figure 5-5).

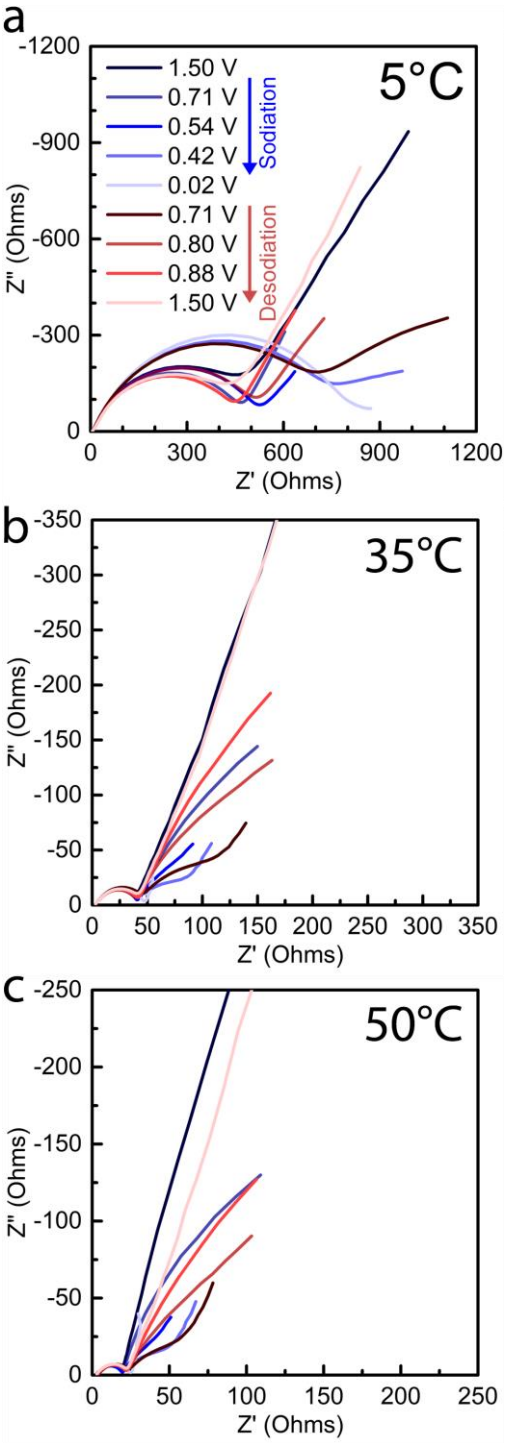

Figure 5-6. Temperature-dependent Nyquist plots collected over a frequency range spanning from 0.1 Hz to 100,000 Hz at (a) 5°C, (b) 35°C, and (c) 50°C for the terminal sodiation states at 0.02 V

and 1.5 V, and several intermediate potentials (0.42 V, 0.54 V, and 0.71 V for sodiation and 0.71 V, 0.80 V, and 0.88 V for desodiation).

The EIS data for the antimony nanocrystal electrodes shown in Figure 5-5 and Figure 5-6 can be modeled using a modified Randle's circuit (Figure 5-7), where R_{cell} is the cell resistance, R_{ct} is the charge transfer resistance, and nonidealities are accounted for by replacing both the double-layer capacitance, C_{dl}, and the Warburg element, W, with constant phase elements (CPEs). For a half-cell, if film (SEI layer) resistance is a significant component of the overall impedance, a second semicircle occurs at high frequency (in the range of 1 x 10^1 to 2 x 10^3 Hz, depending on system design and materials), and an additional RC circuit needs to be included in the model.[132,141,142] In cases for which the SEI layer is a major component of the semicircle that appears in the Nyquist plots, the semicircle tends to be relatively insensitive to voltage.[132] For the antimony nanocrystal-based electrodes, the semicircle in the Nyquist plot is dependent on voltage at all of the temperatures, with a particularly strong dependence at 5 and 20°C, providing initial indication that the SEI layer is unlikely to be a major component of the overall impedance (Figure 5-5 and Figure 5-6). Visual examination of the high frequency domain does show a slight change in slope at ~2 x 10^3 Hz that could be indicative of minor SEI layer contributions to the impedance (Figure 5-5b); however, the addition of a SEI-layer RC circuit to the Modified Randle's Circuit did not improve the model fits to any appreciable degree that would justify including it in the model.[129,130,132] Notably, the temperature-dependent EIS of symmetric Na/Na cells has been previously studied from -10 to 25°C, spanning the frequency range of our study, providing insight into how the sodium counter electrode responds with temperature.[143] In these studies, the response of the Na/Na symmetric cell did not exhibit a large Warburg tail at low frequency and exhibited a

less depressed semicircle (see discussion below) for the kinetically controlled region. This suggests that the characteristic features in our EIS data can be attributed primarily to the antimony nanocrystal-based electrode rather than the sodium electrode.

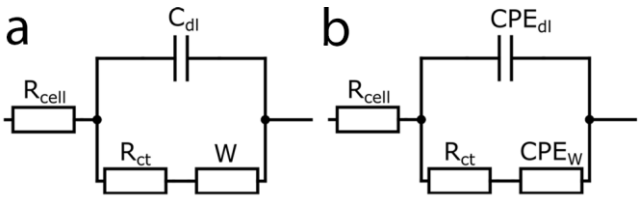

Figure 5-7. (a) Randle's Circuit and (b) the modified Randle's Circuit used to model the electrochemical cycling characteristics of antimony nanocrystal negative electrodes. Wiring diagrams were generated using Ciruit Diagram software.

As mentioned above, in our modified Randle's circuit, the double-layer capacitance, C_{dl}, is replaced with a constant phase element, CPE_{dl}, because the double-layer capacitance and charge transfer resistance cannot be fit with an ideal semi-circle in the observed Nyquist plots (Figure 5-5). The double-layer impedance, Z_{dl}, of the standard double-layer capacitance in the unmodified Randle's Circuit is represented by the following equation

$$Z_{dl} = \frac{1}{i\omega C_{dl}} \qquad 5\text{-}2$$

where ω is the angular frequency of the AC input signal and C_{dl} is the double-layer capacitance.[144] C_{dl} has a characteristic time constant associated with it, and the double-layer impedance of the CPE_{dl} component is represented by the following equation

$$Z_{dl} = \frac{1}{(i\omega)^{CPE_{dl,P}} CPE_{dl,T}} \qquad 5\text{-}3$$

where $CPE_{dl,T}$ represents the phase-angle-dependent double-layer capacitance and $CPE_{dl,P}$ modifies the phase angle.[144] When $CPE_{dl,P}$ is set to 1, Equations 5-2 and 5-3 are equivalent, with an ideal semicircle in the Nyquist plot across the frequency range. As $CPE_{dl,P}$ deviates from 1, the semicircle of the RC circuit is gradually flattened by shifting the center of the circle below the abscissa of the Nyquist plot, while maintaining the same radius from the origin, as shown by the following equation

$$\theta = \left(1 - CPE_{dl,P}\right) \times 90° \qquad 5\text{-}4$$

where θ is the angle, in degrees, at which the center of the circle shifts below the abscissa.[145] In the literature, there are a variety of proposed physical explanations for the nonideality of the semicircular component of the Nyquist plot, all relating to inhomogeneity of the electrode, where each inhomogeneous piece necessitates the inclusion of a new RC circuit.[146] Since the antimony nanocrystals used in this study have a significant size dispersion, as discussed by Walter *et al.*, this likely leads to the inhomogeneity in the electrode that in turn leads to nonidealities in the double-layer capacitance, thus requiring modification of the model with a constant phase element.[17] Importantly, despite these nonidealities, $CPE_{dl,T}$ is still associated with the time constant of the double-layer, just like C_{dl}.

In addition, the Warburg element of the Randle's circuit is also replaced with a constant phase element, denoted as CPE_W in our modified circuit (Figure 5-7), due to deviations in the angle of the tail from -45° in the observed Nyquist plots (Figure 5-5 and Figure 5-6). The Warburg element, Z_W, of the Randle's circuit is given by the following equation

$$Z_W = \frac{\sigma}{(i\omega)^{0.5}} \qquad 5\text{-}5$$

where σ is the Warburg coefficient, which can be used to determine the diffusion coefficient for the migrating species in the electrochemical cell. In an ideal Nyquist plot, this results in a straight

line at -45° for the tail.[145] However, in the observed antimony nanocrystal electrode Nyquist plots (Figure 5-5 and Figure 5-6) the angle of the Warburg impedance tail deviates significantly from the ideal -45°.

As can be seen in Figure 5-5a, the angle of the Warburg element decreases as sodiation increases. The observed variation in angle both above and below -45° in the Nyquist plots at low frequency across the voltage window are characteristic of alloying electrodes (Figure 5-5 and Figure 5-6).[147–149] However, the characteristics that lead to the changes in angle at low frequencies in the Nyquist plots are complicated and can stem from either changes in the solid-state reaction barrier or changes in the porosity of the electrode.[147,150] In alloying electrodes, the solid-state reaction and diffusion both affect impedance in the low-frequency regime, and either can be rate-limiting depending upon the particular system and testing regime. The energetic barrier of the solid-state reaction in an alloying electrode can be large since alloying reactions cause significant structural rearrangement and volume change of the electrode material.[147] In cases where the solid-state reaction barrier is dominant, the Warburg element is replaced with a reaction resistance-based CPE in series with a capacitive element that accounts for the charging ability of an electrode material, called the chemical capacitance. The reaction resistance CPE and chemical capacitance can account for the state-of-charge-based variation in the deviation from -45° in the Nyquist plots.

In cases where solid-state diffusion dominates, the state-of-charge-based variation in the deviation from -45° in the Nyquist plots can be explained by changes in the porosity of the electrodes associated with volume changes of the active material. Deviation in the angle of the Warburg element from -45° is characteristic of porous electrodes.[150] Since the Warburg element is based on one-dimensional diffusion and electrodes are three dimensional, interpreting the characteristics of the Warburg element requires significant knowledge of the electrode geometry

– including parameters such as the porosity, pore geometry, and tortuosity throughout the electrode – to accurately develop a physical model based on the parameters in the Warburg element for a given system. These parameters have not yet been studied for antimony nanocrystal electrodes. However, for the case of solid-state diffusion dominating the Warburg element, significant volume expansion at high sodiation states (~300% volume expansion for fully-sodiated antimony), leading to changes in the porosity, pore geometry, and tortuosity of the electrode, results in the observed changes in the Warburg element.[17]

The real component of the capacitance can indicate whether the chemical capacitance is a significant component of the system. In cases where the chemical capacitance is a significant contributor to the overall capacitive response of the system, the real component of the capacitance will show two plateaus when plotted versus frequency on a logarithmic scale.[148] The plateau at high frequency is indicative of the double-layer capacitance and the plateau at low frequency is indicative of the chemical capacitance. As seen in Figure 5-8, the plateau at low frequency is only observed at 35 and 50°C for the 1.5 V data and does not occur at all for the 0.02 V data. This demonstrates that, within the testing regime, the presence of the chemical capacitance is both temperature and voltage dependent. Therefore, to avoid overfitting in cases where the chemical capacitance was not a significant contributor to the EIS data, the chemical capacitance was not included in the replacement for the Warburg element. This also suggests that changes in the system parameters controlling solid-state diffusion rather than changes in the system parameters controlling the solid-state reaction barrier cause the shifts in angle for the Warburg component.

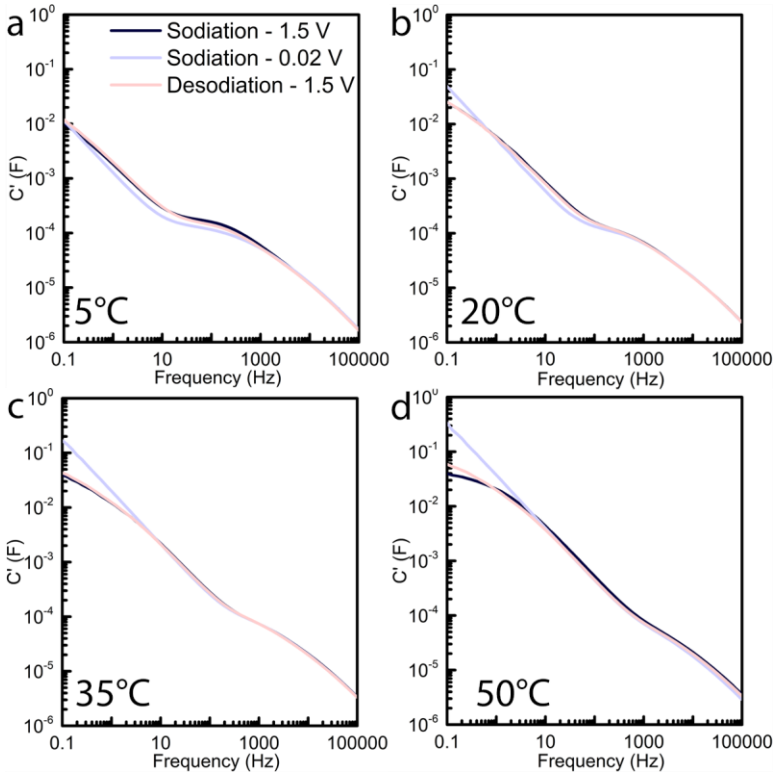

Figure 5-8. Temperature-dependent capacitance plots collected over a frequency range spanning from 0.1 Hz to 100,000 Hz at (a) 5°C, (b) 20°C, (c) 35°C, and (d) 50°C for the terminal sodiation states at 0.02 V and 1.5 V

We implemented the following generalized form of the Warburg element, which is able to capture the observed shifts in angle:[151–154]

$$Z_W = \frac{1}{(i\omega)^{CPE_{W,P}} CPE_{W,T}} \qquad 5\text{-}6$$

In the above equation, $CPE_{W,T}$ is a constant phase element for the generalized form of the Warburg element, while $CPE_{W,P}$ modifies the phase angle.

Fitting the data with the model described above can determine whether the reaction rate or solid-state diffusion is rate-limiting in the low-frequency regime. If the reaction rate is limiting, the value of $CPE_{W,P}$ would be expected to be between 0 and 0.3.[147] A value of 0 for the $CPE_{W,P}$

parameter represents ideal resistive behavior that is frequency independent. Large deviations from 0 indicate that a significant component of the CPE_W is not caused by resistive behavior, which would be uncharacteristic of the reaction resistance, but could occur if solid-state diffusion is rate-limiting and the deviation from ideal Warburg element characteristics is related to the porous electrode geometry. When $CPE_{W,P}$ is 0.5, the CPE form of the Warburg element and the standard Warburg form are equivalent, with $CPE_{W,T}$ inversely proportional to σ, as seen in the following equation.

$$Z_W = \frac{\sigma}{(i\omega)^{0.5}} = \frac{1}{(i\omega)^{0.5} CPE_{W,T}} \quad 5\text{-}7$$

If the diffusion rate is limiting, the $CPE_{W,T}$ component of CPE_W within the model correlates to the diffusion rate, with higher $CPE_{W,T}$ values indicating faster diffusion. The Warburg coefficient σ can then be used to calculate the diffusion coefficient via the following equation

$$\sigma = \frac{RT}{(nF)^2 A C_{Na,0} \sqrt{2 D_{Na,Sb}}} \quad 5\text{-}8$$

where R is the ideal gas constant, T is the absolute temperature, A is the electrochemically accessible surface area of the electrode, $C_{Na,0}$ is the initial sodium-ion concentration in the electrode, and $D_{Na,Sb}$ is the diffusion coefficient of sodium in antimony.[155] While the relationship between $CPE_{W,T}$ and $D_{Na,Sb}$ is more complicated due to the phase angle contributions, the proportionality of $D_{Na,Sb}$ and $CPE_{W,T}$ can be determined by setting $CPE_{W,T}$ to 0.5 and combining Equations 9 and 10 to get the following expression

$$\frac{\frac{RT}{(nF)^2 A C_{Na,0} \sqrt{2 D_{Na,Sb}}}}{(i\omega)^{0.5}} = \frac{1}{(i\omega)^{0.5} CPE_{W,T}} \quad 5\text{-}9$$

which simplifies to

$$\frac{1}{CPE_{W,T}} = \frac{B}{\sqrt{D_{Na,Sb}}} \quad 5\text{-}10$$

where the parameters in Equation 11 are consolidated into a single constant, B, clearly showing that

$$CPE_{W,T} \propto \sqrt{D_{Na,Sb}} \quad 5\text{-}11$$

and demonstrating that $CPE_{W,T}$ is proportional to the square root of the diffusion rate.

Finally, the expression for the impedance of the Randle's circuit is given by the following equation

$$Z = R_{cell} + \frac{Z_{dl}(R_{ct} + Z_W)}{Z_{dl} + (R_{ct} + Z_W)} \quad 5\text{-}12$$

which can be adjusted for the case of the modified Randle's circuit as follows:

$$Z = R_{cell} + \frac{\frac{1}{(i\omega)^{CPE_{dl,P}} CPE_{dl,T}} \left(R_{ct} + \frac{1}{(i\omega)^{CPE_{W,P}} CPE_{W,T}}\right)}{\frac{1}{(i\omega)^{CPE_{dl,P}} CPE_{dl,T}} + \left(R_{ct} + \frac{1}{(i\omega)^{CPE_{W,P}} CPE_{W,T}}\right)} \quad 5\text{-}13$$

The above expression for the impedance of the modified Randle's circuit (Equation 5-13) was then used to fit the EIS data collected at 1.5 V and 0.02 V, and the parameters extracted from these fits were used to evaluate the sources of performance change with temperature (Figure 5-9). The R_{cell}, R_{ct}, and $CPE_{W,T}$ parameters for the fully desodiated 1.5 V state of charge are shown in Table 5-3, as these parameters were found to exhibit the largest changes with temperature. Error bounds were determined by progressively testing values further from the fitted value for a given parameter until chi-squared decreased beyond a preset tolerance for the overall fit.[144]

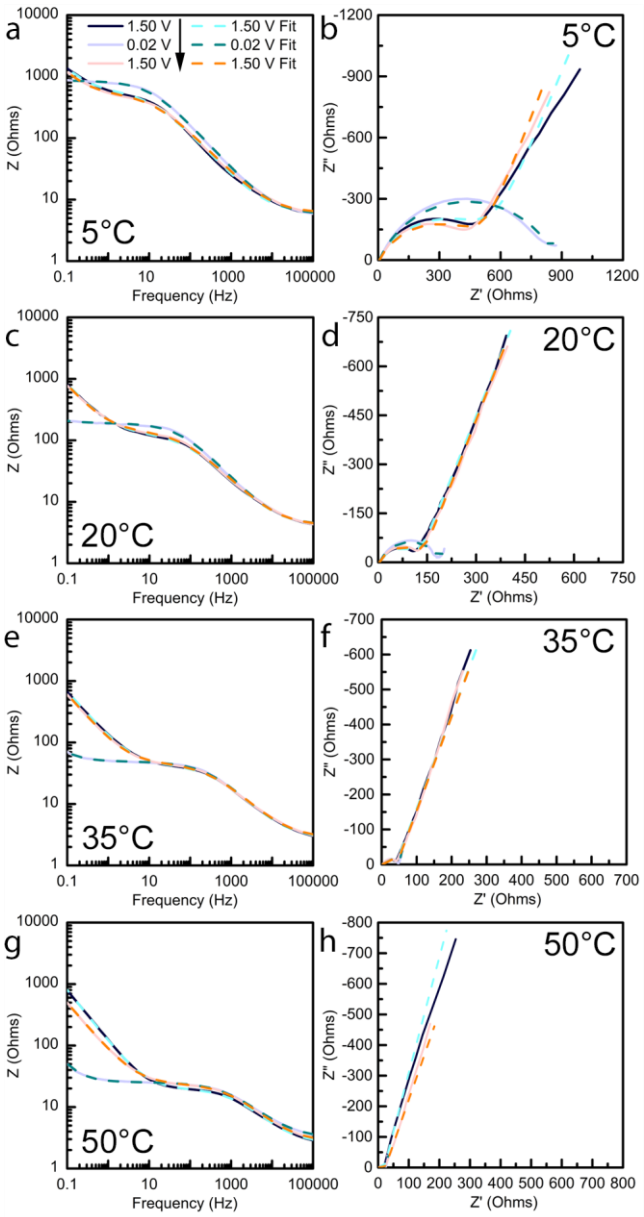

Figure 5-9. Temperature-dependent Bode and Nyquist plots collected over a frequency range spanning from 0.1 Hz to 100,000 Hz at (a, b) 5°C, (c, d) 20°C, (e, f) 35°C, and (g, h) 50°C for the terminal sodiation states at 0.02 V and 1.5 V (solid lines) along with the associated model fits (dashed lines). Note that the EIS data collected before and after each sodiation cycle (1.50 V state of charge) overlaps, indicating that the battery is cycling stably within this regime.

The R_{cell}, R_{ct}, and $CPE_{W,T}$ parameters from the EIS fits of the 1.5 V and 0.02 V spectra at 5, 20, 35, and 50°C exhibit monotonic trends with temperature, indicating that these parameters are correlated with the temperature-dependent capacity of the antimony nanocrystal composite electrodes (Figure 5-10, Table 5-1, Table 5-2, and Table 5-3). The $CPE_{dl,T}$, $CPE_{dl,P}$, and $CPE_{W,P}$ parameters do not respond monotonically with temperature at either 1.5 V and 0.02 V, indicating that these parameters do not drive the temperature-dependence of the capacity (Figure 5-10, Table 5-1, Table 5-2, and Table 5-3). The characteristics of the R_{cell}, R_{ct}, and $CPE_{W,T}$ parameters for the 1.5 V state of charge after desodiation are discussed in detail in the main manuscript. The R_{cell} and R_{ct} parameters at the 1.5 V state of charge before sodiation and at the 0.02 V state of charge after sodiation both have very similar values to the R_{cell} and R_{ct} parameters at the 1.5 V state of charge after desodiation, with the exception of the R_{ct} parameter value for the 0.02 V state of charge after sodiation at 5°C (550 Ω at the 1.5 V state of charge after desodiation *vs.* 865 Ω at the 0.02 V state of charge after sodiation). This difference indicates that charge transfer at low temperatures is more difficult at high states of charge than at low states of charge. However, as temperature is increased, this difference in charge transfer resistance at high states of charge and at low states of charge lessens. The $CPE_{W,T}$ parameter has very similar values for both the 1.5 V state of charge before sodiation and the 1.5 V state of charge after desodiation, indicating that the degradation in cell performance due to this parameter was small during EIS testing. The $CPE_{W,T}$ parameter is larger for the fully sodiated state at 0.02 V after sodiation than for the fully desodiated state at 1.5 V. The diffusion coefficient has been calculated in the literature within the region from 0.1 V to 0.7 V, and within this region, the diffusion coefficient continuously declines in value as voltage is increased.[82] Assuming that this trend continues across the voltage window, this would

match the observed changes in the $CPE_{W,T}$ parameter, given that $CPE_{W,T}$ and the diffusion constant are directly proportional.

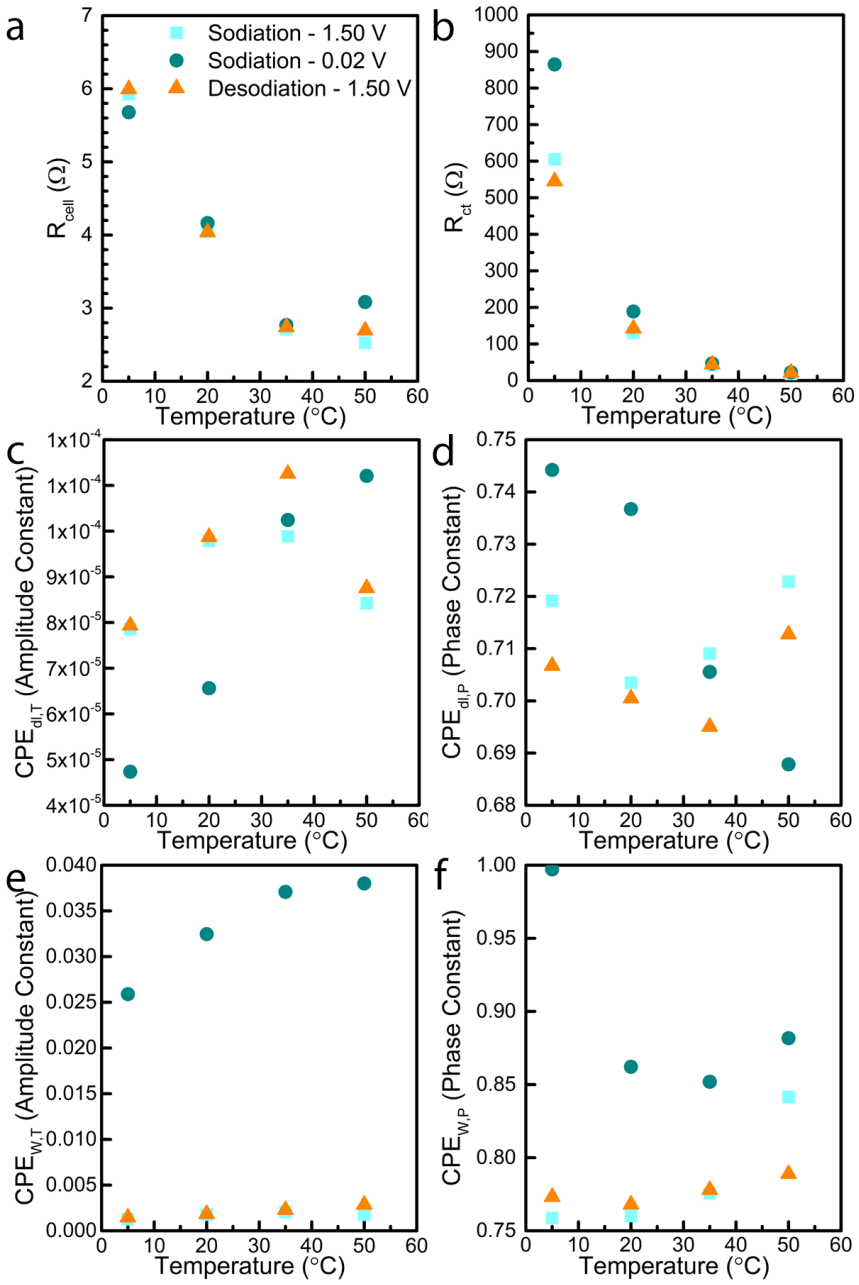

Figure 5-10. Model fit parameters as a function of temperature for (a) cell resistance, (b) charge transfer resistance, (c) amplitude constant for the constant phase element associated with the double-layer capacitance, (d) phase constant for the constant phase element associated with the

double-layer capacitance, (e) amplitude constant for the constant phase element associated with the Warburg diffusion element, and (f) phase constant for the constant phase element associated with the Warburg diffusion element.

Table 5-1. Model fit parameters and associated error bounds for a 1.5 V state of charge before sodiation.

	5°C	**20°C**	**35°C**	**50°C**
R_{cell} (Ω)	5.9 ± 0.1	4.05 ± 0.06	2.71 ± 0.03	2.53 ± 0.03
$CPE_{dl,T}$ ($s^{CPEdl,P}/\Omega$)	(7.9 ± 0.3) x 10^{-5}	(9.8 ± 0.4) x 10^{-5}	(9.9 ± 0.4) x 10^{-5}	(8.4 ± 0.4) x 10^{-5}
$CPE_{dl,P}$ (Phase Constant)	0.719 ± 0.006	0.703 ± 0.005	0.709 ± 0.005	0.723 ± 0.005
R_{ct} (Ω)	610 ± 20	130 ± 2	41.9 ± 0.4	17.9 ± 0.1
$CPE_{W,T}$ ($s^{CPEW,P}/\Omega$)	(1.25 ± 0.04) x 10^{-3}	(1.76 ± 0.02) x 10^{-3}	(2.05 ± 0.01) x 10^{-3}	(1.76 ± 0.01) x 10^{-3}
$CPE_{W,P}$ (Phase Constant)	0.76 ± 0.02	0.760 ± 0.007	0.776 ± 0.003	0.841 ± 0.002
χ^2	0.006	0.002	0.0009	0.0007

Table 5-2. Model fit parameters and associated error bounds for a 0.02 V state of charge after sodiation.

	5°C	**20°C**	**35°C**	**50°C**
R_{cell} (Ω)	5.68 ± 0.06	4.16 ± 0.05	2.77 ± 0.03	3.08 ± 0.03
$CPE_{dl,T}$ ($s^{CPEdl,P}$/Ω)	(4.74 ± 0.09) x 10^{-5}	(6.6 ± 0.2) x 10^{-5}	(1.02 ± 0.04) x 10^{-4}	(1.12 ± 0.04) x 10^{-4}
$CPE_{dl,P}$ (Phase Constant)	0.744 ± 0.002	0.736 ± 0.004	0.706 ± 0.004	0.688 ± 0.004
R_{ct} (Ω)	865 ± 7	189 ± 2	46.6 ± 0.3	22.4 ± 0.1
$CPE_{W,T}$ ($s^{CPEW,P}$/Ω)	0.026 ± 0.006	0.032 ± 0.002	0.0371 ± 0.0007	0.0380 ± 0.0003
$CPE_{W,P}$ (Phase Constant)	1.0 ± 0.2	0.86 ± 0.06	0.85 ± 0.01	0.882 ± 0.005
χ^2	0.002	0.003	0.002	0.0008

Table 5-3. Model fit parameters and associated error bounds for a 1.5 V state of charge after desodiation.

	5°C	**20°C**	**35°C**	**50°C**
R_{cell} (Ω)	6.0 ± 0.1	4.04 ± 0.06	2.74 ± 0.04	2.70 ± 0.03
$CPE_{dl,T}$ ($s^{CPEdl,P}/\Omega$)	(7.9 ± 0.3) x 10^{-5}	(9.9 ± 0.4) x 10^{-5}	(1.13 ± 0.05) x 10^{-4}	(8.8 ± 0.4) x 10^{-5}
$CPE_{dl,P}$ (Phase Constant)	0.707 ± 0.005	0.700 ± 0.005	0.695 ± 0.005	0.713 ± 0.004
R_{ct} (Ω)	550 ± 10	142 ± 2	44.3 ± 0.5	21.5 ± 0.1
$CPE_{W,T}$ ($s^{CPEW,P}/\Omega$)	(1.47 ± 0.03) x 10^{-3}	(1.85 ± 0.02) x 10^{-3}	(2.29 ± 0.02) x 10^{-3}	(2.86 ± 0.01) x 10^{-3}
$CPE_{W,P}$ (Phase Constant)	0.77 ± 0.02	0.768 ± 0.008	0.778 ± 0.004	0.789 ± 0.002
χ^2	0.004	0.002	0.001	0.0005

The cell resistance, R_{cell}, was found to decrease by approximately 50% as the temperature was increased from 5 to 50°C (Table 5-1, Table 5-2, and Table 5-3), which is a relatively small change – especially considering that the maximum cell resistance is only ~6 Ω for both 1.5 V and 0.02 V – that is orders of magnitude lower than the charge-transfer contributions. This could occur because the conductivity of the electrolyte increases with temperature, thus decreasing its resistance, and further indicates that the intrinsic resistance due to the cell and testing configuration

is not a significant factor in terms of the changes in performance with temperature, as would be expected.

In contrast, the charge transfer resistance, R_{ct}, was found to dramatically decrease to between 2.5% and 4% of its starting value at 5°C as the temperature was increased to 50°C (Table 5-1, Table 5-2, and Table 5-3). The exchange current density – which is a measure of the intrinisic ability to transfer ions from the electrolyte to the electrode, and a way to compare rates of reaction – can be calculated from the charge transfer resistance using the following equation:

$$i_0 = \frac{RT}{nFAR_{ct}} \qquad 5\text{-}14$$

Therefore, because of the change in charge transfer resistance from 5 to 50°C for a 1.5 V state of charge after desodiation, the exchange current density increases from 2.46 x 10^{-5} A/cm^2 to 7.33 x 10^{-4} A/cm^2 based upon the superficial electrode surface area of 1.8 cm^2 (Table 5-3). For comparison, the exchange current density of hydrogen evolution in 1 N H_2SO_4 is 8 x 10^{-4} A/cm^2 at a platinum electrode and 7 x 10^{-8} A/cm^2 at a titanium electrode for an electrode with the same superficial surface area at ambient temperature.[156] Both of these are catalysts for hydrogen evolution and so – at least initially – the antimony system appears to be promoting fast charge transfer across the electrode-electrolyte interface. However, since the electrode is comprised of antimony nanocrystals rather than bulk antimony, the actual electrochemically accessible surface area is potentially much larger than the superficial area, which in turn would lower the actual exchange current density. Thus, a lower bound on these exchange current densities must be established.

If one assumes that each individual antimony nanocrystal is not aggregated and has a radius of 20 nm (corresponding to the characterization data shown in Figure 5-2) then the total surface area would be 98 cm^2, resulting in exchange current densities of 4.46 x 10^{-7} A/cm^2 at 5°C and 1.32

x 10^{-5} A/cm^2 at 50°C. For comparison, graphite has an exchange current density on the order of 1 x 10^{-3} A/cm^2 in typical lithium ion batteries, which is much higher than that of the antimony nanocrystals, even at 50°C using the superficial electrode area.[157,158] Considering that one of the major advantages of antimony is its high charge-discharge capability, this is surprising, as we would expect a very high exchange current density for a material that is not rate limited. This could suggest that, in terms of rate capability, the step that includes the charge transfer resistance and exchange current density is not the rate limiting step for antimony nanocrystal alloying electrodes, and further investigation of this observation could potentially be valuable.

Increased charge transfer resistance can substantially reduce the capacity of batteries at low temperatures,[130] and there are multiple possible physical sources of changes in the charge transfer resistance, as discussed in the introduction.[159] Because the modified Randle's circuit models the data effectively without the need for an additional SEI-layer RC component, it is likely that the transport of Na-ions across the SEI layer-electrode interface is the rate-limiting step in charge transfer. Charge transfer rates can become hindered at lower temperatures, and strategies aimed at facilitating working ion transport could lead to improved antimony Na-ion capacity at low temperatures.

At 5 and 20°C, the charge transfer resistance is also strongly dependent on the state of charge, with larger radius semicircles clearly evident in the Nyquist plots at higher states of charge (Figure 5-5 and Figure 5-6). This suggests that reactions close to the terminal sodiation state are more difficult to access at 5 and 20°C, which may be due to the structural rearrangements required to reach full sodiation.[38] However, this barrier is not as significant at elevated temperatures (35 and 50°C).

The Warburg CPEs (CPE_W), deviate from the standard Warburg element angle of -45° for the tail in the Nyquist plot (Figure 5-5 and Figure 5-6) due to either reaction resistance or solid-state diffusion limitations. $CPE_{W,P}$ had values between 0.76 and 1 for all of the model fits (Figure 5-10, Table 5-1, Table 5-2, and Table 5-3), and $CPE_{W,P}$ would be expected to fall between 0 and 0.3 if the reaction rate was rate-limiting.[147] Therefore, the fitted values of $CPE_{W,P}$ suggest that solid-state diffusion is rate limiting in the antimony nanocrystal composite electrode. Thus, the variations in the angle of the Warburg element at low frequency are likely caused by the porosity of the electrode.

For a given voltage, the $CPE_{W,T}$ components for CPE_W increase by ~50-100% as the operating temperature is raised from 5 to 50°C (Figure 5-10, Table 5-1, Table 5-2, and Table 5-3). This would indicate that solid-state diffusion rates increase by ~100-200% across the temperature range, based on the proportionality demonstrated in Equation 13. Nonetheless, the change in the Warburg component is much smaller than what is observed for the charge transfer resistance; therefore, although the increase in solid-state diffusion rate at higher temperature is likely contributing to the increased capacity, it is not the majority cause. On the basis of our EIS model, the changes in antimony nanocrystal capacity with temperature appear to be strongly driven by changes in the charge transfer resistance of the interface, as illustrated schematically in Figure 5-11. The changes in the other key components of the EIS model are much smaller than the charge transfer resistance and so are likely unimpactful in terms of the observed changes in capacity.

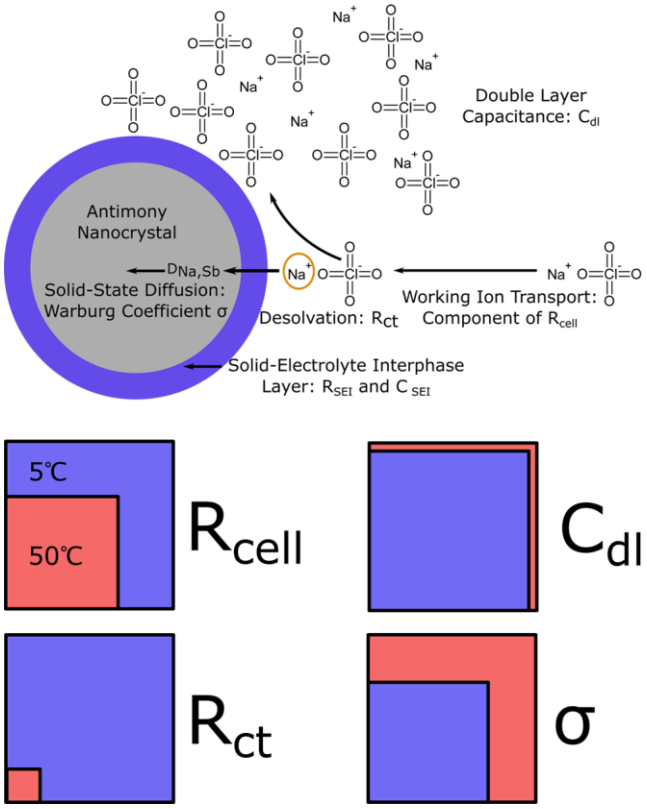

Figure 5-11. Schematic of diagram of the physical processes associated with the fitted electrochemical impedance spectroscopy model, where C_{dl} is proportional to $CPE_{dl,T}$ and σ is inversely proportional to $CPE_{W,T}$, along with the relative changes in key parameters (represented by the relative area of the blue and red squares, corresponding to experiments carried out at 5 to 50°C, respectively) extracted from EIS measurements at 1.5 V after desodiation.

5.3.5 Diffusion Coefficients for Na-Ion Diffusion in Antimony Nanocrystals

The diffusion coefficients for sodium ion diffusion through the antimony nanocrystals can be calculated from the EIS data based upon the Warburg coefficient σ using the following equation:

$$D_{Na^+} = \frac{1}{2}(V_m(dE/dx)/AF\sigma)^2 \qquad 5\text{-}15$$

where D_{Na^+} is the diffusion coefficient for Na-ions through the antimony nanocrystals, V_m is the molar volume, dE/dx is the slope of the potential versus the sodiation state, A is the surface area of the electrode, F is the Faraday constant, and σ is the Warburg coefficient.[160] We assume that $1/CPE_{W,T}$ and σ are equivalent for the purposes of the diffusion coefficient calculation, which modifies the equation as follows:

$$D_{Na^+} = \frac{1}{2}\left(V_m CPE_{W,T}(dE/dx)/AF\right)^2 \qquad 5\text{-}16$$

We calculated an upper bound for the diffusion coefficient using the superficial surface area of the current collector (1.77 cm^2) and a lower bound for the diffusion coefficient based upon the surface area of completely unaggregated spherical nanocrystals with a 40-nm diameter (98 cm^2). (Table 5-4). At 1.5 V, we used the Sb molar volume (18.18 cm^3/mol) and at 0.02 V we used the Na_3Sb molar volume (71.44 cm^3/mol).[17,66,161] In addition, we multiplied the surface areas by a factor of 3.9 for the diffusion coefficient calculations at 0.02 V to account for the additional surface area of Na_3Sb relative to Sb.[17] Previously, sodium diffusion coefficients have primarily been determined for desodiation close to the Na_3Sb terminal sodiation state at room temperature with values ranging from ~10^{-13} cm^2 s^{-1} to ~10^{-9} cm^2 s^{-1}.[82,162,163] The most relevant study, based upon the voltage window tested, was conducted between 0.1 V and 0.7 V for an antimony thin-film using a potentiostatic intermittent titration technique (PITT).[82] At 0.1 V (the closest reference point to our data) the diffusion coefficient was on the order of 10^{-9} cm^2 s^{-1}. For 20°C at 0.02 V, we found a lower bound on the order of 10^{-7} cm^2 s^{-1}. However, PITT and EIS are known to provide quantitatively different results, particularly for phase-change electrodes that can lead to measured diffusion coefficients that are greater than two orders of magnitude apart.[164–168] Thus, our diffusion coefficients are comparable to those previously observed for antimony. Furthermore, based upon our data, the sodium diffusion coefficients in antimony are approximately two to three orders of

magnitude lower than the sodium diffusion coefficients in Na_3Sb, which aligns well with the previous diffusion coefficient measurements using PITT, which showed a decrease in the diffusion coefficient of approximately one order of magnitude between 0.1 and 0.7 V.[82] The diffusion coefficients do not vary strongly with temperature, and so are not the major driver for the temperature-based performance changes.

Table 5-4. Diffusion coefficients based on the EIS Warburg component.

	Surface Area	5°C	20°C	35°C	50°C
D_{Na+} (cm^2 s^{-1}) 0.02 V After Sodiation	Maximum	2 x 10^{-7}	3 x 10^{-7}	4 x 10^{-7}	2 x 10^{-7}
	Minimum	1 x 10^{-5}	2 x 10^{-5}	2 x 10^{-5}	1 x 10^{-5}
D_{Na+} (cm^2 s^{-1}) 1.5 V After Desodiation	Maximum	3 x 10^{-10}	5 x 10^{-10}	5 x 10^{-10}	6 x 10^{-10}
	Minimum	2 x 10^{-8}	3 x 10^{-8}	3 x 10^{-8}	3 x 10^{-8}

5.4 Conclusions

Using electrochemical impedance spectroscopy and differential capacity measurements, we demonstrate that charge transfer resistance is the main source of capacity reduction (~100 mAh g^{-1}, ~20%) for antimony nanocrystal composite electrodes as the cycling temperature is decreased from 50 to 5°C. The increase in charge transfer resistance with reduced temperatures is primarily driven by the increased difficulty of Na-ion transport across the SEI layer-electrode interface. As the cycling characteristics of the antimony nanocrystal composite electrodes are highly reversible, we find that primarily irreversible sources of capacity loss, such as sodium deposition and subsequent SEI layer formation, are not major sources of the capacity reduction with reduced temperature under the investigated conditions. Furthermore, we show negligible contributions to

the capacity reduction at low temperatures from the double layer capacitance, resistive and capacitive contributions from charge transfer or ion mobility through the solid-electrolyte interphase (SEI) layer, and the rate of solid-state diffusion in the antimony nanocrystals. Overall, these results suggest that rational modification of the SEI layer composition could potentially increase the low-temperature capacity of antimony nanocrystal composite electrodes.

Chapter 6: Effects of Oxide Formation on the Electrochemical Cycling Characteristics of Antimony Nanocrystal Alloying Electrodes

6.1 Introduction

Antimony (Sb) and its oxide, senarmontite (Sb_2O_3), have both been investigated as alloying electrode materials that exhibit large theoretical gravimetric capacities (660 mAh g^{-1} and 1103 mAh g^{-1} respectively) and impressive rate capabilities, with antimony nanocrystal-based Na-ion battery electrodes experiencing only a ~15% reduction in capacity at a 20C rate, relative to a 1C rate.[17,169] Surprisingly, despite the propensity of antimony toward oxide formation, nanostructured antimony active materials are typically processed in water-based slurries under atmospheric conditions during battery electrode fabrication.[16,17,63,170] Although this fabrication method is lower cost and much safer than the approaches for other battery materials, which commonly require processing under inert gas using toxic organic solvents, oxidation of the active material during electrode fabrication is an uncontrolled variable that has not been discussed in detail. Interestingly, while a number of studies have fabricated electrodes based on composites of antimony and antimony oxide (typically Sb_2O_3), showing capacities above the theoretical capacity of antimony with good rate capabilities in Na-ion batteries,[169,171–175] these studies have primarily focused on one or two specific levels of oxidation, rather than a systematic investigation into the impact of Sb_2O_3 content on the cycling characteristics of nanostructured Sb/Sb_2O_3 electrodes.

Herein, we systematically probe the changes in the electrochemical cycling characteristics of antimony nanocrystal-based Na-ion battery electrodes as a function of active material oxidation. We find that large levels of oxide formation adversely affects rate capability, but find further mechanistic support that capacity retention is indeed increased with low levels of oxidation,[169] largely due to increased amorphization and inhibition of the crystalline sodium antimonide (c-

Na_3Sb) terminal sodiation state. Barriers to sodiation during initial cycling are alleviated by the eventual amorphization of the c-Sb_2O_3, indicating that a burn-in period is required for antimony electrodes with a significant oxide fraction. Furthermore, we find the desodiation of the oxide is kinetically limited, leading to substantial sodium sequestration in the oxide and low reversible sodium storage utilization during cycling. Likewise, desodiation of the antimonide becomes kinetically limited after ~200 cycles. Overall, we develop significant insight into the kinetic and thermodynamic considerations associated with the electrochemical sodiation of nanostructured Sb/Sb_2O_3 as a function of oxide content, which we hope will inform future work related to the optimization of antimony-based alloying electrodes.

6.2 Experimental Methods

6.2.1 Materials.

N-Methyl-2-pyrrolidone (NMP) (anhydrous, 99.5%), antimony trichloride (≥99.0%), methanol (anhydrous, 99.8%), propylene carbonate (99.7%), sodium metal (>99.99%), sodium borohydride (99.99%), and sodium carboxymethyl cellulose (CMC, M_w ~90,000) were purchased from Sigma Aldrich. Sodium perchlorate (≥98%) was purchased from Fisher Scientific. Fluoroethylene carbonate (≥98%) was purchased from TCI America. Carbon black was purchased from Cabot Corporation (Vulcan XC72R) and stored in a vacuum oven at 80°C. Copper foil was purchased from MTI Corporation. All reagents were used as received without further purification.

6.2.2 Antimony Nanocrystal Synthesis.

Antimony nanocrystals were synthesized based on the procedure of Walter *et al.*[17] Briefly, sodium borohydride (48 mmol) was dissolved in NMP (51 mL) in a three-neck flask and heated to 60°C under nitrogen atmosphere. $SbCl_3$ (12 mmol) was dissolved in NMP (9 mL) and rapidly

injected into the flask. The flask was then rapidly cooled to room temperature using an ice bath. The product was centrifuged at 7440 RCF for 4 minutes, after which the supernatant was removed and the antimony nanocrystals (NCs) were collected. The Sb NCs were then washed with deionized water (~30 mL) three times using a filter funnel connected to a vacuum flask. The product was dried overnight under vacuum (<4 x 10^{-5} bar) and stored under nitrogen. An additional methanol cleaning step was employed as needed to remove excess NaCl byproduct.

During nanocrystal synthesis, the antimony trichloride precursor ($SbCl_3$) is reduced by sodium borohydride ($NaBH_4$) to form antimony nanocrystals (Sb NCs)[17] along with a significant quantity of residual sodium chloride byproduct. In a typical synthesis, the byproducts are easily removed by rinsing the product with deionized water, as described in the methods section of the main text. However, in cases where visible quantities of sodium chloride salt are still present on the surface of the nanocrystals after cleaning, or in cases where air exposure and adventitious oxidation needs to be prevented, the residual salt can be removed under an inert, moisture-free atmosphere by suspending the nanocrystal product (~600 mg) in 20 mL of anhydrous methanol, decanting the methanol after the antimony nanocrystals settle out of dispersion, and repeating as necessary.

6.2.3 Antimony Nanocrystal Oxidation.

In a typical experiment, antimony nanocrystals (~150 mg) were dispersed via vortexing in deionized water (3 mL). The dispersion was then placed in a vial on a hot plate at 95°C and stirred for up to 240 minutes until the desired level of oxidation was achieved.[176] When extended periods of oxidation were employed, the vial was covered with a glass fiber filter in order to mitigate potential outgassing of sublimated antimony oxide.[177]

6.2.4 Electrode Fabrication, Cell Assembly and Testing.

In a typical electrode fabrication, active material, conductive carbon, and polymeric binder were combined via mortar and pestle mixing with a mass ratio of 64:21:15 [(Sb/Sb_2O_3):carbon black:CMC] and then slurry-cast using a doctorblade.[16,17,88,89] A typical electrode formulation used 150 mg antimony, 49 mg carbon black, and 0.52 mL CMC in deionized water (0.067 g/mL), along with an additional ~0.4 mL of deionized water, which was adjusted as needed to create the desired slurry concentration. After mortar-and-pestle mixing, the slurry was then doctor-bladed onto a copper foil current collector and dried on a hot plate at 80°C. Electrodes were stored in a vacuum oven (80°C, less than 15 mbar) until use, at which point they were weighed in air, under ambient conditions. 15-mm diameter electrodes were then punched out, weighed, and transferred to an argon glovebox along with the excess electrode material. CR2032-type half cells were assembled in an argon glovebox using elemental sodium as the positive electrode, a glass fiber separator (Whatman, grade gf/f), and 1.0 M $NaClO_4$ in 90% w/v propylene carbonate and 10% w/v fluoroethylene carbonate electrolyte. Electrochemical testing was performed with a MACCOR Series 4000M 64-Channel Automated Battery Test System using a 1C cycling rate that corresponds to a current density of 660 mA/g. Gravimetric capacities were calculated based on the weight of the active material. To verify the resultant composition of the active material after the additional air exposure that occurred during fabrication and weighing, the excess electrode material was then characterized using X-ray diffraction (XRD) and subsequent Rietveld refinement.[72,79,121,178]

6.2.5 Galvanostatic Intermittent Titration Technique (GITT) Experiments

GITT data was also collected using the MACCOR Series 4000M 64-Channel Automated Battery Test System. During GITT cycles, current was injected or extracted via a C/10 current

pulse (66 mA/g) over the course of 1 minute, with a 10-minute rest period between pulses to monitor the voltage response of the cell to each current injection / extraction event. This process was carried out repeatedly as the cell was discharged to 0.02 V and then charged to 1.5 V. In between GITT experiments, the cell was cycled repeatedly at a rate of 1C (660 mA/g) in order to investigate the kinetics of charge injection / extraction across a wide span of extended cycling.

6.2.6 Materials Characterization

Scanning electron microscopy (SEM) images were collected with a FEI XL830 Dual Beam FIB/SEM operating at 5 kV. XRD scans were collected on a Bruker D8 Discover diffractometer with a IμS 2-D XRD system and then analyzed using EVA software. The composition of the samples was determined using the Whole Pattern Fitting component of the Jade software package.

6.2.7 Rietveld Refinements

Crystallite size and sample composition can be determined from X-ray diffraction data using Rietveld refinement and the Whole Pattern Fitting module in the Jade software package.[178] An example of the Rietveld refinement analysis that was carried out is shown in Figure 6-1 below. The full data set with oxidation parameters is shown in Table 6-1.

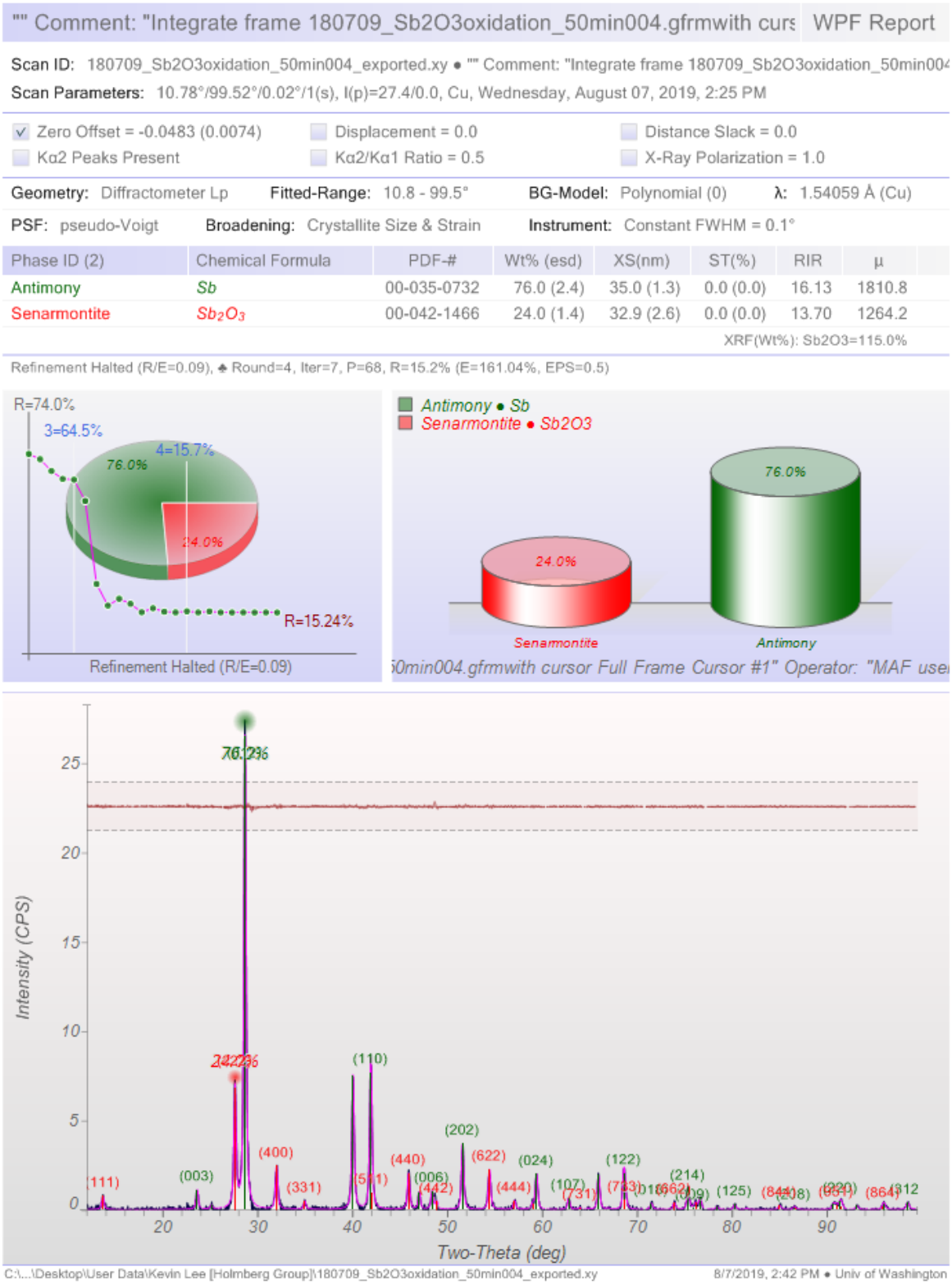

Figure 6-1. Rietveld refinement and Whole Pattern Fitting for a 50-minute oxidation carried out in 6 mL of deionized water.

Table 6-1. Degree of oxidation and crystallite sizes based on Whole Pattern Fitting and Rietveld refinement of the studied samples.

Oxidation (mol% Sb_2O_3)	Sb Crystallite Size (nm)	Sb_2O_3 Crystallite Size	Electrode	Figures and Tables	Time (hrs)	DI H_2O Volume (ml)	Dispersal Method	Vial Cover
0	24 ± 2	NA	Yes	Figures 6-2, 6-4, 6-5 and 6-6 – 0%	0	NA	NA	NA
18 ± 2	-	-	Yes	Figures 6-4, 6-5 and 6-6 – 20%	0	NA	NA	NA
43 ± 7	-	-	Yes	Figure 6-4 and 6-5 – 45%	0.5	6	Vortexing	No
44 ± 3	-	-	Yes	Figure 6-5 and 6-6 – 45%	0.5	6	Vortexing	No
58 ± 4	-	-	Yes	Figures 6-5, 6-5 and 6-6 – 60%	1	6	Vortexing	No
89 ± 7	-	-	Yes	Figures 6-5, 6-5 and 6-6 – 90%	1	6	Vortexing	No
100	NA	33 ± 2	Yes	Figures 6-2, 6-4, 6-5, 6-6, 6-7, 6-8, 6-9, 6-10, and 6-11 – 100%	4	3	Vortexing	Glass Fiber Filter
24 ± 1	-	-	No	Figure 6-3	1	3	Vortexing	No
100	-	-	No	Figure 6-3	1	3	Sonication	No
16 ± 1	-	-	No	Table 6-3	1	6	Vortexing	No
32 ± 1	-	-	No	Table 6-3	0.833	1	Vortexing	No
67 ± 3	-	-	No	Table 6-3	2	3	Vortexing	No

6.2.8 Sb/Sb_2O_3 Nanocrystal Capacity Error

Accurately determining the margin of error for the measured electrode gravimetric capacities is critical to determining the degree to which the increased theoretical capacity of Sb_2O_3 (1103 mAh g^{-1}) relative to Sb (660 mAh g^{-1}) can be realized.[17,169] There are a number of possible sources of capacity error, including inhomogeneous distribution of the active material in the electrode, weighing uncertainty based on balance accuracy, and weighing errors caused by

differences between the actual copper current collector weight and the average copper current collector weight. Careful weighing of the electrode materials in large quantities, use of precise balances, and full mixing of the electrode slurry can largely eliminate the first two sources of capacity error. However, error due to the difference between the actual copper current collector weight and the average copper current collector weight is difficult to eliminate.

The error due to the difference between the actual copper current collector weight and the average copper current collector weight occurs because of the predominant electrode weight determination procedure that is used throughout the literature. The weights of the electrode material and the copper current collector in the electrode/current collector assembly cannot be individually measured, since the electrode/copper current collectors are punched out *after* the electrode slurry is doctor bladed onto a large-area copper foil. Consequently, the weight of the electrode material is determined by subtracting the *average* weight of a copper current collector disk for a given punch size from the actual weight of the punched-out electrode/current collector assembly. Unfortunately, the rolled copper foil used for electrode fabrication has non-negligible thickness variations, which introduces significant error into this electrode weight determination technique, and subsequent calculated gravimetric capacities. The only way to reduce the influence of this error for a given copper foil is to increase the electrode thickness; however, for most electrode architectures, increasing the electrode mass loading adversely affects performance because the electrolyte does not fully penetrate the porous electrode structure beyond a certain thickness, and the electron transport pathways to the current collector become impeded.

For slurry-cast antimony nanocrystal electrodes, optimal electrode performance was seen with a 38-μm doctor-blading thickness, corresponding to a mass loading of ~1 to 1.2 mg of active electrode material per 15-mm-diameter disk. The manufacturer specifications indicate that the

MTI copper foil current collector is 10.5 ± 1.5 μm thick,[179] which is similar to the specifications given by other manufacturers for this thickness of copper foil.[180,181] For a 15-mm-diameter current collector, with a copper density of 8.94 g cm^{-3}, the weight of the current collector is 16 ± 3 mg based on the thickness tolerance information provided by the manufacturer.[179] A copper disk weight variation of 3 mg would make accurate gravimetric capacity determination difficult for active material mass loadings on the order of 1 mg. However, measurements of the foil indicate that the actual weight variation is much smaller than the values reported by the manufacturer (Table 6-2). Based on the measured standard deviation for the mass of a 15-mm-diameter copper current collector and the typical active material mass loadings of ~1 to 1.2 mg used in the study, the gravimetric capacity uncertainty in our measurements is approximately ±10%. If the mass loading of the electrode decreases, the margin of error can increase significantly. Since the theoretical capacity of Sb_2O_3 is 67% larger than the theoretical capacity of Sb, a 10% margin of error should be sufficient for determining the degree to which Sb_2O_3 improves capacity relative to unoxidized Sb.

Table 6-2. Average clean copper foil current collector mass (with no electrode composite) for 25 copper disks, each weighed 5 times, and repeated for each diameter shown below.

Diameter (mm)	Average (mg)	StDev (mg)	Ratio
15	16.157	0.140	0.009
16	18.366	0.229	0.012
19	27.296	0.842	0.031

6.3 Results and Discussion

6.3.1 Antimony Nanocrystal Oxidation

We demonstrate that antimony nanocrystals can be controllably oxidized up to 100 mol% Sb_2O_3 in deionized water at 95°C, with minimal aggregation (Figure 6-2). Rietveld refinement indicates that the antimony nanocrystals in the as-synthesized unoxidized antimony nanocrystal-based electrode have a diameter of 24 ± 2 nm, which corresponds well with the reported literature value of 22 nm for this particular protocol (Figure 6-2, Table 6-2).[17] Likewise, for the fully oxidized Sb_2O_3 electrode material, Rietveld refinement indicates that the Sb_2O_3 nanocrystals have a diameter of 33 ± 2 nm, both well within the reported 100-nm diameter size range for stable cycling of nanocrystalline antimony.[16,17]

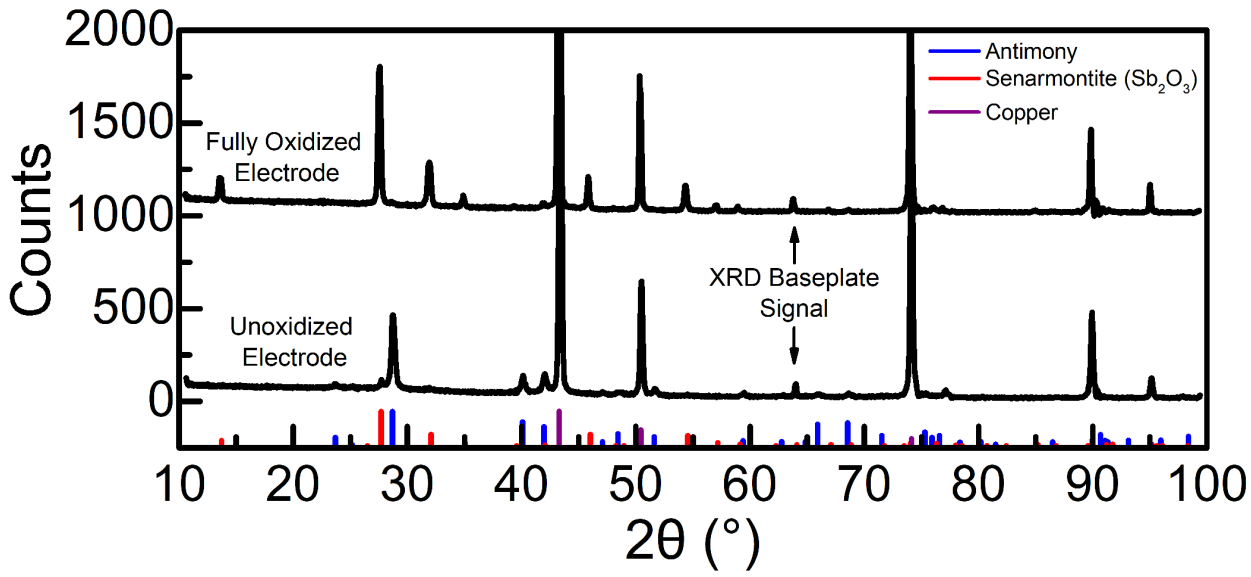

Figure 6-2. X-ray diffraction (XRD) patterns of unoxidized (0 mol% Sb_2O_3) and fully oxidized (100 mol% Sb_2O_3) antimony electrodes (PDF #s: Sb: 00-035-0732, Sb_2O_3: 00-042-1466, Cu: 00-004-0836).[72,79,121]

The oxidation rate of the antimony nanocrystals was found to be highly dependent upon the degree of nanocrystal aggregation, the method used to disperse the nanocrystals prior to oxidation, the nanocrystal concentration, and the amount of air exposure prior to oxidation. These factors, particularly aggregation and air exposure time before oxidation, can be affected by the synthesis and oxidation parameters, including precursor age, the preparation methods used before oxidation, and product handling. In addition, it is important to note that sublimation of oxidized antimony can lead to material loss during extended oxidation procedures. When the above variables are well controlled, repeatable levels of oxidation can be achieved.

The observed differences in oxidation rate, depending upon the method that was used to disperse the antimony nanocrystals in deionized water prior to oxidation, provide a clear illustration of how aggregation strongly affects active material oxidation. For example, when the antimony nanocrystals were dispersed via vortexing, as opposed to sonication, the oxidation rate was observed to be significantly lower (Figure 6-3). While antimony nanocrystals dispersed via sonication were fully oxidized to 100 mol% Sb_2O_3 after 1 hour in deionized water at 95°C, when the nanocrystals were dispersed via vortexing, only 24 ± 1 mol% Sb_2O_3 was achieved after 1 hour at 95°C. In general, sonication is significantly more effective at dispersing aggregated material than vortexing,[182] leading to a more complete dispersion with less aggregated material that is more readily oxidized, clearly demonstrating the importance of dispersion method on nanocrystal oxidation rate.

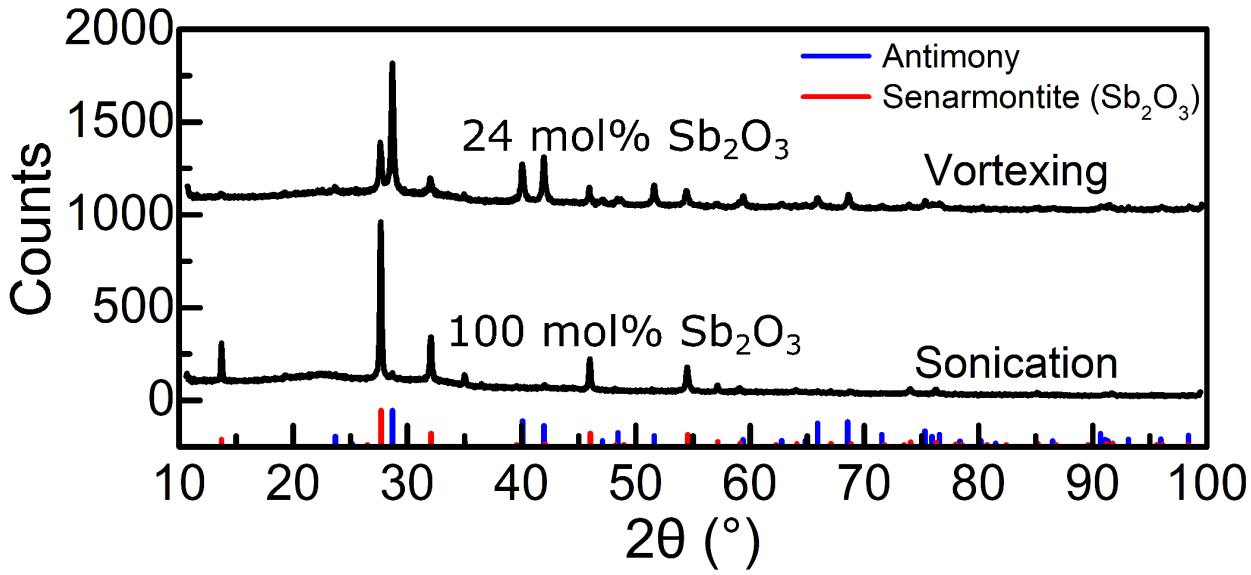

Figure 6-3. XRD of antimony nanocrystals oxidized for 1 hour at 95°C after either sonication for 10 minutes or vortexing for 1 minute in 3 mL of deionized water. (PDF #s: Sb: 00-035-0732, Sb_2O_3: 00-042-1466).[72,121]

The mass of antimony recovered from each aqueous oxidation dispersion dropped substantially as oxidation proceeded (Table 6-3). Past literature on the oxidation of antimony has shown that for oxidation beyond Sb_2O_3, oxidation and sublimation become competing processes with similar activation energies ($E_a^{(ox)}$ = 192 kJ/mol and $E_a^{(sub)}$ = 185–198 kJ/mol, respectively).[177,183] In cases where the sublimation rate is comparable or greater than the oxidation rate, mass loss occurs.[184,185] Notably, recoverable mass can be dramatically increased by placing a glass fiber filter over the top of the vial during oxidation, allowing free flow of oxygen in and out of the vial, but increasing the vapor pressure in the vial headspace, thus suppressing Sb_2O_3 sublimation. To reiterate, careful control of all synthesis, oxidation, and electrode fabrication parameters is critical to ensuring repeatable levels of oxidation.

Table 6-3. Recoverable antimony weight for different levels of oxidation.

Initial Weight (mg)	28 mol% Sb_2O_3 Weight (mg)	32 mol% Sb_2O_3 Weight (mg)	67 mol% Sb_2O_3 Weight (mg)
150	100	100	20

6.3.2 Electrochemical Sodiation/Desodiation of Sb/Sb_2O_3 nanocrystals

Figure 6-4 shows the measured gravimetric capacity, coulombic efficiency, and rate capability of Na-ion battery negative electrodes fabricated using antimony nanocrystals that had been subjected to various degrees of oxide formation, ranging from completely unoxidized Sb to fully oxidized senarmontite (Sb_2O_3). As can be seen in Figure 6-4a, although small amounts of oxidation appear to give rise to a slightly increased gravimetric capacity – as has been observed previously[169,171–173] – and larger amounts of oxidation result in a burn-in period where capacity increases during initial cycling, the resultant cycling capacity of the oxidized antimony nanocrystal electrodes remain largely unchanged, irrespective of oxidation level, despite the fact that the theoretical gravimetric capacity of senarmontite (1103 mAh g^{-1}) is approximately double that of pure antimony.[16,169] Notably, the standard water-based electrode slurry processing protocols used widely throughout the literature[16,17,63,170] consistently gave rise to samples with a final oxide content of up to 20%. Electrodes comprised of fully oxidized Sb_2O_3 were also fabricated, exhibiting gravimetric capacities strikingly similar to elemental Sb electrodes.

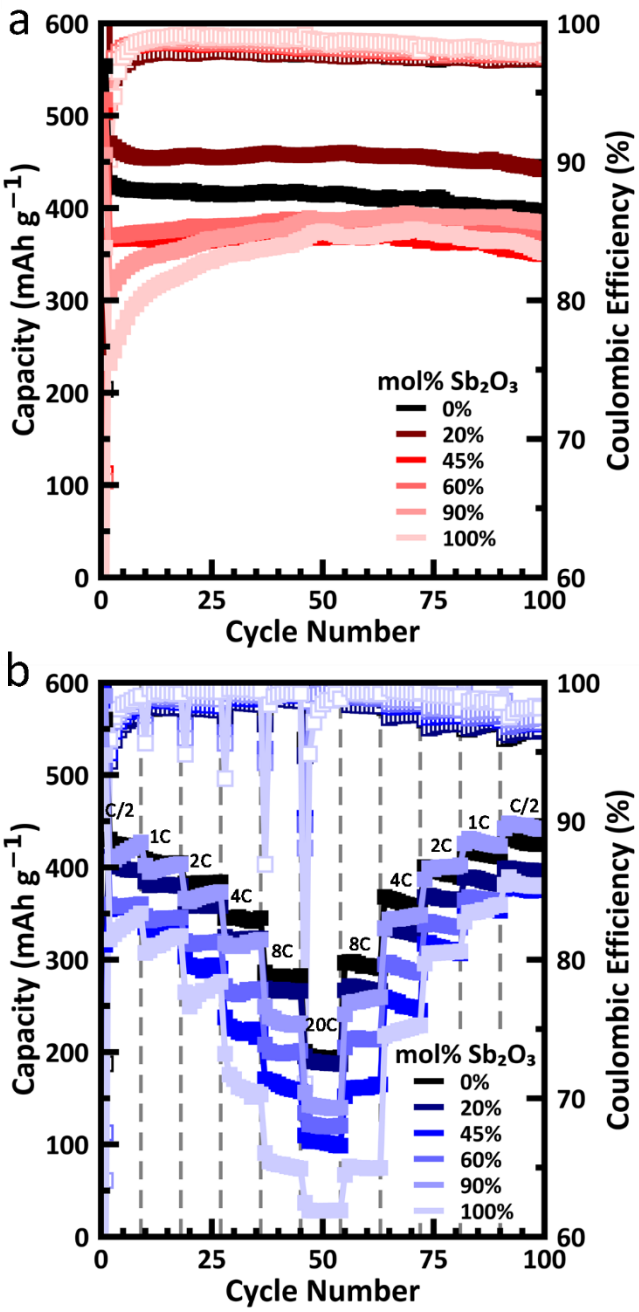

Figure 6-4. (a) Capacity and coulombic efficiency of Na-ion battery negative electrodes fabricated using antimony nanocrystals that had been subjected to varying degrees of oxide formation (1C cycling rate in 1M $NaClO_4$ 90% propylene carbonate / 10% fluoroethylene carbonate electrolyte), and (b) the associated rate test. Note that the reported gravimetric capacities have a ±10% uncertainty (Table 6-2).

After initial cycling, sodiation and desodiation occur via separate reaction pathways for sodium antimonide and sodium oxide for all but the lowest states of sodiation.[173] The initial sodiation step (0.87 V) in each cycle results in a reaction product of antimony plus sodium oxide (Na_2O), while the final desodiation step (1.25-2 V) results in partial desodiation of the oxide (Na_2O) and the concomitant formation of amorphous Sb_2O_3.[173] Thus, electrochemical reactions corresponding to the sodiation (below 0.87 V) and desodiation (below 1.25 V) of sodium antimonide are observed in all Sb/Sb_2O_3 samples after initial cycling (Figure 6-5).[42]

For full utilization of the theoretical gravimetric capacity of Sb_2O_3, one would expect strong peaks with large areas corresponding to the sodium-oxygen redox couple at 0.87/1.25-2 V in the differential capacity plots (Figure 6-5);[16,173] however, this is clearly not the case, with the areas associated with the initial sodiation (0.87 V) and final desodiation (1.25-2 V) of the oxide corresponding to a very small fraction of the reversible charge storage capacity in the differential capacity plots (Figure 6-5). Instead, the vast majority of reversible charge storage capacity corresponds to sodiation/desodiation of sodium antimonide (sodiation from a-NaSb to a-$Na_{1.7}Sb$, a-$Na_{1.7}Sb$ to a-$Na_{3-x}Sb$, c-Sb to a-$Na_{3-x}Sb$, and a-$Na_{3-x}Sb$ to c-Na_3Sb at ~0.73 V, ~0.6 V, ~0.4 V, and ~0.2 V, respectively, and desodiation from c-Na_3Sb to a-$Na_{1.7}Sb$, a-$Na_{1.7}Sb$ to a-NaSb, and a-NaSb to c-Sb at 0.8 V, ~0.82 V, and ~0.88 V, respectively)[38,42,44] Therefore, the lack of reversible sodiation and desodiation of the oxide is responsible for most of the underutilization of Sb_2O_3 relative to its reported theoretical sodium storage capacity.

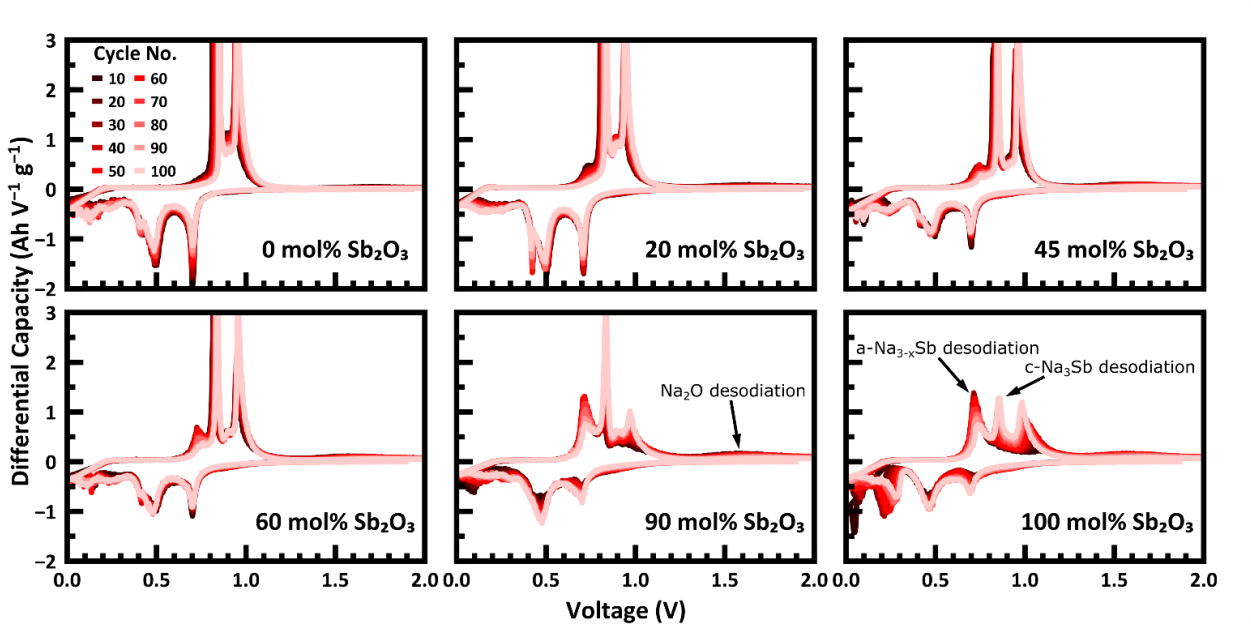

Figure 6-5. Differential capacity of oxidized antimony nanocrystal Na-ion battery negative electrodes cycled at 1C in 1M $NaClO_4$ 90% propylene carbonate / 10% fluoroethylene carbonate electrolyte, demonstrating increased amorphization with increased oxide content.

Increased oxide content reduces the fraction of the antimony that reaches the c-Na_3Sb terminal sodiation state (~0.2 V during sodiation, Figure 6-5), particularly for the 90 and 100 mol% oxidized samples during initial cycling.[42] Instead, sodiation stops at the amorphous sodium antimonide phase (a-$Na_{3-x}Sb$, where x is close to zero), which occurs at ~0.4 V during sodiation (Figure 6-5). [42] The reduced intensity of the peak associated with c-Na_3Sb sodiation during initial cycling correlates with the burn-in period for the samples with significant oxide content (Figure 6-4)). Furthermore, the a-$Na_{3-x}Sb$ to c-Na_3Sb sodiation exhibits a broad peak characteristic of a solid-solution reaction and occurs close to the lower cut-off voltage (0.02 V).[186] Notably, previous observations have shown that small amounts of Sb_2O_3 formation can lead to increased capacity retention, even when the maximum voltage is reduced to 1.5 V.[169] This has been previously attributed to Na_2O buffering the stress and strain associated with the volume expansion of the

alloying process (~290% for pure antimony);[17] however, our observation that increased oxidation results in a larger fraction of the sample stopping sodiation at the a-$Na_{3-x}Sb$ phase provides further mechanistic insight into the increased capacity retention of slightly oxidized antimony electrodes. Stress in amorphous phases is generally lower than stress in crystalline phases during cycling because the amorphous phases are less ordered and can more readily undergo plastic deformation instead of cracking.[187,188] Consequently, since stress-related damage is one of the primary causes of capacity loss in alloying active materials,[22,33,189,190] increased amorphous material in the nanocrystals during cycling leads to increased capacity retention. Overall, the 1C cycling data shown in Figure 6-5 indicates that oxidation suppresses the crystalline phases, particularly during initial cycling, and that utilization of the oxygen in Sb_2O_3 for reversible sodium storage is low.

The transition from a-$Na_{3-x}Sb$ to c-Na_3Sb becomes easier after extended cycling at high oxidation levels, enabling a more complete capacity utilization for the antimony component of the Sb_2O_3 (Figure 6-5). During initial cycling, due to the low utilization of Sb_2O_3 described above, much of the active material is still crystalline Sb_2O_3. As can be seen in Figure 6-5, the higher oxidation levels require a larger overpotential to reach the c-Na_3Sb phase than the lower oxidation levels – ~0.2 V c-Na_3sb sodiation peak shifts to lower voltages.[42] During extended cycling, the c-Sb_2O_3 amorphizes.[173] Once the c-Sb_2O_3 is amorphized, the overpotential of sodiation to c-Na_3Sb becomes smaller and increased c-Na_3Sb forms (Figure 6-5). Thus, after extended cycling, the amorphization of crystalline Sb_2O_3 allows the sample to become more fully utilized for the highly oxidation samples.

Oxide content also affects the rate capability of the active material, with rate performance decreasing as oxide content increases (Figure 6-4b). As the cycling rate is increased, less charge

is passed through all of the sodiation and desodiation reactions, with the decrease in capacity most severe in systems with the largest oxide content, leading to essentially no observable electrochemical reactions in the 100 mol% Sb_2O_3 differential capacity plots at a 20C cycling rate (Figure 6-6). The reactions at 90 and 100 mol% Sb_2O_3 are significantly more kinetically limited than the rest of the samples, demonstrating that oxide content has a non-linear, but negative effect on rate capability, with particularly severe effects at high oxide contents.

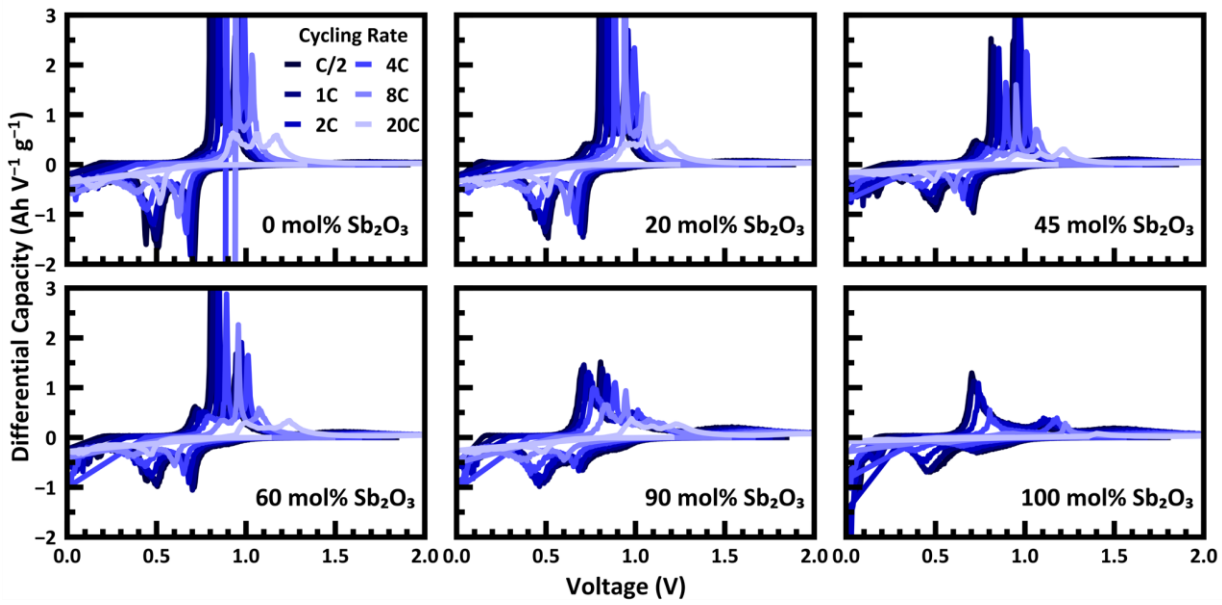

Figure 6-6. Rate-based differential capacity data demonstrating a reduction in the charge passing through all electrochemical reactions as rate is increased, with particularly large effects at high oxide contents.

6.3.3 Thermodynamics and Kinetics of the Sodiation/Desodiation of Sb/Sb_2O_3 nanocrystals

The thermodynamics and kinetics of the Sb/Sb_2O_3 nanocrystal electrodes during electrochemical cycling were studied with a galvanostatic intermittent titration technique (GITT). Galvanostatic Intermittent Titration Technique (GITT) is a pulse-based electrochemical measurement technique whereby an electrochemical cell – in our experiment, a Na-ion half-cell –

is cycled in a stepwise fashion.[80] Each titration step consists of a current pulse of specified time, followed by a relaxation to the thermodynamic equilibrium potential for the given electrochemical state – in our experiment, the state of sodiation. Each current injection step must be small relative to the rest step, in order to allow for Fickian diffusion prior to the next titration step.[191] GITT separates the thermodynamic and kinetic characteristics of the electrochemical cell, providing significant insight into how each component is contributing at a given electrochemical state, with a particular fidelity for the kinetic aspects of the system.[80] In our experiment, we interspersed GITT cycles at a C/10 rate during extended cycling at 1C in order to study the influences and effects of aging on the thermodynamic and kinetic characteristics of the cell. The C/10 GITT analysis was employed at cycles 2, 5, 10, 20, 40, 100, 200, and 400, thus capturing the electrochemical behaviors of Na-ion half cells at various states of aging Figure 6-7.

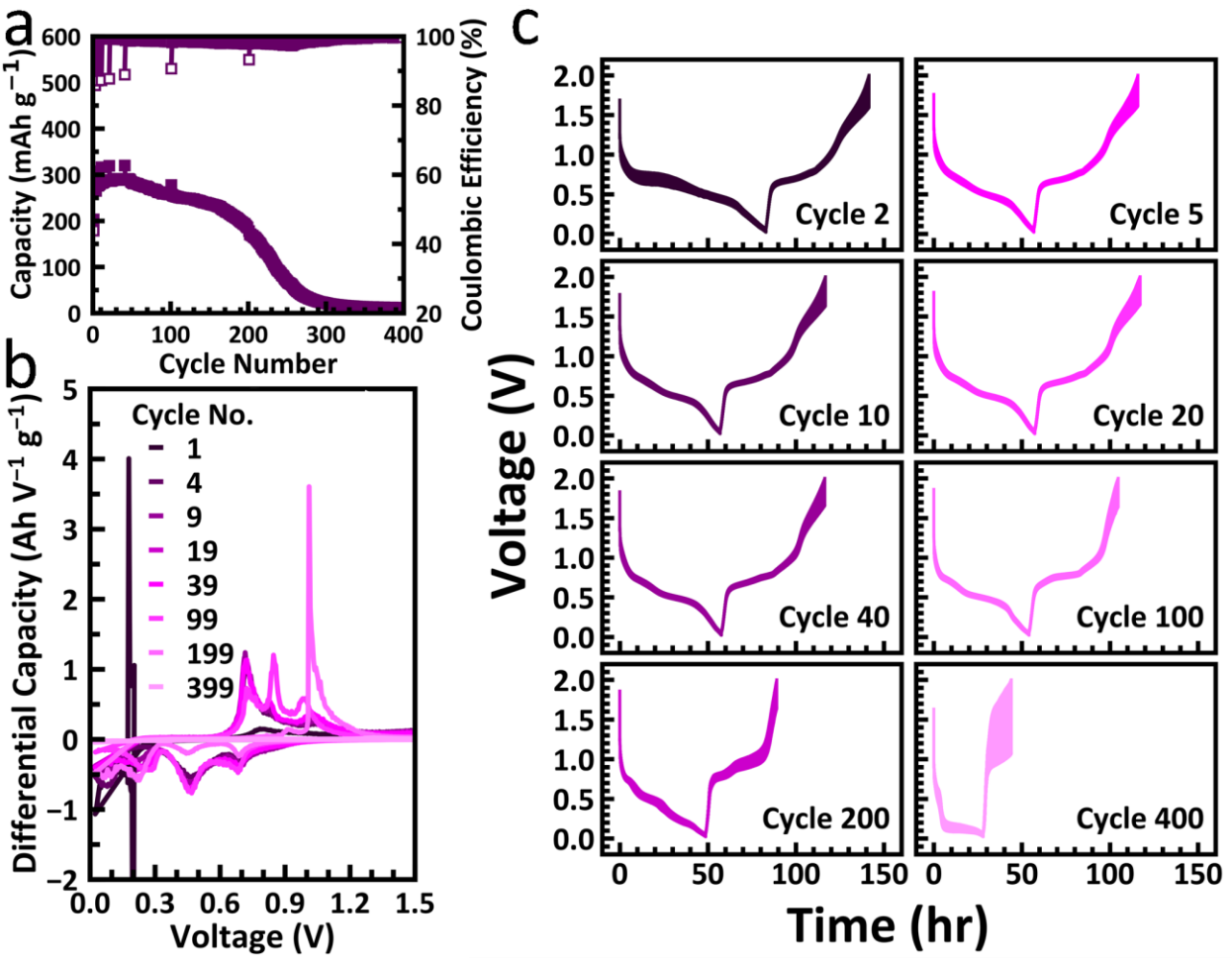

Figure 6-7. a) Capacity and coulombic efficiency, b) differential capacity, and c) time-based coulometric titration curves for a fully oxidized Sb_2O_3 nanocrystal electrode cycled at a rate of 1C during extended cycling and at a C/10 rate during GITT measurements.

For the 100 mol% Sb_2O_3 material, kinetic limitations in the initial sodiation steps between 1.0 and 0.5 V substantially reduce the capacity during initial cycling, as can be seen in the coulometric titration curves (Figure 6-7c and Figure 6-8).[42,173] Since the thickness (vertical width) of a coulometric titration curve is correlated with the kinetic limitations of the associated electrochemical reactions,[81,107] a wider coulometric titration curve indicates that the electrochemical reactions are more kinetically hindered. As can be seen in Figure 6-8, the width

of the coulometric titration curve for the 100 mol% Sb_2O_3 is thicker between 1.0 and 0.5 V for cycle 2 than for any of the subsequent cycles, indicating that sodiation during the initial cycles is more difficult than sodiation for any of the cycles that follow. The rest of the curves appear to have approximately the same width, and so do not differ in terms of kinetic limitations. During initial cycling, at low sodiation states, sodiation occurs via the c-Sb_2O_3 to $Na_xSb_2O_3$ intercalation reaction.[173] After initial cycling, the Sb_2O_3 amorphizes and sodiation at low sodiation states instead proceeds via the addition of Na to a-Sb_2O_3, resulting in the formation of Sb along with a Na_2O alloying reaction.[173] Since the widths of the GITT curves in the 1.0 to 0.5 V region are only wide during initial cycling, this indicates that the c-Sb_2O_3 to $Na_xSb_2O_3$ sodiation is kinetically limited during initial cycling.[42,173]

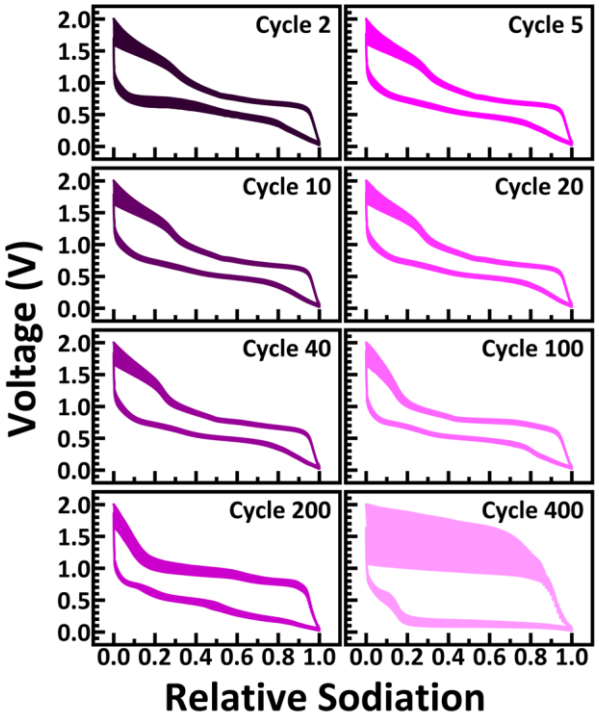

Figure 6-8. Coulometric titration curves showing significant kinetic limitations during desodiation for a 100 mol% Sb_2O_3 nanocrystal electrode cycled at a C/10 rate during GITT measurements.

Relative sodiation states of 0.0 and 1.0 are respectively defined as the minimum and maximum sodiation states achieved during GITT cycling.

Detailed inspection of the shape of each GITT titration step can enable deconvolution of the kinetic limitations associated with each reaction into three components: an IR drop, a reaction overpotential, and a diffusional overpotential (Figure 6-9a).[81] In combination, each of these components drive the overall overpotential of each GITT step.[107] The IR drop is the voltage step-change that is necessary to overcome the configurational resistance of the cell,[81] resulting in a sharp vertical drop that occurs at the start of each current injection step. IR drops should be small for well-designed cell configurations, as is observed at low sodiation levels for the 100 mol% Sb_2O_3 electrode relative to the overpotential, indicating that cell configuration is not responsible for the observed kinetic limitations of the Sb_2O_3 (Figure 6-10a). Although it is clear that the reaction overpotential or the diffusional overpotential is limiting, the reaction overpotential cannot be easily quantitatively accessed by GITT, particularly for electrodes that undergo phase transformation.[81] However, the shape of each current injection step can clearly indicate whether the reaction overpotential or diffusional overpotential is dominant for a particular electrochemical reaction. In cases where the reaction overpotential is dominant, the current injection step will continue with a steep, almost vertical, slope after the initial IR drop. In Figure 6-9b, this characteristic is much more prominent in cycle 2 than in cycle 5 in the 1.0 to 0.5 V sodiation region, indicating that reaction overpotential is the predominant kinetic limitation for sodiation during initial cycling. The kinetically limited c-Sb_2O_3 to $Na_xSb_2O_3$ sodiation reaction is described primarily as an intercalation reaction in the literature,[173] and as can be seen in Figure 6-4 and Figure 6-5, the observed reaction exhibits a broad sodiation peak (1.0 to 0.6 V) which is characteristic of

a solid-solution reaction.[186] In solid-solution reactions, no phase or structural changes occur,[186] and for an intercalation reaction where no phase or structural change occur, the primary form of reaction resistance is typically charge transfer.[159] Together, this suggests that, prior to amorphization of the Sb_2O_3, sodiation is kinetically limited by charge transfer resistance.

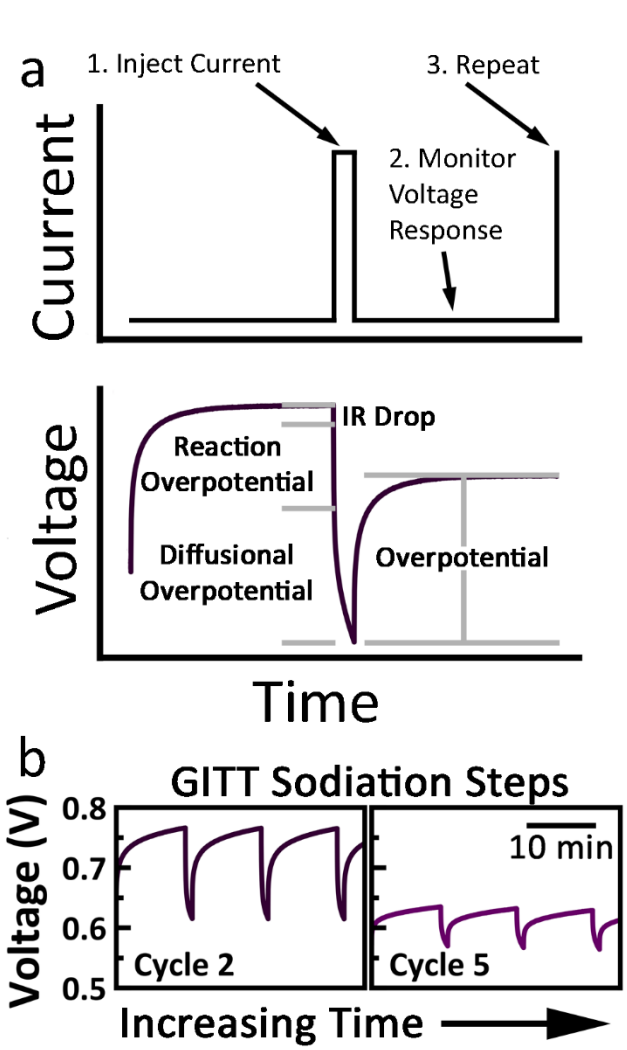

Figure 6-9. a) Schematic decomposition of the characteristic overpotential components for a time-based coulometric titration curve (data shown collected during cycle 2 at a C/10 rate for a fully oxidized Sb_2O_3 nanocrystal electrode), and b) coulometric titration curves for the kinetically

limited region of sodiation during initial GITT steps, showing reduced reaction overpotential after increased cycling at a C/10 rate.

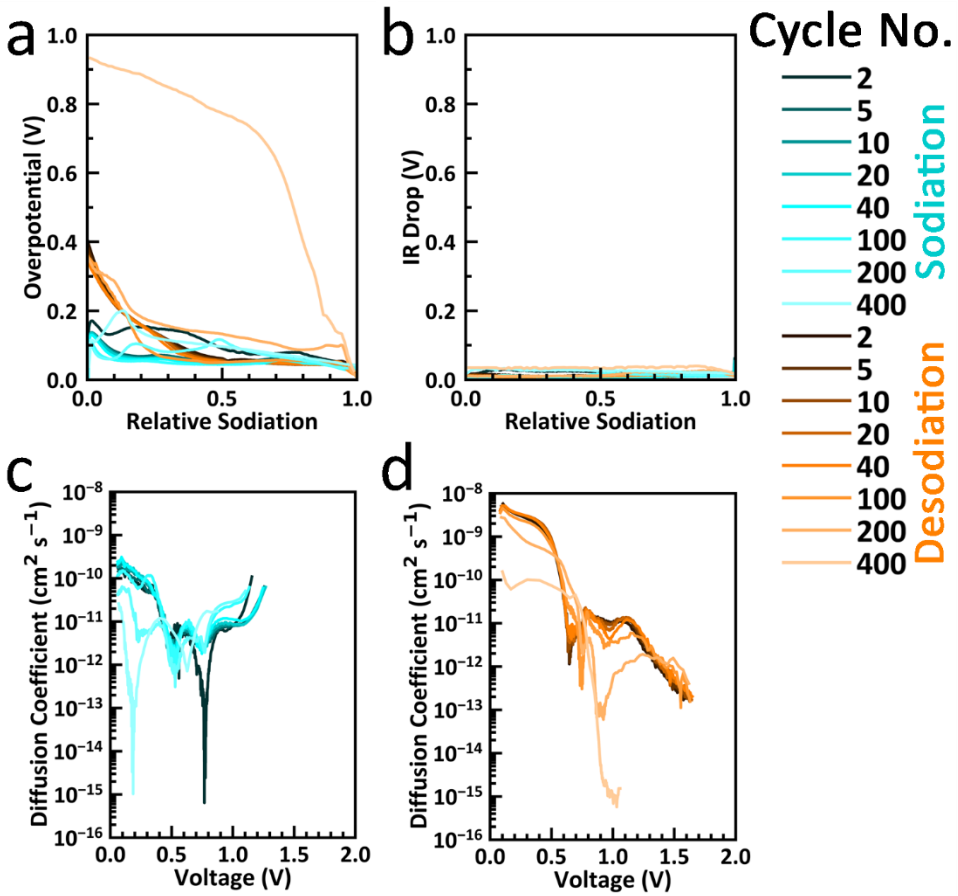

Figure 6-10. a) Overpotential, b) IR drop, and voltage-based c) sodiation and d) desodiation diffusion coefficients for a fully oxidized Sb_2O_3 nanocrystal electrode cycled at a C/10 rate during GITT measurements, where relative sodiation states of 0.0 and 1.0 are respectively defined as the minimum and maximum sodiation states achieved during GITT cycling.

Inspection of Figure 4 indicates that the other kinetically limited region through cycle 100 is the final desodiation reaction that takes place between 1 and 2 V, with the only reaction occurring

in this voltage window corresponding to the desodiation of Na_2O between 1.25 and 2 V.[173] The steep slopes of the current injection steps in the 1.0 to 2.0 V region of the time-based coulometric titration curve (Figure 6-11) indicate that the desodiation of Na_2O is kinetically limited due to a large reaction overpotential, and since the desodiation of Na_2O is an alloying reaction,[173] the kinetic limitations toward desodiation could either be due to charge transfer or structural rearrangement at the interfaces.[186] Irrespective of the specific mechanism, the kinetic limitations for desodiation result in a sequestration of the working ion in the oxide, leading to an underutilization of the active material capacity at the rates tested, as described above.

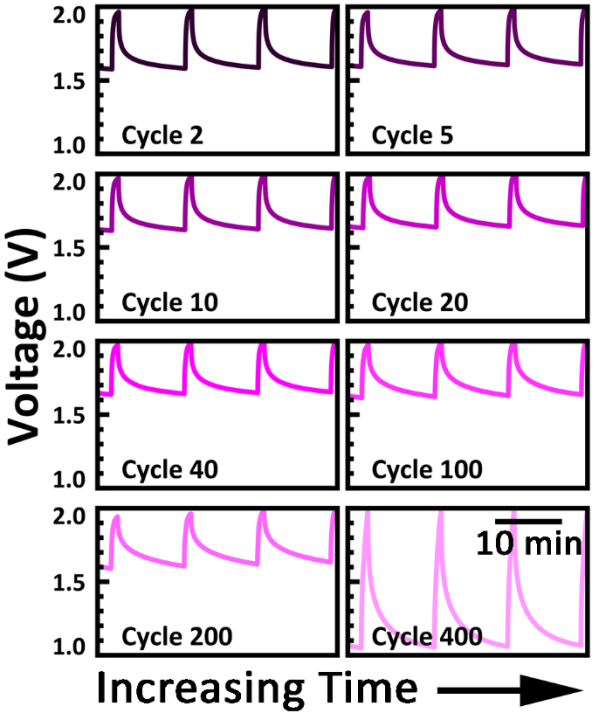

Figure 6-11. Coulometric titration curves for the kinetically limited desodiation of Na_2O during cycling at a C/10 rate for a fully oxidized antimony nanocrystal electrode.

In addition, the coulometric titration curves illuminate the predominant drivers of capacity loss. Through cycle 100, the vertical width of the coulometric titration curves (Figure 6-8) remain the same outside of the 1.0 to 2.0 V Na_2O desodiation region, indicating that capacity losses are not kinetically driven. While capacity losses are small through approximately cycle 175 (Figure 6-7), thereafter, the rate of capacity loss becomes much larger. This transition is correlated with the increased kinetic limitations – particularly during desodiation – that are observed in the GITT measurements (Figure 6-11). By cycle 200, the GITT curve width has increased substantially throughout desodiation, indicating that kinetic limitations are playing a significant role. Moreover, the vertical line portion of the GITT curve that corresponds to reaction overpotential increases between cycle 100 and 200, indicating that the kinetic limitations that correlate with an increased rate of capacity loss are due to difficulties in the desodiation reactions. Desodiation outside of the 1.0 to 2.0 V desodiation region for Na_2O also becomes highly kinetically impeded by cycle 400, with the curved portion of the current injection steps growing in prominence between cycle 200 and 400 (Figure 6-8 and Figure 6-11), indicating that diffusional overpotential is responsible for the increased kinetic limitations. These increased kinetic limitations also correspond to a decrease in diffusion coefficient of two orders of magnitude at low sodiation states during desodiation, relative to cycle 200 (Figure 6-10). Overall, the GITT data illuminates the key kinetic drivers for stable cycling. During extended cycling, reaction overpotentials exhibit the strongest effects on the observed cycling behavior, indicating that modeling the reaction interfaces for Sb_2O_3 sodiation and desodiation would be a particularly interesting area of study for future research, with diffusional overpotentials introducing additional kinetic limitations after significant capacity loss has taken place.

6.3.4 Antimony Oxide Diffusion Coefficient Calculations

While GITT data can be used to quantitatively determine a number of thermodynamic and kinetic parameters, as discussed in the main manuscript,[192] here, we determine the diffusion coefficients of the working ion from the GITT data using the following equation:

$$D = \frac{4}{\pi}\left(\frac{iV_m}{z_A FS}\right)^2 \left[\frac{\left(\frac{dE}{d\delta}\right)}{\left(\frac{dE}{d\sqrt{t}}\right)}\right]^2 \qquad t \ll \frac{L^2}{D} \tag{6-1}$$

where D is the solid-state diffusion coefficient, i is the current, V_m is the molar volume of the electrode, z_A is the charge number of the working ion, F is Faraday's constant, S is the electrochemically active surface area of the electrode, $\frac{dE}{dx}$ is the slope of the equilibrium potentials (the last voltages achieved during the rest steps of the coulometric titration curve, immediately before current injection resumes), $\frac{dE}{d\sqrt{t}}$ is the slope of the linearized charging steps in the coulometric titration curve, t is time, and L is the characteristic size of the electrode material in the diffusion direction (Figure 6-10c,d).[113] For the diffusion coefficients, we assume that diffusion primarily occurs through antimony-rich domains, since the Na_2O that forms is largely electrochemically inactive after initial cycling in our system, as evidenced by the near-negligible broad desodiation peak at 1.6 V, which can be seen in Figure 6-4 and Figure 6-6, along with previous work that has indicated that sodium oxide and sodium antimonide phase-separate during sodiation, and that Na_2O, in its pure form, has been previously shown to block sodium-ion transport.[173,193] Single-particle *in situ* analysis, or synchrotron-based tomographic phase analysis could be used to validate this assumption.[49,194,195]

The diffusion coefficient calculations for a composite electrode with an alloying active material are complicated by factors including the electrochemically active surface area, volume expansion, and phase-transformation reactions. For a composite electrode, the electrochemically

active surface area cannot be readily determined by physical surface area measurement techniques such as Brunauer-Emmett-Teller (BET) adsorption, because the inactive carbon and binder also contribute significantly to the measured surface area.[115] Current research is focused on developing accurate methods to determine the electrochemically active surface area via modelling the complicated porous structures of composite electrodes or directly determining the area via preferential staining of lithiated or sodiated material.[114–116] However, this has only been realized for a small subset of electrode chemistries and is not yet readily generalizable. Thus, in this analysis, we used the superficial surface area to provide rough initial estimates. Notably, the diffusion coefficients (~10^{-9} cm^2 s^{-1}) measured at high sodiation states during desodiation (0.02 V to 0.7 V) are within an order of magnitude of diffusion coefficients determined via potentiostatic intermittent titration technique (PITT) measurements for pure antimony thin films also at high sodiation states during desodiation, validating this approach (Figure 6-10d).[82] As modeling techniques become available for accurate electrochemical surface area evaluation, this data could be reevaluated to improve the accuracy of the measured diffusion coefficients.

Importantly, the molar volume of alloying electrodes changes substantially during cycling, with the transformation from Sb to Na_3Sb representing a ~300% volume expansion.[17] Therefore, the molar volume change for alloying electrodes during cycling must also be taken into account during the diffusion coefficient calculations via the following equation

$$V_m = (1 - x)V_{m,Sb} + xV_{m,Na_3Sb} \quad (6\text{-}2)$$

where x is the relative sodiation level, such that the maximum sodiation state reached during a given sodiation or desodiation step is 1 and the minimum sodiation state reached during a given sodiation or desodiation step is 0, $V_{m,Sb}$ is the molar volume of antimony (18.18 cm^3/mol), and V_{m,Na_3Sb} is the molar volume of Na_3Sb (71.44 cm^3/mol).[66,99] Finally, we note that phase-

transformation reactions can significantly confound GITT-based diffusion coefficient calculations.[118] For example, as can be seen in Figure S4f, the diffusion coefficient during desodiation appears to rapidly drop by approximately five orders of magnitude at 0.8 V, where the two-phase Na_3Sb desodiation occurs. However, the sudden decrease in diffusion coefficient is not actually representative of the diffusive behavior in that region;[118] instead it is representative of the phase transformation that is occurring. In reality, for a typical phase-transformation material, the diffusion coefficient smoothly transitions between the diffusion coefficients of the pure phases. Further refinement of these diffusion coefficients, including taking into account the phase-transformations that occur could be particularly valuable for improving cycle life, since the diffusional overpotential most strongly affects Sb_2O_3 cycling performance after capacity loss.

6.4 Conclusions

In Chapter 6, we systematically studied the performance of antimony nanocrystals with oxidation levels of 0 to 100 mol% Sb_2O_3 as Na-ion battery negative electrodes. We find that capacity retention increases with small amounts of oxide present, as has been previously observed, and attribute this to increased amorphization and suppression of the terminal c-Na_3Sb sodiation state.[169] In contrast to the increased capacity retention associated with small amounts of oxide, cycling rate is adversely affected by increased oxide content, particularly when thick layers of oxide are present. Furthermore, we demonstrate via high-fidelity GITT analysis that oxide formation introduces both kinetic and thermodynamic barriers to sodiation during initial cycling. However, these barriers are reduced by the amorphization of c-Sb_2O_3 during extended cycling, indicating that a burn-in period is required for antimony nanocrystal electrodes with high oxide content. In addition, desodiation of Na_2O is kinetically limited by the large reaction overpotential,

which leads to low reversible sodium storage utilization of the oxide during cycling. Considering that the oxide is responsible for a large fraction of the gravimetric storage capacity of Sb_2O_3, this limitation must be overcome if highly oxidized materials are to be utilized to their maximum potential. Finally, capacity degradation is driven by both thermodynamic and kinetic limitations, with the kinetic limitations leading to sequestration of sodium in the active material. Overall, we have systematically demonstrated that nanocrystalline antimony exhibits significant robustness in both gravimetric capacity and cycling performance with small amounts of oxide, indicating that low-cost, water-based electrode processing represents an ideal path forward for antimony electrode fabrication, irrespective of the inadvertent active material oxidation that may occur.

Chapter 7: Conclusions and Future Work

7.1 Conclusions

7.1.1 Supercritical Fluid Synthesis of Highly Anisotropic Antimony Nanoplatelets

In Chapter 2, we explore the supercritical fluid-based synthesis of antimony nanostructures and microstructures using a triphenylantimony precursor in an anhydrous toluene solvent. We find minimal precursor decomposition below 375°C. At elevated temperatures, we find that the product morphology can be selectively tuned, with high precursor concentrations leading to dendritic growth and intermediate concentrations at high temperature (500°C) resulting in microsized truncated octahedra. Most interestingly, we demonstrate that ultrathin, highly anisotropic antimony nanoplatelets with lateral dimensions of many micrometers and aspect ratios in excess of 1000:1 form in the rest of the explored parameter space with thicknesses between 30 and 80 nm (average thickness of 50±10 nm). The lateral dimension of these platelets can extend to in excess of 100 μm under certain conditions. While the product morphology is relatively insensitive to ligand addition, we also find that the addition of small amounts of oleic acid under air-free growth conditions resulted in the formation of Sb_2O_3 microoctahedra, due to the reaction of oleic acid with the triphenylantimony precursor. The ultrathin antimony nanoplatelets may have possible applications for the development and study of topological and 2D materials.

7.1.2 Morphology-Dependent Electrochemical Characteristics of Antimony Nanomaterials

In Chapter 3, we use the highly anisotropic antimony nanoplatelets as a model system to study the impacts of morphology on the electrochemical sodiation nanostructured antimony. Relative to small, isotropic antimony nanocrystals, the antimony nanoplatelets experience significantly more strain during cycling, leading to increased crystallization and suppression of amorphous phases – most notably, suppression of the previously unassigned a-$Na_{3-x}Sb$ desodiation

peak that occurs at 0.72 V. In addition, using a high-fidelity galvanostatic intermittent titration technique we demonstrate that this leads to increased strain-driven kinetic overpotentials above ~0.9 V in the highly anisotropic antimony nanoplatelets that occur immediately upon cycling. Through this analysis we elucidate that these kinetic hindrances are the source of the previously observed difficulty in desodiation beyond a-NaSb.[42] We also find that for both the antimony nanocrystals and antimony nanoplatelets, the diffusional overpotential during desodiation at voltages greater than ~0.9 V correlates strongly with the capacity reductions. These results suggest that minimizing the diffusional overpotential at voltages greater than ~0.9 V is critical to increasing both capacity and capacity retention in antimony electrode materials. Furthermore, we find that the anisotropy and size dispersion of the antimony nanoplatelets leads to unfavorable electrode heterogeneity that also negatively impacts performance. Therefore, controlling the morphology of antimony-based active materials is critical to obtaining high performance both on an individual particle level and on an electrode composite level, with decreased anisotropy driving increased performance at both levels.

7.1.3 *In Situ* XRD of Antimony Na-Ion Battery Electrodes After Extended Cycling

The emergence of a previously unidentified desodiation reaction that appears at 0.93 V after extended cycling occurs during antimony nanomaterial cycling. *In situ* XRD measurements carried out on antimony alloying electrodes after extended cycling associate the emergence of this electrochemical feature with the presence of crystalline NaSb. We note that the micrometer-scale lateral dimensions of the nanoplatelets enable the collection of interpretable *in situ* XRD signal relative to the nanometer-scale dimensions of the nanocrystals. Overall, these observations, in conjunction with previous thermodynamic calculations in the literature, lead us to attribute this electrochemical reaction to the desodiation of crystalline NaSb – a thermodynamically favorable,

but largely undiscussed source of capacity in antimony electrodes – demonstrating that crystalline NaSb plays an increasingly important role in antimony-based Na-ion battery alloying electrodes after extended cycling.

7.1.4 Temperature-Dependent Electrochemical Characteristics of Antimony Nanocrystals

Using electrochemical impedance spectroscopy and differential capacity measurements, we demonstrate that charge transfer resistance is the main source of capacity reduction (~100 mAh g^{-1}, ~20%) for antimony nanocrystal composite electrodes as the cycling temperature is decreased from 50 to 5°C. The increase in charge transfer resistance with reduced temperatures is primarily driven by the increased difficulty of Na-ion transport across the SEI layer-electrode interface. As the cycling characteristics of the antimony nanocrystal composite electrodes are highly reversible, we find that primarily irreversible sources of capacity loss, such as sodium deposition and subsequent SEI layer formation, are not major sources of the capacity reduction with reduced temperature under the investigated conditions. Furthermore, we show negligible contributions to the capacity reduction at low temperatures from the double layer capacitance, resistive and capacitive contributions from charge transfer or ion mobility through the solid-electrolyte interphase (SEI) layer, and the rate of solid-state diffusion in the antimony nanocrystals. Overall, these results suggest that rational modification of the SEI layer composition could potentially increase the low-temperature capacity of antimony nanocrystal composite electrodes.

7.1.5 Electrochemical Characteristics of Systematically Oxidized Antimony Nanocrystal Alloying Electrodes

In Chapter 6, we systematically studied the performance of antimony nanocrystals with oxidation levels of 0 to 100 mol% Sb_2O_3 as Na-ion battery negative electrodes. We find that capacity retention increases with small amounts of oxide present, as has been previously observed,

and attribute this to increased amorphization and suppression of the terminal c-Na_3Sb sodiation state.[169] In contrast to the increased capacity retention associated with small amounts of oxide, cycling rate is adversely affected by increased oxide content, particularly when thick layers of oxide are present. Furthermore, we demonstrate via high-fidelity GITT analysis that oxide formation introduces both kinetic and thermodynamic barriers to sodiation during initial cycling. However, these barriers are reduced by the amorphization of c-Sb_2O_3 during extended cycling, indicating that a burn-in period is required for antimony nanocrystal electrodes with high oxide content. In addition, desodiation of Na_2O is kinetically limited by the large reaction overpotential, which leads to low reversible sodium storage utilization of the oxide during cycling. Considering that the oxide is responsible for a large fraction of the gravimetric storage capacity of Sb_2O_3, this limitation must be overcome if highly oxidized materials are to be utilized to their maximum potential. Finally, capacity degradation is driven by both thermodynamic and kinetic limitations, with the kinetic limitations leading to sequestration of sodium in the active material. Overall, we have systematically demonstrated that nanocrystalline antimony exhibits significant robustness in both gravimetric capacity and cycling performance with small amounts of oxide, indicating that low-cost, water-based electrode processing represents an ideal path forward for antimony electrode fabrication, irrespective of the inadvertent active material oxidation that may occur.

7.2 Future Directions

In the future, antimony has the potential to be commercialized as a high-power, high capacity negative electrode for both Li-ion and Na-ion batteries. However, critical areas of research remain along the commercialization pathway. Much of the work herein that was performed for Na-ion batteries could be done for Li-ion batteries as well, particularly the temperature-dependence and

oxidation-dependence studies. There is also room to refine and optimize antimony-nanomaterial electrode performance further in Na-ion batteries.

Developing a deeper understanding of the morphology-based limitations on performance would be valuable. While the low-cost antimony nanocrystals exhibit high-performance, they are synthesized without any surface functionalization leading to anisotropy, aggregation and a large size dispersion, all of which can inhibit optimal performance. These variables are currently largely left uncontrolled and so a systematic understanding of their effects is needed. Introducing ligands into the antimony nanocrystal synthesis in a controlled fashion could be used to probe these variables systematically, eventually resulting in improved morphological control, both at a single particle and electrode level, leading to further increases in capacity and rate capability. Considering the importance of electrode morphology on rate capability, studying the electrode fabrication procedure for antimony nanocrystal-based electrodes and developing an understanding of the critical variables would also be valuable to improving the understanding of morphological effects on antimony nanomaterial performance. In addition, although outside the realm of batteries, the ultrathin antimony nanoplatelets used in the morphology study may have possible applications for the development and study of topological and 2D materials.

The importance of the SEI layer to temperature-dependent performance indicates that understanding the SEI layer chemistry is critical to improving antimony nanomaterial-based electrodes, further indicating the value of more detailed surface chemistry studies for antimony electrode materials. Systematically surface-functionalizing the antimony nanocrystals can provide further insight into the SEI layer temperature effects and dovetails well with the extensions described above for the morphology-related areas of study. In addition, studying alternative electrolyte chemistries with varied solvents, additives and salts can also provide insight into the

SEI layer temperature effects. SEI layer modification represents an interesting avenue for further antimony nanomaterial-based electrode research.

Developing a stronger understanding the drivers for degradation for both the antimony and antimony oxide nanocrystals would also be valuable. While most of the degradation is primarily driven by diffusion-based limitations to desodiation, the initial causes for degradation are not as clear. Understanding the source of the initial drop-offs in capacity for these materials would be valuable in increasing their lifetime. *In situ* and *ex situ* analysis during and after cycling respectively, would be critical in identifying the changes in the cell that correlate with this initial degradation. These studies would seek to correlate changes in the electrode properties such as the SEI layer chemistry and thickness or the electrode morphology and active material distribution to the capacity loss. If a correlation can be found, future work would relate to systematically modifying the relevant electrode parameters to understand the initial degradation drivers. Extending this work to understand if the small initial capacity losses lead to the large kinetic limitations during desodiation that in turn drive a more rapid capacity loss would represent the next step forward in these studies. In addition, the exact relationship between the c-NaSb phase that forms during degradation and the capacity loss is unclear. Further research to determine if the c-NaSb phase drives degradation or is only a symptom is critical to developing a full understanding of antimony electrode degradation.

More generally, the high-fidelity GITT and the sample preparation techniques for the AFM-based electrode morphology analysis used in our studies are potentially interesting for other electrode materials. The high-fidelity GITT offers significant improvement in resolution relative to most GITT analysis in the literature. Combined with long-term cycling this technique offers

improved insight into the drivers for electrode capacity loss and can be used to pinpoint the exact electrochemical reactions that lead to the performance losses.

The sample preparation techniques for the AFM-based electrode morphology analysis support the analysis of electrode materials that have large z-heights. Traditional AFM-based battery electrode analysis can only access materials with limited z-height without producing large artifacts in the data or causing instrument damage. Therefore, certain electrodes, such as semiconductor nanowire fabric electrodes, are difficult to study with AFM due to the high porosity and large z-height variations. Epoxying and slicing a representative piece of the electrode material as detailed in section 3.4 represents a way to avoid this issue as the slice is thin enough to avoid AFM data artifacts or equipment damage but still provides data that is characteristic of the whole electrode. This approach widens the range of electrode materials which can be studied to understand nanoscale morphology and conductivity via AFM. Considering that AFM is much more readily available than other techniques traditionally used to study these types of properties such as synchrotron or TEM-based single particle experiments, this sample preparation approach can dramatically increase the understanding of nanoscale phenomena in battery electrode materials.

These future directions provide further insight into antimony electrode performance and degradation, particularly with regards to key parameters that are not yet ideally optimized for commercialization. In addition, some of the techniques we have used to study antimony herein can be more broadly applied and support the study and understanding of other electrode materials. Overall these future directions offer the ability to significantly impact the understanding, development and commercialization of many battery electrode materials.

Bibliography

(1) Yu, L.; Jiang, T.; Cao, Y.; Qi, Q. Carbon-Aware Energy Cost Minimization for Distributed Internet Data Centers in Smart Microgrids. *IEEE Internet of Things Journal* **2014**, *1* (3), 255–264. https://doi.org/10.1109/JIOT.2014.2322606.

(2) Allan, G.; Eromenko, I.; Gilmartin, M.; Kockar, I.; McGregor, P. The Economics of Distributed Energy Generation: A Literature Review. *Renewable and Sustainable Energy Reviews* **2015**, *42*, 543–556. https://doi.org/10.1016/j.rser.2014.07.064.

(3) Poudineh, R.; Jamasb, T. Distributed Generation, Storage, Demand Response and Energy Efficiency as Alternatives to Grid Capacity Enhancement. *Energy Policy* **2014**, *67*, 222–231. https://doi.org/10.1016/j.enpol.2013.11.073.

(4) Smith, J.; Rogers, B.; Taylor, J.; Roark, J.; Neenan, B.; Mimnagh, T.; Takayesu, E. Time and Location: What Matters Most When Valuing Distributed Energy Resources. *IEEE Power and Energy Magazine* **2017**, *15* (2), 29–39. https://doi.org/10.1109/MPE.2016.2639178.

(5) Hirth, L.; Ueckerdt, F.; Edenhofer, O. Integration Costs Revisited – An Economic Framework for Wind and Solar Variability. *Renewable Energy* **2015**, *74*, 925–939. https://doi.org/10.1016/j.renene.2014.08.065.

(6) Ueckerdt, F.; Pietzcker, R.; Scholz, Y.; Stetter, D.; Giannousakis, A.; Luderer, G. Decarbonizing Global Power Supply under Region-Specific Consideration of Challenges and Options of Integrating Variable Renewables in the REMIND Model. *Energy Economics* **2017**, *64*, 665–684. https://doi.org/10.1016/j.eneco.2016.05.012.

(7) Ray, D. *Lazard's Levelized Cost of Energy Analysis—Version 12.0*; 2018.

(8) Nosratabadi, S. M.; Hooshmand, R.-A.; Gholipour, E. A Comprehensive Review on Microgrid and Virtual Power Plant Concepts Employed for Distributed Energy Resources Scheduling in Power Systems. *Renewable and Sustainable Energy Reviews* **2017**, *67*, 341–363. https://doi.org/10.1016/j.rser.2016.09.025.

(9) Krieger, E. M.; Casey, J. A.; Shonkoff, S. B. C. A Framework for Siting and Dispatch of Emerging Energy Resources to Realize Environmental and Health Benefits: Case Study on Peaker Power Plant Displacement. *Energy Policy* **2016**, *96*, 302–313. https://doi.org/10.1016/j.enpol.2016.05.049.

(10) Kaschub, T.; Jochem, P.; Fichtner, W. Solar Energy Storage in German Households: Profitability, Load Changes and Flexibility. *Energy Policy* **2016**, *98*, 520–532. https://doi.org/10.1016/j.enpol.2016.09.017.

(11) M. Gür, T. Review of Electrical Energy Storage Technologies, Materials and Systems: Challenges and Prospects for Large-Scale Grid Storage. *Energy & Environmental Science* **2018**, *11* (10), 2696–2767. https://doi.org/10.1039/C8EE01419A.

(12) Lawrence Livermore National Laboratory. Estimated U.S. Energy Consumption in 2018 https://flowcharts.llnl.gov/content/assets/images/charts/Energy/Energy_2018_United-States.png (accessed Aug 26, 2019).

(13) Reddy, T. B. *Linden's Handbook of Batteries*; McGraw-hill New York, 2011; Vol. 4.

(14) Oszajca, M. F.; Bodnarchuk, M. I.; Kovalenko, M. V. Precisely Engineered Colloidal Nanoparticles and Nanocrystals for Li-Ion and Na-Ion Batteries: Model Systems or Practical Solutions? *Chem. Mater.* **2014**, *26* (19), 5422–5432. https://doi.org/10.1021/cm5024508.

(15) Nitta, N.; Wu, F.; Lee, J. T.; Yushin, G. Li-Ion Battery Materials: Present and Future. *Materials Today* **2015**, *18* (5), 252–264. https://doi.org/10.1016/j.mattod.2014.10.040.
(16) He, M.; Kravchyk, K.; Walter, M.; Kovalenko, M. V. Monodisperse Antimony Nanocrystals for High-Rate Li-Ion and Na-Ion Battery Anodes: Nano versus Bulk. *Nano Lett.* **2014**, *14* (3), 1255–1262. https://doi.org/10.1021/nl404165c.
(17) Walter, M.; Erni, R.; Kovalenko, M. V. Inexpensive Antimony Nanocrystals and Their Composites with Red Phosphorus as High-Performance Anode Materials for Na-Ion Batteries. *Scientific Reports* **2015**, *5*, 8418. https://doi.org/10.1038/srep08418.
(18) Mikolajczak, C.; Kahn, M.; White, K.; Long, R. T. *Lithium-Ion Batteries Hazard and Use Assessment*; SpringerBriefs in Fire; Springer US: Boston, MA, 2011. https://doi.org/10.1007/978-1-4614-3486-3.
(19) Li, Q.; Li, Z.; Zhang, Z.; Li, C.; Ma, J.; Wang, C.; Ge, X.; Dong, S.; Yin, L. Low-Temperature Solution-Based Phosphorization Reaction Route to Sn_4P_3/Reduced Graphene Oxide Nanohybrids as Anodes for Sodium Ion Batteries. *Adv. Energy Mater.* **2016**, *6* (15), 1600376. https://doi.org/10.1002/aenm.201600376.
(20) Obrovac, M. N.; Chevrier, V. L. Alloy Negative Electrodes for Li-Ion Batteries. *Chem. Rev.* **2014**, *114* (23), 11444–11502. https://doi.org/10.1021/cr500207g.
(21) Chockla, A. M.; Harris, J. T.; Akhavan, V. A.; Bogart, T. D.; Holmberg, V. C.; Steinhagen, C.; Mullins, C. B.; Stevenson, K. J.; Korgel, B. A. Silicon Nanowire Fabric as a Lithium Ion Battery Electrode Material. *J. Am. Chem. Soc.* **2011**, *133* (51), 20914–20921. https://doi.org/10.1021/ja208232h.
(22) Pharr, M.; Choi, Y. S.; Lee, D.; Oh, K. H.; Vlassak, J. J. Measurements of Stress and Fracture in Germanium Electrodes of Lithium-Ion Batteries during Electrochemical Lithiation and Delithiation. *Journal of Power Sources* **2016**, *304*, 164–169. https://doi.org/10.1016/j.jpowsour.2015.11.036.
(23) Choi, J. W.; Cui, Y.; Nix, W. D. Size-Dependent Fracture of Si Nanowire Battery Anodes. *Journal of the Mechanics and Physics of Solids* **2011**, *59* (9), 1717–1730. https://doi.org/10.1016/j.jmps.2011.06.003.
(24) Xu, J.; Deshpande, R. D.; Pan, J.; Cheng, Y.-T.; Battaglia, V. S. Electrode Side Reactions, Capacity Loss and Mechanical Degradation in Lithium-Ion Batteries. *J. Electrochem. Soc.* **2015**, *162* (10), A2026–A2035. https://doi.org/10.1149/2.0291510jes.
(25) Ning, G.; Popov, B. N. Cycle Life Modeling of Lithium-Ion Batteries. *J. Electrochem. Soc.* **2004**, *151* (10), A1584–A1591. https://doi.org/10.1149/1.1787631.
(26) Zhang, Q.; Pan, J.; Lu, P.; Liu, Z.; Verbrugge, M. W.; Sheldon, B. W.; Cheng, Y.-T.; Qi, Y.; Xiao, X. Synergetic Effects of Inorganic Components in Solid Electrolyte Interphase on High Cycle Efficiency of Lithium Ion Batteries. *Nano Lett.* **2016**, *16* (3), 2011–2016. https://doi.org/10.1021/acs.nanolett.5b05283.
(27) Li, Z.; Tan, X.; Li, P.; Kalisvaart, P.; Janish, M. T.; Mook, W. M.; Luber, E. J.; Jungjohann, K. L.; Carter, C. B.; Mitlin, D. Coupling In Situ TEM and Ex Situ Analysis to Understand Heterogeneous Sodiation of Antimony. *Nano Lett.* **2015**, *15* (10), 6339–6348. https://doi.org/10.1021/acs.nanolett.5b03373.
(28) Darwiche, A.; Marino, C.; Sougrati, M. T.; Fraisse, B.; Stievano, L.; Monconduit, L. Better Cycling Performances of Bulk Sb in Na-Ion Batteries Compared to Li-Ion Systems: An Unexpected Electrochemical Mechanism. *J. Am. Chem. Soc.* **2012**, *134* (51), 20805–20811. https://doi.org/10.1021/ja310347x.

(29) Zhou, J.; Qian, T.; Wang, M.; Xu, N.; Zhang, Q.; Li, Q.; Yan, C. Core–Shell Coating Silicon Anode Interfaces with Coordination Complex for Stable Lithium-Ion Batteries. *ACS Appl. Mater. Interfaces* **2016**, *8* (8), 5358–5365. https://doi.org/10.1021/acsami.5b12392.

(30) Zhang, L. Q.; Liu, X. H.; Liu, Y.; Huang, S.; Zhu, T.; Gui, L.; Mao, S. X.; Ye, Z. Z.; Wang, C. M.; Sullivan, J. P.; et al. Controlling the Lithiation-Induced Strain and Charging Rate in Nanowire Electrodes by Coating. *ACS nano* **2011**, *5* (6), 4800–4809.

(31) Li, S.; Niu, J.; Zhao, Y. C.; So, K. P.; Wang, C.; Wang, C. A.; Li, J. High-Rate Aluminium Yolk-Shell Nanoparticle Anode for Li-Ion Battery with Long Cycle Life and Ultrahigh Capacity. *Nat Commun* **2015**, *6*, 7872. https://doi.org/10.1038/ncomms8872.

(32) Jung, S. C.; Choi, J. W.; Han, Y.-K. Anisotropic Volume Expansion of Crystalline Silicon during Electrochemical Lithium Insertion: An Atomic Level Rationale. *Nano Lett.* **2012**, *12* (10), 5342–5347. https://doi.org/10.1021/nl3027197.

(33) Chan, C. K.; Peng, H.; Liu, G.; McIlwrath, K.; Zhang, X. F.; Huggins, R. A.; Cui, Y. High-Performance Lithium Battery Anodes Using Silicon Nanowires. *Nat Nano* **2008**, *3* (1), 31–35. https://doi.org/10.1038/nnano.2007.411.

(34) Zhu, Y.; Han, X.; Xu, Y.; Liu, Y.; Zheng, S.; Xu, K.; Hu, L.; Wang, C. Electrospun Sb/C Fibers for a Stable and Fast Sodium-Ion Battery Anode. *ACS Nano* **2013**, *7* (7), 6378–6386. https://doi.org/10.1021/nn4025674.

(35) Liang, L.; Xu, Y.; Wang, C.; Wen, L.; Fang, Y.; Mi, Y.; Zhou, M.; Zhao, H.; Lei, Y. Large-Scale Highly Ordered Sb Nanorod Array Anodes with High Capacity and Rate Capability for Sodium-Ion Batteries. *Energy & Environmental Science* **2015**, *8* (10), 2954–2962. https://doi.org/10.1039/C5EE00878F.

(36) Liu, J.; Yu, L.; Wu, C.; Wen, Y.; Yin, K.; Chiang, F.-K.; Hu, R.; Liu, J.; Sun, L.; Gu, L.; et al. New Nanoconfined Galvanic Replacement Synthesis of Hollow Sb@C Yolk–Shell Spheres Constituting a Stable Anode for High-Rate Li/Na-Ion Batteries. *Nano Lett.* **2017**, *17* (3), 2034–2042. https://doi.org/10.1021/acs.nanolett.7b00083.

(37) Tian, W.; Zhang, S.; Huo, C.; Zhu, D.; Li, Q.; Wang, L.; Ren, X.; Xie, L.; Guo, S.; Chu, P. K.; et al. Few-Layer Antimonene: Anisotropic Expansion and Reversible Crystalline-Phase Evolution Enable Large-Capacity and Long-Life Na-Ion Batteries. *ACS Nano* **2018**, *12* (2), 1887–1893. https://doi.org/10.1021/acsnano.7b08714.

(38) Baggetto, L.; Hah, H.-Y.; Jumas, J.-C.; Johnson, C. E.; Johnson, J. A.; Keum, J. K.; Bridges, C. A.; Veith, G. M. The Reaction Mechanism of SnSb and Sb Thin Film Anodes for Na-Ion Batteries Studied by X-Ray Diffraction, ^{119}Sn and ^{121}Sb Mössbauer Spectroscopies. *Journal of Power Sources* **2014**, *267*, 329–336. https://doi.org/10.1016/j.jpowsour.2014.05.083.

(39) Fan, X.-Y.; Han, J.; Jiang, Y.; Ni, J.; Gou, L.; Li, D.-L.; Li, L. Hierarchical Porous Sb Films on 3D Cu Substrate Have Promise for Stable Sodium Storage. *ACS Appl. Energy Mater.* **2018**, *1* (8), 3598–3602. https://doi.org/10.1021/acsaem.8b00872.

(40) Li, X.; Sun, M.; Ni, J.; Li, L. Template-Free Construction of Self-Supported Sb Prisms with Stable Sodium Storage. *Advanced Energy Materials* **2019**, *9* (24), 1901096. https://doi.org/10.1002/aenm.201901096.

(41) Liu, Y.; Zhou, B.; Liu, S.; Ma, Q.; Zhang, W.-H. Galvanic Replacement Synthesis of Highly Uniform Sb Nanotubes: Reaction Mechanism and Enhanced Sodium Storage Performance. *ACS Nano* **2019**, *13* (5), 5885–5892. https://doi.org/10.1021/acsnano.9b01660.

(42) Allan, P. K.; Griffin, J. M.; Darwiche, A.; Borkiewicz, O. J.; Wiaderek, K. M.; Chapman, K. W.; Morris, A. J.; Chupas, P. J.; Monconduit, L.; Grey, C. P. Tracking Sodium-Antimonide Phase Transformations in Sodium-Ion Anodes: Insights from Operando Pair Distribution Function Analysis and Solid-State NMR Spectroscopy. *Journal of the American Chemical Society* **2016**, *138* (7), 2352–2365. https://doi.org/10.1021/jacs.5b13273.

(43) Caputo, R. An Insight into Sodiation of Antimony from First-Principles Crystal Structure Prediction. *Journal of Elec Materi* **2016**, *45* (2), 999–1010. https://doi.org/10.1007/s11664-015-4260-0.

(44) Darwiche, A.; Fehse, M.; Mahmoud, A.; Fontaine, C. L.; Fraisse, B.; Hermann, R. P.; Doublet, M.-L.; Monconduit, L.; Sougrati, M. T.; Yahia, M. B.; et al. The Electrochemical Sodiation of Sb Investigated by Operando X-Ray Absorption and ^{121}Sb Mössbauer Spectroscopy: What Does One Really Learn? *Batteries* **2018**, *4* (2), 25. https://doi.org/10.3390/batteries4020025.

(45) Darwiche, A.; Bodenes, L.; Madec, L.; Monconduit, L.; Martinez, H. Impact of the Salts and Solvents on the SEI Formation in Sb/Na Batteries: An XPS Analysis. *Electrochimica Acta* **2016**, *207*, 284–292. https://doi.org/10.1016/j.electacta.2016.03.089.

(46) Lu, Y.; Zhang, N.; Jiang, S.; Zhang, Y.; Zhou, M.; Tao, Z.; Archer, L. A.; Chen, J. High-Capacity and Ultrafast Na-Ion Storage of a Self-Supported 3D Porous Antimony Persulfide–Graphene Foam Architecture. *Nano Lett.* **2017**, *17* (6), 3668–3674. https://doi.org/10.1021/acs.nanolett.7b00889.

(47) Luo, W.; Calas, A.; Tang, C.; Li, F.; Zhou, L.; Mai, L. Ultralong Sb_2Se_3 Nanowire-Based Free-Standing Membrane Anode for Lithium/Sodium Ion Batteries. *ACS Appl. Mater. Interfaces* **2016**, *8* (51), 35219–35226. https://doi.org/10.1021/acsami.6b11544.

(48) Jackson, E. D.; Mosby, J. M.; Prieto, A. L. Evaluation of the Electrochemical Properties of Crystalline Copper Antimonide Thin Film Anodes for Lithium Ion Batteries Produced by Single Step Electrodeposition. *Electrochimica Acta* **2016**, *214*, 253–264. https://doi.org/10.1016/j.electacta.2016.07.126.

(49) Gutiérrez-Kolar, J. S.; Baggetto, L.; Sang, X.; Shin, D.; Yurkiv, V.; Mashayek, F.; Veith, G. M.; Shahbazian-Yassar, R.; Unocic, R. R. Interpreting Electrochemical and Chemical Sodiation Mechanisms and Kinetics in Tin Antimony Battery Anodes Using in Situ Transmission Electron Microscopy and Computational Methods. *ACS Appl. Energy Mater.* **2019**, *2* (5), 3578–3586. https://doi.org/10.1021/acsaem.9b00310.

(50) Kalisvaart, W. P.; Xie, H.; Olsen, B. C.; Luber, E. J.; Buriak, J. M. Understanding the Mechanism of Enhanced Cycling Stability in Sn–Sb Composite Na-Ion Battery Anodes: Operando Alloying and Diffusion Barriers. *ACS Appl. Energy Mater.* **2019**, *2* (7), 5133–5139. https://doi.org/10.1021/acsaem.9b00819.

(51) Zhao, Y.; Manthiram, A. High-Capacity, High-Rate Bi–Sb Alloy Anodes for Lithium-Ion and Sodium-Ion Batteries. *Chem. Mater.* **2015**, *27* (8), 3096–3101. https://doi.org/10.1021/acs.chemmater.5b00616.

(52) Arnaiz, M.; Gómez-Cámer, J. L.; Ajuria, J.; Bonilla, F.; Acebedo, B.; Jáuregui, M.; Goikolea, E.; Galceran, M.; Rojo, T. High Performance Titanium Antimonide $TiSb_2$ Alloy for Na-Ion Batteries and Capacitors. *Chem. Mater.* **2018**, *30* (22), 8155–8163. https://doi.org/10.1021/acs.chemmater.8b02639.

(53) Zhang, W.; Zhang, Q.; Shi, Q.; Xin, S.; Wu, J.; Zhang, C.-L.; Qiu, L.; Zhang, C. Facile Synthesis of Carbon-Coated Porous Sb_2Te_3 Nanoplates with High Alkali Metal Ions

Storage. *ACS Appl. Mater. Interfaces* **2019**, *11* (33), 29934–29940. https://doi.org/10.1021/acsami.9b09056.
(54) Edison, E.; Sreejith, S.; Madhavi, S. Melt-Spun Fe–Sb Intermetallic Alloy Anode for Performance Enhanced Sodium-Ion Batteries. *ACS Appl. Mater. Interfaces* **2017**, *9* (45), 39399–39406. https://doi.org/10.1021/acsami.7b13096.
(55) Williamson, G. A.; Hu, V. W.; Yoo, T. B.; Affandy, M.; Opie, C.; Paradis, E. K.; Holmberg, V. C. Temperature-Dependent Electrochemical Characteristics of Antimony Nanocrystal Alloying Electrodes for Na-Ion Batteries. *ACS Appl. Energy Mater.* **2019**, *2* (9), 6741–6750. https://doi.org/10.1021/acsaem.9b01216.
(56) Shah, P. S.; Hanrath, T.; Johnston, K. P.; Korgel, B. A. Nanocrystal and Nanowire Synthesis and Dispersibility in Supercritical Fluids. *J. Phys. Chem. B* **2004**, *108* (28), 9574–9587. https://doi.org/10.1021/jp049827w.
(57) Holmes, J. D.; Ziegler, K. J.; Doty, R. C.; Pell, L. E.; Johnston, K. P.; Korgel, B. A. Highly Luminescent Silicon Nanocrystals with Discrete Optical Transitions. *J. Am. Chem. Soc.* **2001**, *123* (16), 3743–3748. https://doi.org/10.1021/ja002956f.
(58) Lu, X.; Ziegler, K. J.; Ghezelbash, A.; Johnston, K. P.; Korgel, B. A. Synthesis of Germanium Nanocrystals in High Temperature Supercritical Fluid Solvents. *Nano Lett.* **2004**, *4* (5), 969–974. https://doi.org/10.1021/nl049831j.
(59) Pell, L. E.; Schricker, A. D.; Mikulec, F. V.; Korgel, B. A. Synthesis of Amorphous Silicon Colloids by Trisilane Thermolysis in High Temperature Supercritical Solvents. *Langmuir* **2004**, *20* (16), 6546–6548. https://doi.org/10.1021/la048671o.
(60) Hanrath, T.; Korgel, B. A. Supercritical Fluid–Liquid–Solid (SFLS) Synthesis of Si and Ge Nanowires Seeded by Colloidal Metal Nanocrystals. *Adv. Mater.* **2003**, *15* (5), 437–440. https://doi.org/10.1002/adma.200390101.
(61) Lu, X.; Hanrath, T.; Johnston, K. P.; Korgel, B. A. Growth of Single Crystal Silicon Nanowires in Supercritical Solution from Tethered Gold Particles on a Silicon Substrate. *Nano Lett.* **2003**, *3* (1), 93–99. https://doi.org/10.1021/nl0202307.
(62) Holmes, J. D.; Lyons, D. M.; Ziegler, K. J. Supercritical Fluid Synthesis of Metal and Semiconductor Nanomaterials. *Chemistry – A European Journal* **2003**, *9* (10), 2144–2150. https://doi.org/10.1002/chem.200204521.
(63) Hou, H.; Jing, M.; Zhang, Y.; Chen, J.; Huang, Z.; Ji, X. Cypress Leaf-like Sb as Anode Material for High-Performance Sodium-Ion Batteries. *Journal of Materials Chemistry A* **2015**, *3* (34), 17549–17552. https://doi.org/10.1039/C5TA04703J.
(64) Zhang, M.; Wang, Z.; Xi, G.; Ma, D.; Zhang, R.; Qian, Y. Large-Scale Synthesis of Antimony Nanobelt Bundles. *Journal of Crystal Growth* **2004**, *268* (1–2), 215–221. https://doi.org/10.1016/j.jcrysgro.2004.05.016.
(65) Liu, P.; Zhong, K.; Liang, C.; Yang, Q.; Tong, Y.; Li, G.; Hope, G. A. Self-Assembly of Three-Dimensional Nanostructured Antimony. *Chem. Mater.* **2008**, *20* (24), 7532–7538. https://doi.org/10.1021/cm802225h.
(66) Schiferl, D.; Barrett, C. S. The Crystal Structure of Arsenic at 4.2, 78 and 299°K. *J Appl Cryst, J Appl Crystallogr* **1969**, *2* (1), 30–36. https://doi.org/10.1107/S0021889869006443.
(67) Holmberg, V. C.; Korgel, B. A. Corrosion Resistance of Thiol- and Alkene-Passivated Germanium Nanowires. *Chem. Mater.* **2010**, *22* (12), 3698–3703. https://doi.org/10.1021/cm1005696.

(68) Momma, K.; Izumi, F. VESTA 3 for Three-Dimensional Visualization of Crystal, Volumetric and Morphology Data. *J Appl Cryst, J Appl Crystallogr* **2011**, *44* (6), 1272–1276. https://doi.org/10.1107/S0021889811038970.
(69) Downs, R. T.; Hall-Wallace, M. The American Mineralogist Crystal Structure Database. *American Mineralogist* **2003**, *88* (1), 247–250.
(70) Webb, R. Stella: Polyhedron Navigator. *Symmetry: Culture and Science* **2000**, *11* (1–4), 231–268.
(71) Aktürk, O. Ü.; Özçelik, V. O.; Ciraci, S. Single-Layer Crystalline Phases of Antimony: Antimonenes. *Phys. Rev. B* **2015**, *91* (23), 235446. https://doi.org/10.1103/PhysRevB.91.235446.
(72) Swanson, H. E.; Fuyat, R. K.; Ugrinic, G. M. *Standard X-Ray Diffraction Powder Patterns*; Circular of the Bureau of Standards; National Bureau of Standards: Washington, D.C., 1954; Vol. 3.
(73) Buerger, M. J. *Elementary Crystallography: An Introduction to the Fundamental Geometrical Features of Crystals*; John Wiley & Sons: New York, NY, 1963.
(74) Tran, R.; Xu, Z.; Radhakrishnan, B.; Winston, D.; Sun, W.; Persson, K. A.; Ong, S. P. Surface Energies of Elemental Crystals. *Scientific Data* **2016**, *3*, 160080. https://doi.org/10.1038/sdata.2016.80.
(75) Anthony, J. W.; Bideaux, R. A.; Bladh, K. W.; Nichols, M. C. *Handbook of Mineralogy. Vol. 1: Elements, Sulfides, Sulfosalts*; Mineral Data Publishing: Tucson, AZ, 1990; Vol. 1.
(76) Buerger, M. J. The Genesis of Twin Crystals. *American mineralogist* **1945**, *30* (7–8), 469–482.
(77) Bennett, A. I. *Crystals Perfect and Imperfect*; Walker: New York, NY, 1965.
(78) Cejka, J.; Corma, A.; Zones, S. *Zeolites and Catalysis: Synthesis, Reactions and Applications*; Wiley-VCH: Mörlenbach, Germany, 2010.
(79) Svensson, C. Refinement of the Crystal Structure of Cubic Antimony Trioxide, Sb_2O_3. *Acta Cryst B* **1975**, *31* (8), 2016–2018. https://doi.org/10.1107/S0567740875006759.
(80) Weppner, W.; Huggins, R. A. Determination of the Kinetic Parameters of Mixed-Conducting Electrodes and Application to the System Li_3Sb. *J. Electrochem. Soc.* **1977**, *124* (10), 1569–1578. https://doi.org/10.1149/1.2133112.
(81) Li, L.; Jacobs, R.; Gao, P.; Gan, L.; Wang, F.; Morgan, D.; Jin, S. Origins of Large Voltage Hysteresis in High-Energy-Density Metal Fluoride Lithium-Ion Battery Conversion Electrodes. *J. Am. Chem. Soc.* **2016**, *138* (8), 2838–2848. https://doi.org/10.1021/jacs.6b00061.
(82) Baggetto, L.; Ganesh, P.; Sun, C.-N.; Meisner, R. A.; Zawodzinski, T. A.; Veith, G. M. Intrinsic Thermodynamic and Kinetic Properties of Sb Electrodes for Li-Ion and Na-Ion Batteries: Experiment and Theory. *J. Mater. Chem. A* **2013**, *1* (27), 7985–7994. https://doi.org/10.1039/c3ta11568b.
(83) Landesfeind, J.; Hattendorff, J.; Ehrl, A.; Wall, W. A.; Gasteiger, H. A. Tortuosity Determination of Battery Electrodes and Separators by Impedance Spectroscopy. *J. Electrochem. Soc.* **2016**, *163* (7), A1373–A1387. https://doi.org/10.1149/2.1141607jes.
(84) Liu, Z.; Mukherjee, P. P. Microstructure Evolution in Lithium-Ion Battery Electrode Processing. *J. Electrochem. Soc.* **2014**, *161* (8), E3248–E3258. https://doi.org/10.1149/2.026408jes.

(85) Wen, L.; Sun, J.; An, L.; Wang, X.; Ren, X. T.; Liang, G. Effect of Conductive Material Morphology on Spherical Lithium Iron Phosphate. *Nanomaterials* **2018**, *8* (11), 904. https://doi.org/10.3390/nano8110904.

(86) Kwon, Y. H.; Huie, M. M.; Choi, D.; Chang, M.; Marschilok, A. C.; Takeuchi, K. J.; Takeuchi, E. S.; Reichmanis, E. Toward Uniformly Dispersed Battery Electrode Composite Materials: Characteristics and Performance. *ACS Appl. Mater. Interfaces* **2016**, *8* (5), 3452–3463. https://doi.org/10.1021/acsami.5b11938.

(87) AL-Shroofy, M. N. Understanding and Improving Manufacturing Processes for Making Lithium-Ion Battery Electrodes, University of Kentucky Libraries, 2017. https://doi.org/10.13023/etd.2017.296.

(88) Yabuuchi, N.; Takeuchi, M.; Nakayama, M.; Shiiba, H.; Ogawa, M.; Nakayama, K.; Ohta, T.; Endo, D.; Ozaki, T.; Inamasu, T.; et al. High-Capacity Electrode Materials for Rechargeable Lithium Batteries: Li_3NbO_4-Based System with Cation-Disordered Rocksalt Structure. *PNAS* **2015**, *112* (25), 7650–7655. https://doi.org/10.1073/pnas.1504901112.

(89) Zhou, X.; Yin, Y.-X.; Wan, L.-J.; Guo, Y.-G. Self-Assembled Nanocomposite of Silicon Nanoparticles Encapsulated in Graphene through Electrostatic Attraction for Lithium-Ion Batteries. *Advanced Energy Materials* **2012**, *2* (9), 1086–1090. https://doi.org/10.1002/aenm.201200158.

(90) Li, D.; Zhou, H. Two-Phase Transition of Li-Intercalation Compounds in Li-Ion Batteries. *Materials Today* **2014**, *17* (9), 451–463. https://doi.org/10.1016/j.mattod.2014.06.002.

(91) Obrovac, M. N.; Christensen, L. Structural Changes in Silicon Anodes during Lithium Insertion/Extraction. *Electrochem. Solid-State Lett.* **2004**, *7* (5), A93–A96. https://doi.org/10.1149/1.1652421.

(92) Einfal, T.; Planinšek, O.; Hrovat, K. Methods of Amorphization and Investigation of the Amorphous State. *Acta Pharmaceutica* **2013**, *63* (3), 305–334. https://doi.org/10.2478/acph-2013-0026.

(93) Eising, G.; Pauza, A.; Kooi, B. J. Stress-Induced Crystallization of Ge-Doped Sb Phase-Change Thin Films. *Crystal Growth & Design* **2013**, *13* (1), 220–225. https://doi.org/10.1021/cg3013848.

(94) Toki, S.; Fujimaki, T.; Okuyama, M. Strain-Induced Crystallization of Natural Rubber as Detected Real-Time by Wide-Angle X-Ray Diffraction Technique. *Polymer* **2000**, *41* (14), 5423–5429. https://doi.org/10.1016/S0032-3861(99)00724-7.

(95) Ran, S.; Wang, Z.; Burger, C.; Chu, B.; Hsiao, B. S. Mesophase as the Precursor for Strain-Induced Crystallization in Amorphous Poly(Ethylene Terephthalate) Film. *Macromolecules* **2002**, *35* (27), 10102–10107. https://doi.org/10.1021/ma021252i.

(96) Shahrjerdi, D.; Hekmatshoar, B.; Rezaee, L.; Mohajerzadeh, S. S. Low Temperature Stress-Induced Crystallization of Germanium on Plastic. *Thin Solid Films* **2003**, *427* (1), 330–334. https://doi.org/10.1016/S0040-6090(02)01200-2.

(97) Manoharan, M. P.; Kumar, S.; Haque, M. A.; Rajagopalan, R.; Foley, H. C. Room Temperature Amorphous to Nanocrystalline Transformation in Ultra-Thin Films under Tensile Stress: An in Situ TEM Study. *Nanotechnology* **2010**, *21* (50), 505707. https://doi.org/10.1088/0957-4484/21/50/505707.

(98) Liu, X. H.; Zhong, L.; Huang, S.; Mao, S. X.; Zhu, T.; Huang, J. Y. Size-Dependent Fracture of Silicon Nanoparticles During Lithiation. *ACS Nano* **2012**, *6* (2), 1522–1531. https://doi.org/10.1021/nn204476h.

(99) Brauer, G.; Zintl, E. Konstitution von Phosphiden, Arseniden, Antimoniden Und Wismutiden Des Lithiums, Natriums Und Kaliums. *Zeitschrift für Physikalische Chemie* **1937**, *37B* (1), 323–352. https://doi.org/10.1515/zpch-1937-0125.
(100) Gerya Taras V. *Stress and Strain*; Cambridge University Press: New York, NY, 2010.
(101) Gaillac, R.; Pullumbi, P.; Coudert, F.-X. ELATE: An Open-Source Online Application for Analysis and Visualization of Elastic Tensors. *J. Phys.: Condens. Matter* **2016**, *28* (27), 275201. https://doi.org/10.1088/0953-8984/28/27/275201.
(102) Zhao, K.; Pharr, M.; Vlassak, J. J.; Suo, Z. Inelastic Hosts as Electrodes for High-Capacity Lithium-Ion Batteries. *Journal of Applied Physics* **2011**, *109* (1), 016110. https://doi.org/10.1063/1.3525990.
(103) Hutchinson, J. W.; Suo, Z. Mixed Mode Cracking in Layered Materials. *Advances in Applied Mechanics* **1991**, *29*, 63–191. https://doi.org/10.1016/S0065-2156(08)70164-9.
(104) Pugno, N.; Marino, F.; Carpinteri, A. Towards a Periodic Table for the Nanomechanical Properties of the Elements. *International Journal of Solids and Structures* **2006**, *43* (18–19), 5647–5657. https://doi.org/10.1016/j.ijsolstr.2005.12.003.
(105) Sethuraman, V. A.; Chon, M. J.; Shimshak, M.; Srinivasan, V.; Guduru, P. R. In Situ Measurements of Stress Evolution in Silicon Thin Films during Electrochemical Lithiation and Delithiation. *Journal of Power Sources* **2010**, *195* (15), 5062–5066. https://doi.org/10.1016/j.jpowsour.2010.02.013.
(106) Takamura, T.; Ohara, S.; Uehara, M.; Suzuki, J.; Sekine, K. A Vacuum Deposited Si Film Having a Li Extraction Capacity over 2000 MAh/g with a Long Cycle Life. *Journal of Power Sources* **2004**, *129* (1), 96–100. https://doi.org/10.1016/j.jpowsour.2003.11.014.
(107) Wang, X. J.; Yu, X. Q.; Li, H.; Yang, X. Q.; McBreen, J.; Huang, X. J. Li-Storage in $LiFe_{1/4}Mn_{1/4}Co_{1/4}Ni_{1/4}PO_4$ Solid Solution. *Electrochemistry Communications* **2008**, *10* (9), 1347–1350. https://doi.org/10.1016/j.elecom.2008.07.010.
(108) Bickelhaupt, F. M.; Houk, K. N. Analyzing Reaction Rates with the Distortion/Interaction-Activation Strain Model. *Angewandte Chemie International Edition* **2017**, *56* (34), 10070–10086. https://doi.org/10.1002/anie.201701486.
(109) Wang, Z.-W.; Shu, D.-J.; Wang, M.; Ming, N.-B. Strain Effect on Diffusion Properties of Oxygen Vacancies in Bulk and Subsurface of Rutile TiO_2. *Surface Science* **2012**, *606* (3), 186–191. https://doi.org/10.1016/j.susc.2011.09.014.
(110) Verma, M. K. S.; Basu, S.; Hariharan, K. S.; Kolake, S. M.; Song, T.; Jeon, J. A Strain-Diffusion Coupled Electrochemical Model for Lithium-Ion Battery. *J. Electrochem. Soc.* **2017**, *164* (13), A3426–A3439. https://doi.org/10.1149/2.0021714jes.
(111) Liang, H.; Zhang, X.; Yang, L.; Wu, Y.; Chen, H.; Song, W.; Fang, D. Electrochemomechanical Coupled Behaviors of Deformation and Failure in Electrode Materials for Lithium-Ion Batteries. *Sci. China Technol. Sci.* **2019**, *62* (8), 1277–1296. https://doi.org/10.1007/s11431-018-9485-6.
(112) Yang, W.; Xie, H.; Shi, B.; Song, H.; Qiu, W.; Zhang, Q. In-Situ Experimental Measurements of Lithium Concentration Distribution and Strain Field of Graphite Electrodes during Electrochemical Process. *Journal of Power Sources* **2019**, *423*, 174–182. https://doi.org/10.1016/j.jpowsour.2019.03.076.
(113) Dees, D. W.; Kawauchi, S.; Abraham, D. P.; Prakash, J. Analysis of the Galvanostatic Intermittent Titration Technique (GITT) as Applied to a Lithium-Ion Porous Electrode. *Journal of Power Sources* **2009**, *189* (1), 263–268. https://doi.org/10.1016/j.jpowsour.2008.09.045.

(114) Kashkooli, A. G.; Amirfazli, A.; Farhad, S.; Lee, D. U.; Felicelli, S.; Park, H. W.; Feng, K.; De Andrade, V.; Chen, Z. Representative Volume Element Model of Lithium-Ion Battery Electrodes Based on X-Ray Nano-Tomography. *J Appl Electrochem* **2017**, *47* (3), 281–293. https://doi.org/10.1007/s10800-016-1037-y.

(115) Pfaffmann, L.; Birkenmaier, C.; Müller, M.; Bauer, W.; Mitsch, T.; Feinauer, J.; Krämer, Y.; Scheiba, F.; Hintennach, A.; Schleid, T.; et al. Investigation of the Electrochemically Active Surface Area and Lithium Diffusion in Graphite Anodes by a Novel OsO_4 Staining Method. *Journal of Power Sources* **2016**, *307*, 762–771. https://doi.org/10.1016/j.jpowsour.2015.12.085.

(116) Verma, A.; Smith, K.; Santhanagopalan, S.; Abraham, D.; Yao, K. P.; Mukherjee, P. P. Galvanostatic Intermittent Titration and Performance Based Analysis of $LiNi_{0.5}Co_{0.2}Mn_{0.3}O_2$ Cathode. *J. Electrochem. Soc.* **2017**, *164* (13), A3380–A3392. https://doi.org/10.1149/2.1701713jes.

(117) Jain, A.; Ong, S. P.; Hautier, G.; Chen, W.; Richards, W. D.; Dacek, S.; Cholia, S.; Gunter, D.; Skinner, D.; Ceder, G.; et al. The Materials Project: A Materials Genome Approach to Accelerating Materials Innovation. *APL Materials* **2013**, *1* (1), 011002. https://doi.org/10.1063/1.4812323.

(118) Zhu, Y.; Wang, C. Galvanostatic Intermittent Titration Technique for Phase-Transformation Electrodes. *J. Phys. Chem. C* **2010**, *114* (6), 2830–2841. https://doi.org/10.1021/jp9113333.

(119) Oh, S.-T.; Sekino, T.; Niihara, K. Effect of Particle Size Distribution and Mixing Homogeneity on Microstructure and Strength of Alumina/Copper Composites. *Nanostructured Materials* **1998**, *10* (2), 327–332. https://doi.org/10.1016/S0965-9773(98)00072-5.

(120) Cromer, D. T. The Crystal Structure of NaSb. *Acta Cryst, Acta Crystallogr* **1959**, *12* (1), 41–45. https://doi.org/10.1107/S0365110X59000123.

(121) Swanson, H. E.; Tatge, E. *Standard X-Ray Diffraction Powder Patterns*; Circular of the Bureau of Standards; National Bureau of Standards: Washington, D.C., 1953; Vol. 1.

(122) Yang, Y. W.; Coppens, P. The Electron Density and Bonding in Beryllium Metal as Studied by Fourier Methods. *Acta Crystallographica Section A* **1978**, *34* (1), 61–65. https://doi.org/10.1107/S0567739478000121.

(123) Ida, T.; Ando, M.; Toraya, H. Extended Pseudo-Voigt Function for Approximating the Voigt Profile. *J Appl Cryst* **2000**, *33* (6), 1311–1316. https://doi.org/10.1107/S0021889800010219.

(124) Thompson, P.; Cox, D. E.; Hastings, J. B. Rietveld Refinement of Debye-Scherrer Synchrotron X-Ray Data from Al_2O_3. *J. Appl. Cryst.* **1987**, *20* (2), 79–83. https://doi.org/10.1107/S0021889887087090.

(125) Okamoto, H.; Schlesinger, M. E.; Mueller, E. M. *Alloy Phase Diagrams*; ASM Handbook; ASM International: Materials Park, OH, 2016; Vol. 3.

(126) Weather Underground, Seattle-Tacoma International Airport Weather History https://www.wunderground.com/history/daily/us/wa/seattle/KSEA/date/2019-4-3 (accessed Apr 3, 2019).

(127) Lin, H. -p; Chua, D.; Salomon, M.; Shiao, H.-C.; Hendrickson, M.; Plichta, E.; Slane, S. Low-Temperature Behavior of Li-Ion Cells. *Electrochem. Solid-State Lett.* **2001**, *4* (6), A71–A73. https://doi.org/10.1149/1.1368736.

(128) Sides, C. R.; Martin, C. R. Nanostructured Electrodes and the Low-Temperature Performance of Li-Ion Batteries. *Advanced Materials* **2005**, *17* (1), 125–128. https://doi.org/10.1002/adma.200400517.
(129) Plichta, E. J.; Hendrickson, M.; Thompson, R.; Au, G.; Behl, W. K.; Smart, M. C.; Ratnakumar, B. V.; Surampudi, S. Development of Low Temperature Li-Ion Electrolytes for NASA and DoD Applications. *Journal of Power Sources* **2001**, *94* (2), 160–162. https://doi.org/10.1016/S0378-7753(00)00578-4.
(130) Nagasubramanian, G. Electrical Characteristics of 18650 Li-Ion Cells at Low Temperatures. *Journal of Applied Electrochemistry* **2001**, *31* (1), 99–104. https://doi.org/10.1023/A:1004113825283.
(131) Huang, C.-K.; Sakamoto, J. S.; Wolfenstine, J.; Surampudi, S. The Limits of Low-Temperature Performance of Li-Ion Cells. *J. Electrochem. Soc.* **2000**, *147* (8), 2893–2896. https://doi.org/10.1149/1.1393622.
(132) Baggetto, L.; Oudenhoven, J. F. M.; van Dongen, T.; Klootwijk, J. H.; Mulder, M.; Niessen, R. A. H.; de Croon, M. H. J. M.; Notten, P. H. L. On the Electrochemistry of an Anode Stack for All-Solid-State 3D-Integrated Batteries. *Journal of Power Sources* **2009**, *189* (1), 402–410. https://doi.org/10.1016/j.jpowsour.2008.07.076.
(133) Zhang, S. S.; Xu, K.; Allen, J. L.; Jow, T. R. Effect of Propylene Carbonate on the Low Temperature Performance of Li-Ion Cells. *Journal of Power Sources* **2002**, *110* (1), 216–221. https://doi.org/10.1016/S0378-7753(02)00272-0.
(134) Liu, B.; Li, B.; Guan, S. Effect of Fluoroethylene Carbonate Additive on Low Temperature Performance of Li-Ion Batteries. *Electrochem. Solid-State Lett.* **2012**, *15* (6), A77–A79. https://doi.org/10.1149/2.027206esl.
(135) Markevich, E.; Salitra, G.; Aurbach, D. Low Temperature Performance of Amorphous Monolithic Silicon Anodes: Comparative Study of Silicon and Graphite Electrodes. *J. Electrochem. Soc.* **2016**, *163* (10), A2407–A2412. https://doi.org/10.1149/2.1291610jes.
(136) Peters, A. P. H. *Concise Chemical Thermodynamics*; CRC Press, 2010. https://doi.org/10.1201/9781439813331.
(137) Ancheyta Juárez, J. *Chemical Reaction Kinetics: Concepts, Methods, and Case Studies*; John Wiley & Sons, Inc: Hoboken, NJ, 2017.
(138) Orazem, M. E.; Tribollet, B. *Electrochemical Impedance Spectroscopy*; John Wiley & Sons, 2011.
(139) Hong, W.; Ge, P.; Jiang, Y.; Yang, L.; Tian, Y.; Zou, G.; Cao, X.; Hou, H.; Ji, X. Yolk–Shell-Structured Bismuth@N-Doped Carbon Anode for Lithium-Ion Battery with High Volumetric Capacity. *ACS Appl. Mater. Interfaces* **2019**, *11* (11), 10829–10840. https://doi.org/10.1021/acsami.8b20477.
(140) Raccichini, R.; Amores, M.; Hinds, G. Critical Review of the Use of Reference Electrodes in Li-Ion Batteries: A Diagnostic Perspective. *Batteries* **2019**, *5* (1), 12. https://doi.org/10.3390/batteries5010012.
(141) Waag, W.; Käbitz, S.; Sauer, D. U. Experimental Investigation of the Lithium-Ion Battery Impedance Characteristic at Various Conditions and Aging States and Its Influence on the Application. *Applied Energy* **2013**, *102*, 885–897. https://doi.org/10.1016/j.apenergy.2012.09.030.
(142) Howey, D. A.; Mitcheson, P. D.; Yufit, V.; Offer, G. J.; Brandon, N. P. Online Measurement of Battery Impedance Using Motor Controller Excitation. *IEEE*

Transactions on Vehicular Technology **2014**, *63* (6), 2557–2566. https://doi.org/10.1109/TVT.2013.2293597.

(143) Hess, M. Temperature-Dependence of the Solid-Electrolyte Interphase Overpotential: Part I. Two Parallel Mechanisms, One Phase Transition. *J. Electrochem. Soc.* **2018**, *165* (2), A323–A332. https://doi.org/10.1149/2.0701802jes.

(144) Johnson, D. ZView: A Software Program for IES Analysis, Version 3.5. *Scribner Associates, Inc., Southern Pines, NC* **2018**.

(145) Lvovich, V. F. *Impedance Spectroscopy: Applications to Electrochemical and Dielectric Phenomena*; John Wiley & Sons, Incorporated: Somerset, NJ, 2012.

(146) Jorcin, J.-B.; Orazem, M. E.; Pébère, N.; Tribollet, B. CPE Analysis by Local Electrochemical Impedance Spectroscopy. *Electrochimica Acta* **2006**, *51* (8–9), 1473–1479. https://doi.org/10.1016/j.electacta.2005.02.128.

(147) Vicente, N.; Haro, M.; Garcia-Belmonte, G. New Approaches to the Lithiation Kinetics in Reaction-Limited Battery Electrodes through Electrochemical Impedance Spectroscopy. *Chem. Commun.* **2018**, *54* (9), 1025–1040. https://doi.org/10.1039/C7CC08373D.

(148) Martinez-Julian, F.; Guerrero, A.; Haro, M.; Bisquert, J.; Bresser, D.; Paillard, E.; Passerini, S.; Garcia-Belmonte, G. Probing Lithiation Kinetics of Carbon-Coated $ZnFe_2O_4$ Nanoparticle Battery Anodes. *J. Phys. Chem. C* **2014**, *118* (12), 6069–6076. https://doi.org/10.1021/jp412641v.

(149) Xu, C.; Zeng, Y.; Rui, X.; Zhu, J.; Tan, H.; Guerrero, A.; Toribio, J.; Bisquert, J.; Garcia-Belmonte, G.; Yan, Q. Amorphous Iron Oxyhydroxide Nanosheets: Synthesis, Li Storage, and Conversion Reaction Kinetics. *J. Phys. Chem. C* **2013**, *117* (34), 17462–17469. https://doi.org/10.1021/jp405848j.

(150) Cooper, S. J.; Bertei, A.; Finegan, D. P.; Brandon, N. P. Simulated Impedance of Diffusion in Porous Media. *Electrochimica Acta* **2017**, *251*, 681–689. https://doi.org/10.1016/j.electacta.2017.07.152.

(151) Gönüllü, Y.; Kelm, K.; Mathur, S.; Saruhan, B. Equivalent Circuit Models for Determination of the Relation between the Sensing Behavior and Properties of Undoped/Cr Doped TiO_2 NTs. *Chemosensors* **2014**, *2* (1), 69–84. https://doi.org/10.3390/chemosensors2010069.

(152) Carrara, S.; Bavastrello, V.; Ricci, D.; Stura, E.; Nicolini, C. Improved Nanocomposite Materials for Biosensor Applications Investigated by Electrochemical Impedance Spectroscopy. *Sensors and Actuators B: Chemical* **2005**, *109* (2), 221–226. https://doi.org/10.1016/j.snb.2004.12.053.

(153) Diard, J.-P.; Le Gorrec, B.; Montella, C. Linear Diffusion Impedance. General Expression and Applications. *Journal of Electroanalytical Chemistry* **1999**, *471* (2), 126–131. https://doi.org/10.1016/S0022-0728(99)00262-4.

(154) Bisquert, J.; Garcia-Belmonte, G.; Bueno, P.; Longo, E.; Bulhões, L. O. S. Impedance of Constant Phase Element (CPE)-Blocked Diffusion in Film Electrodes. *Journal of Electroanalytical Chemistry* **1998**, *452* (2), 229–234. https://doi.org/10.1016/S0022-0728(98)00115-6.

(155) Wang, L.; Zhao, J.; He, X.; Gao, J.; Li, J.; Wan, C.; Jiang, C. Electrochemical Impedance Spectroscopy (EIS) Study of $LiNi_{1/3}Co_{1/3}Mn_{1/3}O_2$ for Li-Ion Batteries. *Int. J. Electrochem. Sci* **2012**, *7* (1), 345–353.

(156) Wendt, H.; Spinacé, E. V.; Oliveira Neto, A.; Linardi, M. Electrocatalysis and Electrocatalysts for Low Temperature Fuel Cells: Fundamentals, State of the Art, Research

and Development. *Química Nova* **2005**, *28* (6), 1066–1075. https://doi.org/10.1590/S0100-40422005000600023.

(157) Smith, K.; Wang, C.-Y. Solid-State Diffusion Limitations on Pulse Operation of a Lithium Ion Cell for Hybrid Electric Vehicles. *Journal of Power Sources* **2006**, *161* (1), 628–639. https://doi.org/10.1016/j.jpowsour.2006.03.050.

(158) Chang, Y.-C.; Jong, J.-H.; Fey, G. T.-K. Kinetic Characterization of the Electrochemical Intercalation of Lithium Ions into Graphite Electrodes. *J. Electrochem. Soc.* **2000**, *147* (6), 2033–2038. https://doi.org/10.1149/1.1393481.

(159) Jow, T. R.; Delp, S. A.; Allen, J. L.; Jones, J.-P.; Smart, M. C. Factors Limiting Li^+ Charge Transfer Kinetics in Li-Ion Batteries. *J. Electrochem. Soc.* **2018**, *165* (2), A361–A367. https://doi.org/10.1149/2.1221802jes.

(160) Pan, K.; Zou, F.; Canova, M.; Zhu, Y.; Kim, J.-H. Systematic Electrochemical Characterizations of Si and SiO Anodes for High-Capacity Li-Ion Batteries. *Journal of Power Sources* **2019**, *413*, 20–28. https://doi.org/10.1016/j.jpowsour.2018.12.010.

(161) Brauer, G.; Zintl, E. Konstitution von Phosphiden, Arseniden, Antimoniden und Wismutiden des Lithiums, Natriums und Kaliums. *Zeitschrift für Physikalische Chemie* **1937**, *37B* (1). https://doi.org/10.1515/zpch-1937-3725.

(162) Zhang, Y.; Xie, J.; Zhu, T.; Cao, G.; Zhao, X.; Zhang, S. Activation of Electrochemical Lithium and Sodium Storage of Nanocrystalline Antimony by Anchoring on Graphene via a Facile in Situ Solvothermal Route. *Journal of Power Sources* **2014**, *247*, 204–212. https://doi.org/10.1016/j.jpowsour.2013.08.096.

(163) Wang, J.; Yang, J.; Yin, W.; Hirano, S. Carbon-Coated Graphene/Antimony Composite with a Sandwich-like Structure for Enhanced Sodium Storage. *J. Mater. Chem. A* **2017**, *5* (39), 20623–20630. https://doi.org/10.1039/C7TA06770D.

(164) Levi, M. D.; Aurbach, D. Diffusion Coefficients of Lithium Ions during Intercalation into Graphite Derived from the Simultaneous Measurements and Modeling of Electrochemical Impedance and Potentiostatic Intermittent Titration Characteristics of Thin Graphite Electrodes. *J. Phys. Chem. B* **1997**, *101* (23), 4641–4647. https://doi.org/10.1021/jp9701911.

(165) Chung, M. D.; Seo, J. H.; Zhang, X. C.; Sastry, A. M. Implementing Realistic Geometry and Measured Diffusion Coefficients into Single Particle Electrode Modeling Based on Experiments with Single $LiMn_2O_4$ Spinel Particles. *J. Electrochem. Soc.* **2011**, *158* (4), A371. https://doi.org/10.1149/1.3549161.

(166) Shi, Q.; Hu, R.; Zeng, M.; Zhu, M. A Diffusion Kinetics Study of Li-Ion in LiV_3O_8 Thin Film Electrode. *Electrochimica Acta* **2010**, *55* (22), 6645–6650. https://doi.org/10.1016/j.electacta.2010.06.009.

(167) Yu, P. Determination of the Lithium Ion Diffusion Coefficient in Graphite. *J. Electrochem. Soc.* **1999**, *146* (1), 8. https://doi.org/10.1149/1.1391556.

(168) Xie, J.; Imanishi, N.; Matsumura, T.; Hirano, A.; Takeda, Y.; Yamamoto, O. Orientation Dependence of Li–Ion Diffusion Kinetics in $LiCoO_2$ Thin Films Prepared by RF Magnetron Sputtering. *Solid State Ionics* **2008**, *179* (9), 362–370. https://doi.org/10.1016/j.ssi.2008.02.051.

(169) Pan, J.; Wang, N.; Zhou, Y.; Yang, X.; Zhou, W.; Qian, Y.; Yang, J. Simple Synthesis of a Porous Sb/Sb_2O_3 Nanocomposite for a High-Capacity Anode Material in Na-Ion Batteries. *Nano Res.* **2017**, *10* (5), 1794–1803. https://doi.org/10.1007/s12274-017-1501-y.

(170) Liu, Z.; Yu, X.-Y.; Lou, X. W. D.; Paik, U. Sb@C Coaxial Nanotubes as a Superior Long-Life and High-Rate Anode for Sodium Ion Batteries. *Energy Environ. Sci.* **2016**, *9* (7), 2314–2318. https://doi.org/10.1039/C6EE01501H.
(171) Bryngelsson, H.; Eskhult, J.; Nyholm, L.; Herranen, M.; Alm, O.; Edström, K. Electrodeposited Sb and Sb/Sb_2O_3 Nanoparticle Coatings as Anode Materials for Li-Ion Batteries. *Chem. Mater.* **2007**, *19* (5), 1170–1180. https://doi.org/10.1021/cm0624769.
(172) Hong, K.-S.; Nam, D.-H.; Lim, S.-J.; Sohn, D.; Kim, T.-H.; Kwon, H. Electrochemically Synthesized Sb/Sb_2O_3 Composites as High-Capacity Anode Materials Utilizing a Reversible Conversion Reaction for Na-Ion Batteries. *ACS Appl. Mater. Interfaces* **2015**, *7* (31), 17264–17271. https://doi.org/10.1021/acsami.5b04225.
(173) Hu, M.; Jiang, Y.; Sun, W.; Wang, H.; Jin, C.; Yan, M. Reversible Conversion-Alloying of Sb_2O_3 as a High-Capacity, High-Rate, and Durable Anode for Sodium Ion Batteries. *ACS applied materials & interfaces* **2014**, *6* (21), 19449–19455. https://doi.org/10.1021/am505505m.
(174) Kim, S.; Qu, S.; Zhang, R.; Braun, P. V. High Volumetric and Gravimetric Capacity Electrodeposited Mesostructured Sb_2O_3 Sodium Ion Battery Anodes. *Small* **2019**, *15* (3), 1900258. https://doi.org/10.1002/smll.201900258.
(175) Yang, X.; Ma, J.; Wang, H.; Chai, Y.; Yuan, R. Partially Reduced Sb/Sb_2O_3@C Spheres with Enhanced Electrochemical Performance for Lithium Ion Storage. *Materials Chemistry and Physics* **2018**, *213*, 208–212. https://doi.org/10.1016/j.matchemphys.2018.04.027.
(176) Saadi, N. S.; Hassan, L. B.; Karabacak, T. Metal Oxide Nanostructures by a Simple Hot Water Treatment. *Scientific Reports* **2017**, *7* (1), 7158. https://doi.org/10.1038/s41598-017-07783-8.
(177) Centers, P. W. Sublimation-Controlled Oxidation of Antimony Trioxide. *Journal of Solid State Chemistry* **1988**, *72* (2), 303–308. https://doi.org/10.1016/0022-4596(88)90033-3.
(178) Cheetham, A. K. Structure Determination from Powder Diffraction Data: An Overview. In *Structure determination from powder diffraction data*; Oxford University Press: New York, NY, 2006; pp 13–28.
(179) Copper Foil for Battery Anode Substrate (190m length x 298mm width x 9um thickness) - EQ-bccf-9u https://www.mtixtl.com (accessed Aug 4, 2019).
(180) Copper Foil CU000272 - Goodfellow Catalog http://www.goodfellowusa.com (accessed Aug 4, 2019).
(181) Copper Foil (Width : 200 mm, Length : 145 m) – Cambridge Energy Solutions https://cam-energy.com (accessed Aug 4, 2019).
(182) Dickson, D.; Liu, G.; Li, C.; Tachiev, G.; Cai, Y. Dispersion and Stability of Bare Hematite Nanoparticles: Effect of Dispersion Tools, Nanoparticle Concentration, Humic Acid and Ionic Strength. *Science of The Total Environment* **2012**, *419*, 170–177. https://doi.org/10.1016/j.scitotenv.2012.01.012.
(183) Golunski, S. E.; Jackson, D. Antimony Oxides: A Guide to Phase Changes during Catalyst Preparation. *Applied Catalysis* **1989**, *48* (1), 123–135. https://doi.org/10.1016/S0166-9834(00)80270-5.
(184) Cody, C. A.; DiCarlo, L.; Darlington, R. K. Vibrational and Thermal Study of Antimony Oxides. *Inorg. Chem.* **1979**, *18* (6), 1572–1576. https://doi.org/10.1021/ic50196a036.
(185) Thermal Stability and Phase Transitions of the Oxides of Antimony. *Thermochimica Acta* **1981**, *51* (2–3), 153–168. https://doi.org/10.1016/0040-6031(81)85155-6.

(186) Zhang, W.-J. Lithium Insertion/Extraction Mechanism in Alloy Anodes for Lithium-Ion Batteries. *Journal of Power Sources* **2011**, *196* (3), 877–885. https://doi.org/10.1016/j.jpowsour.2010.08.114.
(187) Berla, L. A.; Lee, S. W.; Ryu, I.; Cui, Y.; Nix, W. D. Robustness of Amorphous Silicon during the Initial Lithiation/Delithiation Cycle. *Journal of Power Sources* **2014**, *258*, 253–259. https://doi.org/10.1016/j.jpowsour.2014.02.032.
(188) Zhao, K.; Wang, W. L.; Gregoire, J.; Pharr, M.; Suo, Z.; Vlassak, J. J.; Kaxiras, E. Lithium-Assisted Plastic Deformation of Silicon Electrodes in Lithium-Ion Batteries: A First-Principles Theoretical Study. *Nano Lett.* **2011**, *11* (7), 2962–2967. https://doi.org/10.1021/nl201501s.
(189) Pharr, M.; Suo, Z.; Vlassak, J. J. Measurements of the Fracture Energy of Lithiated Silicon Electrodes of Li-Ion Batteries. *Nano Lett.* **2013**, *13* (11), 5570–5577. https://doi.org/10.1021/nl403197m.
(190) Zhao, K.; Pharr, M.; Vlassak, J. J.; Suo, Z. Fracture of Electrodes in Lithium-Ion Batteries Caused by Fast Charging. *Journal of Applied Physics* **2010**, *108* (7), 073517. https://doi.org/10.1063/1.3492617.
(191) Markevich, E.; Levi, M. D.; Aurbach, D. Comparison between Potentiostatic and Galvanostatic Intermittent Titration Techniques for Determination of Chemical Diffusion Coefficients in Ion-Insertion Electrodes. *Journal of Electroanalytical Chemistry* **2005**, *580* (2), 231–237. https://doi.org/10.1016/j.jelechem.2005.03.030.
(192) Weppner, W.; Huggins, R. A. Electrochemical Methods for Determining Kinetic Properties of Solids. *Annu. Rev. Mater. Sci.* **1978**, *8* (1), 269–311. https://doi.org/10.1146/annurev.ms.08.080178.001413.
(193) He, K.; Lin, F.; Zhu, Y.; Yu, X.; Li, J.; Lin, R.; Nordlund, D.; Weng, T.-C.; Richards, R. M.; Yang, X.-Q.; et al. Sodiation Kinetics of Metal Oxide Conversion Electrodes: A Comparative Study with Lithiation. *Nano Lett.* **2015**, *15* (9), 5755–5763. https://doi.org/10.1021/acs.nanolett.5b01709.
(194) Gu, M.; Genc, A.; Belharouak, I.; Wang, D.; Amine, K.; Thevuthasan, S.; Baer, D. R.; Zhang, J.-G.; Browning, N. D.; Liu, J.; et al. Nanoscale Phase Separation, Cation Ordering, and Surface Chemistry in Pristine $Li_{1.2}Ni_{0.2}Mn_{0.6}O_2$ for Li-Ion Batteries. *Chem. Mater.* **2013**, *25* (11), 2319–2326. https://doi.org/10.1021/cm4009392.
(195) Ebner, M.; Marone, F.; Stampanoni, M.; Wood, V. Visualization and Quantification of Electrochemical and Mechanical Degradation in Li Ion Batteries. *Science* **2013**, *342* (6159), 716–720. https://doi.org/10.1126/science.1241882.

Vita

Grant Andrew Williamson was born in Seattle, Washington. He graduated from Lakeside High School in 2008, and went on to attend the University of Washington, where he graduated *magna cum laude* with departmental honors with a Bachelor of Science in Chemical Engineering in 2012. Upon graduation, he went to work for GE Water and Process Technologies as an Instrumentation and Controls Engineer before returning to the University of Washington in 2015 for his graduate studies in Molecular Engineering, where he received a National Science Foundation Graduate Research Fellowship in 2016 and the University of Washington Husky 100 in 2017. Grant earned a Master of Science in Molecular Engineering in 2017 and earned his Ph.D. in Molecular Engineering while study nanomaterials and energy storage under the supervision of Dr. Vincent Holmberg.

This dissertation was typed by the author.